Modeling and Analysis of the Forced–Flow Thermal Gradient
Chemical Vapor Infiltration Process
for Fabrication of the Ceramic Matrix Composites

by

Ching Yi Tsai

Dissertation submitted to the Faculty of the
Virginia Polytechnic Institute and State University
in partial fulfillment of the requirements for the degree of
Doctor of Philosophy
in
Engineering Mechanics

APPROVED:

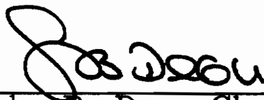
Seshu B. Desu, Chairman

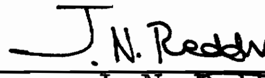
J. N. Reddy, Chairman

D. T. Mook

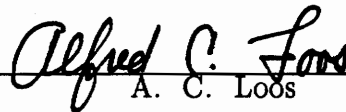
A. C. Loos

W. T. Reynolds, Jr.

June, 1993
Blacksburg, Virginia

c.2

LD
5655
V856
1993
T724
c.2

**Modeling and Analysis of the Forced–Flow Thermal Gradient**

**Chemical Vapor Infiltration Process**

**for Fabrication of the Ceramic Matrix Composites**

by

Ching Yi Tsai

Committee Chairmen: Seshu B. Desu and J. N. Reddy

Engineering Mechanics

(ABSTRACT)

The forced–flow thermal gradient chemical vapor infiltration (FCVI) process for fabricating ceramic matrix composites (CMCs) was modeled and analyzed based on the finite element method (FEM).

The modeling study was focused on the fabrication of silicon carbide (SiC) matrix composites from methyltrichlorosilane (MTS) precursors because of their high strength, high modulus and excellent oxidation resistance properties at high temperatures.

Unlike other available FCVI models, which use lumped reaction schemes, both gas phase and surface reactions of the FCVI process were explicitly considered for the present FEM FCVI model.

The kinetics of SiC deposition from MTS precursor were derived by analyzing our own deposition rate data as well as reported results. The SiC deposition process was modeled using the following reactions — (1) : gas phase decomposition of MTS molecules into two major intermediates, one containing silicon and the other

containing carbon; (2) : adsorption of the intermediates onto the surface sites of the growing film; (3) : reaction of the adsorbed intermediates to form silicon carbide.

The equilibrium constant for the gas phase decomposition process was divided into the forward and backward reaction constants as 2.0E+25 exp[(–448.2 kJ/mol)/RT] and 1.1E+32 exp[(–416.2 kJ/mol)/RT], respectively. Equilibrium constants for the surface adsorption reactions of silicon–carrying and carbon–carrying intermediates were determined to be 0.5E+11 exp[(–21.6 kJ/mol)/RT] and 7.1E+09 exp[(–33.1 kJ/mol)/RT], while the rate constant for the surface reaction of the intermediates was 4.6E+05 exp[(–265.1 kJ/mol)/RT].

Effects of the deposition temperature and vapor pressure variations on the density profiles of the composite preform were studied based on this FEM FCVI model. It was found that the advantages of the commonly used ambient–pressure FCVI process (APFCVI) are likely to be limited by the equipment and the accumulation of gaseous components around the entrance sides, which could render the deposition process to be mass transport limited. A conceptual multi–step FCVI process was proposed to alleviate this problem and obtain products of good final density profiles within reasonable processing times.

This multi–step FCVI process involved deposition under ambient–pressure to improve the density profiles and shorten the processing times. This was followed by the sub ambient–pressure FCVI process (LPFCVI) process to overcome the mass transfer limitations caused by the entrance accumulation effect and possible limitations on the equipment.

A balance between processing time and final density profile can be achieved through the use of this multi–step FCVI process. Advantages of this process has been demonstrated by studying the densification process in large size specimens.

# Acknowledgements

I would like to thank my two major advisors, Professor Seshu B. Desu and Professor J.N. Reddy, for their advice and support throughout the course of this work. Special thanks go to Professor Seshu B. Desu. Without his timely helping hand, this work would have been stopped three years ago. I am grateful indebted to Professor Desu for providing me so much freedom to learn and work independently and, at the same time, giving me so many invaluable suggestions when needed. Thanks also go to Professor J.N. Reddy, whom I had known earlier through books and papers only, for providing me with an insight into the finite element method.

Many thanks also to my advisory committee members: Professor D.T. Mook, Professor A.C. Loos, and Professor William T. Reynolds Jr., for their guidance and assistance in the completion of this manuscript.

I am indebted to the Center for Composite Materials and Structures of Virginia Polytechnic Institute and State University for providing me the Research Assistantship throughout my graduate study.

I would also like to thank all my colleagues and friends in Virginia Polytechnic Institute and State University. It has been my pleasure and good fortune to have shared time with them throughout my graduate study. Special thanks go to: Chien C. Chiu for his help in doing the silicon carbide depositions and being excellent roommate for almost three years; Dilip Vijay, Justin Gaynor and Warren Hendricks

for their unbelievable patience in helping me prepare my publications. Thanks to Dr. T.W. Sun, Dr. C.H. Peng, Gene Li, J.K. Chen, Ashraf Khan, Claire Chen, Jimmy Xing, Professor Z.J. Chen, Professor C. Qiu, Dr. Yoo, May Nyman, Jhing–Fang Chang, Wei Pan, Jie Si, Gang Chen, Kazuya Ishihara, and many others I might have forgotten for many interesting discussions and being good friends.

Finally, I wish to express my deepest love and appreciation to my family. Without their support and sacrifice I could not have finished this work.

This work is dedicated to my parents.

# Table of Contents

Chapter 1 Introduction ........ 1

1.1 Motivation ........ 1

1.2 Literature Review ........ 3

1.2.1 The Structural Element Sub–Model ........ 3

1.2.2 The Chemical Reaction Sub–Model ........ 5

1.2.3 The Transport Sub–Model ........ 6

1.3 The Present Study ........ 7

1.4 Presentation of Results ........ 9

Chapter 2 Evaluations of the Film Conformalities by Using the Step Coverage Method ........ 11

2.1 Abstract ........ 11

2.2 Introduction ........ 12

2.3 The 2–D Step Coverage Model and Its Comparisons with the 1–D Step Coverage Model ........ 14

2.3.1 Theory ........ 15

2.3.2 Results and Discussion ........ 19

2.4 The 2–D Step Coverage Model with Consideration of the Moving Deposition Fronts ........ 29

2.4.1 Theory ..... 29
2.4.1a Boundary Element Formulation of the Step Coverage Process ..... 29
2.4.1b Scheme for Updating the Substrate Surfaces during the Deposition Process ..... 33
2.4.2 Results and Discussion ..... 33
2.5 Summary ..... 49

Chapter 3 The Role of Gas–Phase Reactions in Modeling of the Forced–Flow Chemical Vapor Infiltration Process ..... 52
3.1 Abstract ..... 52
3.2 Introduction ..... 53
3.3 Mathematical Modeling of the Forced–Flow CVI Process ..... 55
3.4 Results and Discussion ..... 60
3.5 Summary ..... 70

Chapter 4 Kinetic Study of Silicon Carbide Deposited from Methyltrichlorosilane Precursor ..... 73
4.1 Abstract ..... 73
4.2 Introduction ..... 74
4.3 Experimental Procedure ..... 76
4.4 Modeling Calculations ..... 79
4.4.1 Deposition Mechanism ..... 79

4.4.2 Modeling of the Hot–Wall CVD Process .................................... 81
4.5 Results and Discussion .................................................................... 86
4.5.1 Deposition Rates of SiC at T=1273°K to 1423°K;
P=1.8, 5.0, 8.0 Torr; and $H_2$/MTS=50 ................................ 86
4.5.2 Determination of the Kinetic Data ............................................ 93
4.6 Summary ........................................................................................ 101

Chapter 5 A Finite Element Model for the Study of the Forced–Flow
Thermal–Gradient Chemical Vapor Infiltration Process .............. 103
5.1 Abstract ........................................................................................ 103
5.2 Introduction .................................................................................. 104
5.3 Mathematical Formulations of the FCVI Process ............................ 105
5.4 The Finite Element Modeling ......................................................... 110
5.5 Numerical Results and Discussion .................................................. 112
5.5.1 Influence of the Forced–Flow on the Thermal Profiles .............. 113
5.5.2 Ambient–Pressure Forced–Flow Thermal–Gradient
Chemical Vapor Infiltration Process .................................. 115
5.5.3 The Thickness Effect on the Densification ............................... 117
5.5.4 Optimization of the FCVI Process with Combinations
of Both APFCVI and LPFCVI Processes ..................................... 128
5.6 Summary ........................................................................................ 130

Chapter 6 Summary and Conclusions ................................................... 138

Appendix A Estimations of the Structural and Transport Properties ............... 142

Appendix B Solving the Conduction–Convection Equation ............................. 149

References ........................................................................................ 155

Vita ................................................................................................. 164

# List of Figures

**Chapter 2**


Figure 2.1 Illustrations of the Domain and Associated Boundaries Considered in the Step Coverage Modeling

Figure 2.2 Dimensionless Transverse Concentration Profiles at $y/L_b = 0.0, 0.4$ and 0.9
(a) $D_{am} = 0.1$ and Trench Width/Depth Ratio = 1.0
(b) $D_{am} = 5.0$ and Trench Width/Depth Ratio = 1.0

Figure 2.3 Trench Deposition Thickness Profiles
(a) $D_{am} = 0.1$ and Trench Width/Depth Ratio = 1.0
(b) $D_{am} = 5.0$ and Trench Width/Depth Ratio = 1.0

Figure 2.4 Values of the Numerical Error ($\epsilon_1$, $\epsilon_2$) of the 1–D Continuum–Like Step Coverage Model Resulting from the Lumped Geometry

Figure 2.5 Axial Concentration Profiles along the Trench Side–Wall with $D_{am} = 20.0$ and Trench Width/Depth Ratio = 1.0

Figure 2.6 Illustrations of the String Advancing Algorithm Used to Update the Deposition Fronts

Figure 2.7 Comparisons of the Modeling Predictions and Experimental Results of $SiO_2$ Step Coverage using $SiH_4/O_2$ Precursors

Figure 2.8 Trench Deposition Thickness Profiles
(a) Width=0.5$\mu$m, Depth=2.5$\mu$m, Temperature=540°K
(b) Width=0.5$\mu$m, Depth=2.5$\mu$m, Temperature=640°K
(c) Width=1.25$\mu$m, Depth=2.5$\mu$m, Temperature=540°K
(d) Width=1.25$\mu$m, Depth=2.5$\mu$m, Temperature=640°K

Figure 2.9 Axial Concentration Profiles along the Trench Side–Wall
(a) Width=0.5$\mu$m, Depth=2.5$\mu$m, Temperature=540°K
(b) Width=0.5$\mu$m, Depth=2.5$\mu$m, Temperature=640°K
(c) Width=1.25$\mu$m, Depth=2.5$\mu$m, Temperature=540°K
(d) Width=1.25$\mu$m, Depth=2.5$\mu$m, Temperature=640°K


**Chapter 3**


Figure 3.1 Deposition Rate Profiles of Surface Reaction Controlled FCVI Processes with $\Delta P$ being Equal to 0.1, 0.5, 1.0 and 1.5

Figure 3.2 Efficiency of the Forced–Flow Technique on Improving the Deposition Rate Profiles of Surface Reaction Controlled FCVI Processes. (The Peclet number was changed from 1.0 in Figure 3.1 to 0.2 to simulate changes of the medium permeability)

Figure 3.3 Deposition Rate Profiles of Gas–Phase Reaction Controlled FCVI Processes with $\Delta P$ being equal to 0.01, 0.1, 0.2, 0.3 and 0.5

Figure 3.4 Changes of Deposition Rate Profiles of Figure 3.1 with the Surface Damkohler Number being Changed from 0.02 to 0.0004, 0.002 and 0.004

Figure 3.5 Changes of Deposition Rate Profiles of Figure 3.3 with the Gas–Phase Damkohler Number being Changed from 0.1 to 0.01, 0.02 and 0.05

**Chapter 4**

Figure 4.1 A Schematic Diagram of the Hot–Wall CVD Reactor

Figure 4.2 Thermal Profiles of the Hot–Wall CVD Reactor

Figure 4.3 The Flow Velocity Profile with Total Gas Pressure = 1.8Torr; Deposition Temperature = 1373°K and $H_2$/MTS = 50

Figure 4.4 SEM Micrographs of the SiC Thin Films on Si(100) Substrates Growth at T=1050°C, $H_2$/MTS=100 for (a): 1.8 Torr, (b): 5.0 Torr, (c):8.0 Torr

Figure 4.5 SiC Deposition Rates as a Function of Deposition Temperatures

Figure 4.6 SiC Deposition Rates as a Function of the Total Gas Pressure

Figure 4.7 Pressure Profiles of $MTS_{(g)}$ and $IP_{si(g)}$ components with P=1.8, 5.0 Torr, T=1373°K, and $H_2$/MTS=50

Figure 4.8 Comparisons between Modeling Predictions and Reported Data from Neuschutz's SiC CVD Experiments

Figure 4.9 Comparisons between Modeling Predictions and Experimental Results : P=1.8, 5.0 and 8.0 Torr, T={1273, 1323, 1373, 1423}°K, and $H_2$/MTS=50

Figure 4.10 Comparisons between Modeling Predictions and Experimental Results : P=1.8Torr, T={1273, 1323, 1373, 1423}°K, and $H_2$/MTS = 10, 100

**Chapter 5**


Figure 5.1 A Schematic Diagram of the Forced–Flow Thermal–Gradient Chemical Vapor Infiltration Process

Figure 5.2 Influences of the Forced–Flow Effect on the Thermal Profiles

Figure 5.3 Deposition rate profiles of a Circular Disk with Radius and Thickness being Equal to 1.26cm and 0.6cm. Experimental Conditions are: $T_{fu}$=1273° K, ΔT=50° K, $H_2$ (outlet)= 1 atm
(a) $H_2$ (Inlet)=1.2 atm
(b) $H_2$ (Inlet)=1.8 atm

Figure 5.4 Improvements of the Resultant Density Profiles with the Use of the Forced–Flow Technique. Radius and Thickness of the Disk are Equal to 1.26cm and 0.6cm

Figure 5.5 Changes of the Resultant Density Resulting from an Increase in the Disk Thickness

Figure 5.6 Calculated Gas flow Profiles for Various ΔP Values: ΔPs are 0.2, 0.5 and 0.8 atm
(a) $T_{fu}$=1273° K, ΔT=50° K
(b) $T_{fu}$=1323° K, ΔT=50° K

Figure 5.7 Comparisons of Deposition Rate Profiles between APFCVI and LPFCVI Processes — $T_{fu}$=1373° K, ΔT=100° K, t=0.6cm

Figure 5.8 Comparisons of Deposition Rate Profiles between APFCVI and LPFCVI Processes — $T_{fu}$=1273° K, ΔT=50° K, t=1.2cm

Figure 5.9a Final Density Profiles of the Disk with Radius and Thickness being Equal to 1.26cm and 1.2cm. The Processing Conditions are Listed in Table 5.1

Figure 5.9b The Time Evolution of the Total Density of the Disk with Radius and Thickness being Equal to 1.26cm and 1.2cm. The Processing Conditions are Listed in Table 5.1

Figure 5.10a Deposition Rate Profiles for the Disk with Radius and Thickness being Equal to 1.26cm and 2.4cm

Figure 5.10b Final Density Profiles of the Disk with Radius and Thickness being Equal to 1.26 cm and 2.4 cm. The Processing Conditions are Listed in Table 5.2

Figure 5.10c The Time Evolution of the Total Density of the Disk with Radius and Thickness being Equal to 1.26cm and 2.4cm. The Processing Conditions are Listed in Table 5.2

# List of Tables


**Chapter 2**

Table 2.1 The Temperature Dependence of Deposition Rates and Sticking Coefficients of $SiO_2$ Thin Films Deposited from $SiH_4/O_2$ Precursors

**Chapter 4**

Table 4.1 Bulk Diffusion Constants of Five Gaseous Components Used in the SiC CVD Modeling Calculations

Table 4.2 Temperature Dependence of the Kinetic Data ($k_t K_{a1} K_{a2} \sqrt{K_g}$, $K_{a1} \sqrt{K_g}$, $K_{a2}$) of SiC Deposited from $MTS/H_2$ Precursors. These kinetic data were used to fit the SiC deposition rates reported by Neuschutz et al. [59], as shown in the Figure 4.8

Table 4.3 Temperature Dependence of the Kinetic Data ($K_{a1}$, $k_1$, $k_{-1}$) of SiC Deposited from $MTS/H_2$ Precursors. These kinetic data together with $K_{a2}$ and $K_t$ obtained in Table 4.2 were used in the CVD FEM model to calculate the SiC deposition rates , as shown in the Figures 4.9 and 4.10

**Chapter 5**

Table 5.1 Parameters of the FCVI Processes Used in Figures 5.9a and 5.9b

Table 5.2 Parameters of the FCVI Processes Used in Figures (5.10a–5.10c)

**Appendix A**

Table A.1 Parameters Used to Estimate the Bulk and Knudsen Diffusion Constants within Structures of Randomly Overlapping Fibers [20–22]

Table A.2 Constants $c_1$, $c_2$ and $V_{fmax}$ Used to Calculate the Permeability of a Uni–Directional Fiber Bundle [77]

**Appendix B**

Table B.1 Numerical Results of the Conduction–Convection Equation ( $-\frac{d^2T}{dx^2}$ + (Peclet Number) $\frac{dT}{dx} = 0$ ) Using Galerkin FEM, Upwinding FEM, and Canonical FEM Techniques
(a) Peclet Number = 0.25
(b) Peclet Number = 50
(c) Peclet Number = 25

# Chapter 1 Introduction

## 1.1 Motivation

Many engineers have come to realize that ceramics could be the ultimate solution to the problem of materials for harsh environments. Ceramic materials can offer benefits over conventional superalloys for many industry and military applications because of their higher temperature capability, lower density and better environmental resistance compared to most conventional metals.

In many applications that do not involve high impact loads, the monolithic ceramics are already being used. However, concerns on the toughness of monolithic ceramic materials have prevented their extensive use in many of the applications where their material properties could offer the maximum benefit.

The primary goal of many ceramic materials researchers has been to alter the properties of ceramic materials through composition, design, and processing techniques in order to minimize the adverse effects of the brittle nature and to retain other desirable properties. The reinforcement of the monolithic ceramic matrix by high performance fibers, the so called ceramic matrix composites (CMCs), is by far the most effective approach to achieve this goal.

Through the composite approach, the mechanical properties of the monolithic ceramics can be enhanced. The undesirable catastrophic failure associated with the monolithic ceramics can be prevented by providing the energy–dissipation paths,

such as crack deflection, fiber pull–out, and crack impediment [1–2], through the addition of toughening fibers.

In general, CMCs are more difficult to fabricate than other types of composites simply because the temperatures and pressures required to fabricate a ceramic component are much higher than those needed for other materials. Among the processing techniques available for fabrication of the CMCs, such as hot–pressing, sol–gel, Lanxide process, etc., chemical vapor infiltration techniques (CVI) have emerged as a strong candidate because of their ability to create all major families of ceramic matrices, to produce well–defined shapes with little dimensional change, to process at low temperature, and to reduce the interactions between the fiber and the matrix [3–5]. The development of forced–flow thermal–gradient CVI (FCVI) processes makes the CVI processes even more competitive because they ensure better uniformity of the deposited matrix and can reduce the processing time significantly [6] under certain conditions.

The purpose of this study is to develop a systematic approach to the study of FCVI processes for fabrication of the CMCs. Relationships between the experimental conditions, including temperature profiles and vapor pressures, and the quality of the FCVI process, as determined by the processing time and resultant composite density profiles, are the key interests behind this modeling effort.

This processing model will be highly valuable in optimizing the FCVI process to produce high quality components and eliminate the need for expensive trial experiments.

## 1.2 Literature Review

The chemical vapor infiltration process is a technique for densifying the ceramic matrix within the porous medium. Therefore, a self–consistent CVI modeling should include at least three sub–models, that is, the structural element, chemical reactions, and transport sub–models. These sub–models have to be integrated together to calculate the density distribution within the composite preforms during the densification processing.

Literature review of the CVI modeling are given based on their contribution on the development of the above three sub–models.

### 1.2.1 The Structural Element Sub–Model

The CVI process is a simultaneous transport and chemical reaction process that occurs within the composite preforms. The structural element model, which describes the geometry of the fibrous preform, is crucial to the CVI process modeling because the subsequent modeling of the transport and chemical reaction process is based on this.

With the complexity and randomness associated with the geometry of the fibrous preform, it is extremely difficult to have a precise and full scale description of the fibrous preform. Several simplified structural element models have been proposed to describe the structure of the composite preform thus leading to a tractable analysis of the infiltration process.

The single pore model, which assumes that the void space between fibers is circular in shape, is often used to describe the geometry of a uni–directional fiber

bundle [7–10]. Starting from the single pore model, several modified models have been proposed to describe the geometry of the fibrous preform. Two typical examples are the overlap pore model [11], which considers the deposited fiber surface to be overlapped, and the so–called gap–hole–space model [12], that considers the layered, woven type preform as a combination of holes, spaces, and gaps. As a matter of fact, the holes, spaces, and gaps are pores of different sizes.

The single pore model is not suitable for the description of the woven type composite preform unless the void space within the composite preform is divided into many sections of different sizes, which is the idea behind the gap–hole–space model. However, this kind of approach to describe the woven type or braided type composite preform could become very tedious once the composite preform is made up of many tows.

Starr [13] proposed a unit–cell approach to describe the geometry of the fibrous preform. In this modeling approach, the geometry of the composite preform is represented by the repetition of a unit cell, which depends on the packing geometry of the fibrous preform. The unit–cell models are commonly used to describe 2–D woven or 3–D braided type fibrous preforms [14]. Actually, the single pore model can be considered as a special case of the unit–cell model with the unit cell being the single pore.

Recently the effective medium approach has been used to describe the geometry of the composite preforms [15–18]. In the effective medium modeling approach, the composite preform is assumed to be a complex network with unit–cells of different sizes. The percolation theory , which is often used to study the combustion problem of porous chars [19], is then applied to study the evolution of the composite preform during the CVI process.

The concept behind the effective medium approach is more realistic in estimating the structural and transport properties of the fibrous medium compared to other modeling approaches. Recently, the gas diffusivity and structural properties of medium with randomly overlapping fibers were studied by Tomadakis and Sotirchos [20–22] based on this approach. The packing of fibers was considered to be one-directional (uni-directional fiber bundle), two-directional (woven type preform), or no preferred orientation (braided type preform). The gas diffusivity coefficient and structural properties of fibrous medium were fitted into functional forms. As a result, updating of the transport and structural properties during the CVI process could be easily implemented in a modeling computer program.

Although they might over-simplify the complex fibrous structures, these simplified geometry models can at least provide a qualitative picture of the fibrous medium.

### 1.2.2 The Chemical Reaction Sub-Model

Chemical reactions involved in the CVI processes are quite complex and can be broadly classified as gas phase and surface reactions. Most of the proposed CVI models lumped the chemical reactions into one single overall reaction for simplicity [8–9,11–13,15]. Recently, Middleman [7] and Sheldon [23] studied the control of the gas phase reactions to optimize the densification process. Both Middleman and Sheldon have shown that theoretically the gas phase kinetics can be controlled to alleviate the premature pore blockage problem.

As for the FCVI process modeling studies, the importance of including the gas phase reactions in the modeling calculations has not yet been documented.

However, the effectiveness of the forced–flow technique on improving the densification process might be strongly dependent on the rate controlling step of the FCVI process, as suggested by the study of determination of rate controlling step of the chemical vapor deposition (CVD) processes (which is a FCVI process in a reactor configuration) by Desu et. al [24].

This important issue will be investigated in this work.

### 1.2.3 The Transport Sub–model

For the FCVI processes, the gaseous species are supplied via the diffusion and convection (forced–flow) mechanisms. The diffusion mechanism of the gaseous species can be further separated into Knudsen and bulk (ordinary) diffusion mechanisms [25–27]. The Knudsen diffusion is controlled by the medium geometry, such as pore size, while the bulk diffusion is controlled by the mean free path of the diffusing molecules.

Although the Knudsen flow is negligible under the ambient pressure condition, which is the commonly–used condition for the FCVI processes [28], initially, this might not be the case at the later stage of the deposition process as the porosity of the medium decreases due to the matrix deposition. The reciprocal relationship or the so–called Bosanquet formula is often used to estimate the overall diffusion constant [25] based on both the Knudsen and bulk diffusion constants.

For the computation of the convection flow (forced–flow), Darcy's law, which predicts a linear relationship between the local pressure gradient and the local flow velocity, is often used [10,14,16].

As mentioned in the structural element sub–model, the network structure

nature of the medium has to be considered to estimate the effective transport coefficient within the porous medium.

## 1.3 The Present Study

The main purpose of the FCVI modeling is to understand the conformability of the deposited thin films or matrices within fibrous medium under various experimental conditions. Because of the complex structure associated with the fibrous preform, the deposition profiles of the FCVI process are not easy to obtain in general. Therefore, it is very difficult to compare the modeling calculations with the experimental results.

In chapter 2, a step coverage approach is proposed to verify the modeling calculations through deposition experiments in the sub–micro trench environment. Dimensional sizes of the trench, which is a via cut into the surface of a wafer, are similar to those of the void space within the fibrous preform. Most important of all, the step coverage profiles are much easier to obtain compared to the deposition thickness profiles of the FCVI processes within fibrous medium. Therefore, the correlation between the modeling calculations and experimental results can be established easily.

In the past, two different approaches have been proposed to model the CVD step coverage processes —— (1): the modified line–of–sight models solved by the Monte Carlo simulation technique [29–34]; (2): the one–dimensional (1–D) continuum–like diffusion–reaction equations [35–37].

In the first approach, the molecular motions are described by the Boltzmann equation and the kinetic theory of gases. The Monte Carlo simulation technique is

then used to solve the Boltzmann equation. Although this approach is fundamentally sound, it suffers from expensive computational cost. In addition to this, its application is restricted to the low pressure CVD processes, and is computationally difficult to extend this model to the ambient pressure CVD processes.

For the 1–D continuum–like diffusion–reaction formulation, molecular motions are described by the cross–sectional averaged diffusion coefficient. The resulting differential equations can then be solved analytically or numerically to depict the CVD step coverage process. The continuum–like modeling approach is straightforward and can predict good results with much less computational cost, although its way of treating the molecular transport is often questioned [38–39]. Moreover, the 1–D continuum–like diffusion–reaction model is not capable of predicting the often observed phenomenon of nonuniform deposition profiles at the trench bottom under strong molecular sticking conditions.

In chapter 2, the 1–D continuum–like diffusion–reaction model is extended into a two–dimensional (2–D) model to account for the nonuniform deposition profile phenomenon. The validity of the continuum–like diffusion–reaction modeling approach is verified by comparing the modeling predictions with the published step coverage data. Transient analysis of the step coverage process, which incorporates the moving deposition front problem, is emphasized to understand the evolution of the film conformity during the trench–filling process.

In chapter 3, the role of gas phase reactions in modeling the FCVI process is studied. The traditional single overall reaction scheme approach in modeling the kinetics of the FCVI process is extended to include both gas phase and surface reactions in the kinetic model of the FCVI process. Changes in the deposition rate

profiles resulting from the application of the forced–flow under different rate controlling regimes are the main theme of this chapter.

This study focuses on the modeling of fabrication of SiC CMCs because of their properties of high strength, high modulus, and excellent oxidation resistance at high temperatures. In chapter 4, the kinetics of silicon carbide (SiC) deposited from methyltrichlorosilane (MTS) is analyzed. Both our own hot–wall CVD data as well as reported data have been analyzed with a 1–D FEM CVD reactor model to obtain the kinetic data of the SiC films deposited from MTS/$H_2$ precursors. This FEM CVD reactor model incorporates both homogeneous gas phase and heterogeneous surface reactions.

Based on studies from the previous chapters, in chapter 5, a 2–D FEM FCVI model has been developed to study the FCVI process. Effects of deposition temperature and vapor pressure variations on the density profiles of the composite preform have been studied.

Chapter 6 provides a summary of this study on the FCVI process.

## 1.4 Presentation of Results

The results of this study are presented in the form of journal publications, which appear as separate chapters (chapter 2 to 5) following the introduction chapter. Each chapter is complete within itself, that is, each chapter has its own abstract, introduction, theory, results, discussion, and summary. The overall summary of this work is given in chapter 6. The references used are listed as chapter 7.

A paper titled

"A Two-Dimensional Step Coverage Boundary Element Model with Consideration of Moving Deposition Fronts"

was published in
Journal of Electrochemical Society
Vol. 140, No. 7, pp. 2128-2133 (1993)

Another paper titled

"Comparisons of CVD Film Conformalities Predicted by 1-D and 2-D Continuum-Like Step Coverage Models"

was submitted to
Journal of Chemical Vapor Deposition

# Chapter 2 Evaluations of the Film Conformalities by using the Step Coverage Method

## 2.1 Abstract

A two–dimensional (2–D) continuum–like diffusion–reaction model was developed to analyze the step coverage of both rectangular trenches and cylindrical contact holes with arbitrary shape under chemical vapor deposition (CVD) process. The moving boundary problem due to the film deposition was also considered in this 2–D step coverage model. The modeling predictions of $SiO_2$ step coverage using $SiH_4/O_2$ precursors were found to be in good agreement with the reported data by Kawahara et al. (1991).

The 2–D step coverage model is an improvement over the one–dimensional (1–D) step coverage model, proposed by McConica et al. (1990). The numerical error of the 1–D model, resulting from the assumption of lumped geometry, was evaluated with the variances of the two controlling parameters, that is, Damkohler number and the trench width/depth ratio, of the step coverage problem. It was found that, for the step coverage problem with high Damkohler number and trench width/depth ratio, the numerical error was too large to be neglected.

Fortran programming codes based on the boundary element method (BEM) were developed to simulate the step coverage process. The number of degrees of freedom required to run the 2–D step coverage model was reduced significantly with

the use of the BEM technique. As a result, the computational efficiency of this 2–D step coverage model is comparable to that of the 1–D step coverage model.

## 2.2 Introduction

The chemical vapor deposition (CVD) processes are widely used in industry to deposit thin solid films within submicron trenches for fabricating IC chips. Although CVD films, in general, are more conformal than films obtained by physical vapor deposition (PVD) processes, conformity of the deposition process may be lost as the trench mouth closes during the deposition process, resulting in creation of voids inside the trench. This problem is known as the step coverage problem, and is becoming a big concern with the increasing degree of miniaturization in integrated circuits.

Efforts have been devoted to modeling the step coverage problem to predict the deposition profiles under various circumstances, which may present clues to prevent the occurrence of poor step coverage.

The step coverage models can be divided into two categories: the Monte Carlo simulation of the Boltzmann equation within the trench geometry [29–34], and the 1–D continuum–like diffusion–reaction models [35–37].

The Monte Carlo simulation is a powerful tool used to solve the Boltzmann equation, which describes the molecular collisions within the submicron geometry. Although this approach is well suited to the step coverage problem, especially as the mean free path of the molecules is comparable to the characteristic dimensions of the trenches [32], the Monte Carlo simulation approaches suffer from expensive computational cost.

McConica et al. [35] used a one-dimensional (1–D) continuum–like diffusion–reaction model, originally proposed by E.W. Thiele in 1939 [40], to study the step coverage of CVD tungsten in a cylindrical contact hole. Qualitative agreements between the model's predictions and experimental results were found.

Based on the 1–D step coverage model, the deposition thickness over the trench bottom was always uniform. However, from the reported experimental results and Monte Carlo simulations of the step coverage problem [29,41], it was found that, over the trench bottom, the film thickness around the middle is always larger than near the side walls. This transverse thickness nonuniformity over the trench bottom increases with the increase of the sticking coefficient of the reactive species. Under these conditions, the 1–D step coverage model is not acceptable for predicting the appropriate thickness profiles.

In fact, there exists a concentration boundary layer, that is, a region in which concentration gradients are appreciable, near the substrate surfaces [26]. The deposition rate on the substrate is dependent on the local concentration value within the concentration boundary layer. Because the concentration boundary layer is only a small portion of the whole cross section, the step coverage based on the 1–D model, which lumped the whole transverse concentration profile into one single value, might be subject to some numerical errors depending on the experimental conditions. The limitations of the 1–D model were investigated by comparing the 1–D step coverage model with the 2–D step coverage model [42], which removed the lumped geometry assumption.

The 2–D step coverage model, proposed previously by Tsai et al. [42], was further extended to include the moving boundary problem resulting from the film deposition. This moving boundary problem was neglected previously for simplicity.

However, it is important to consider the moving boundary problem in the step coverage modeling, especially for step coverage processes designed to fill the entire trench, such as the chemical vapor infiltration (CVI) process.

In reference [42], the finite element method (FEM) was used to solve the 2–D step coverage model, which neglected the geometrical changes of the trench due to film deposition. However, the FEM technique is inefficient in updating the moving boundaries and remeshing the 2–D domain automatically during the trench–filling process. In this work, the boundary element method (BEM) was used to implement the 2–D step coverage model.

With the use of the BEM technique, the deposition rate profiles over the substrate surfaces can be obtained by considering integrations of the fundamental solutions and given variables along the 1–D string that encloses the 2–D domain. This reduced considerably the number of degrees of freedom of the problem, and allowed straightforward update of the domain as the boundaries moved.

Details of the BEM technique and the algorithm to update the deposition surfaces were given. Influences on the instantaneous deposition rate profiles and the final step coverage due to the moving deposition fronts were discussed.

## 2.3 The 2–D Step Coverage Model and Its Comparisons with the 1–D Step Coverage Model

As shown in Figure 2.1, the domain of the 2–D step coverage model consists of two portions: the area A, where diffusion of the gas species is controlled primarily by the trench dimensions; and the area B, where diffusion of the gas species is governed by the mean free path of the molecules [42]. It is interesting to note that

only the area A was considered in the 1–D step coverage model [35].

In order to compare the 1–D and 2–D step coverage models on the same basis, the deposition rates along the boundary 5 were assumed to be the same as that at the top of the boundary 3 in the following calculations. This assumption was supported by the previous study [42].

Comparisons were based on the initial stage solutions, that is, solutions with no consideration of the moving boundaries during the step coverage process. Various values of the controlling parameters were tested in order to find the range over which the lumped geometry assumption is valid.

### 2.3.1 Theory

The CVD step coverage problem can be viewed as the diffusion process of the species within the trench volume, with surface reactions of the species occurring on surfaces of the trench. Due to the small sizes of the trenches, effects of gas phase reaction were neglected. Although the chemical reactions may involve several species, it was assumed that the process is controlled by one major species.

The governing equation of the step coverage problem is Laplace equation, $\nabla^2 C=0$, where C represents the concentration of reactive species. As shown in Figure 2.1, along the boundary 1, the symmetric condition $\partial C/\partial n=0$ was used. Over the trench surfaces, that is, both boundaries 2 and 3, the assumption that the rate of mass transfer is equal to the rate of the surface reaction was used. Along the trench mouth, that is, the boundary 4, concentrations of the major species were specified, whose value $C_0$ can be determined from the deposition rate along the boundary 5.

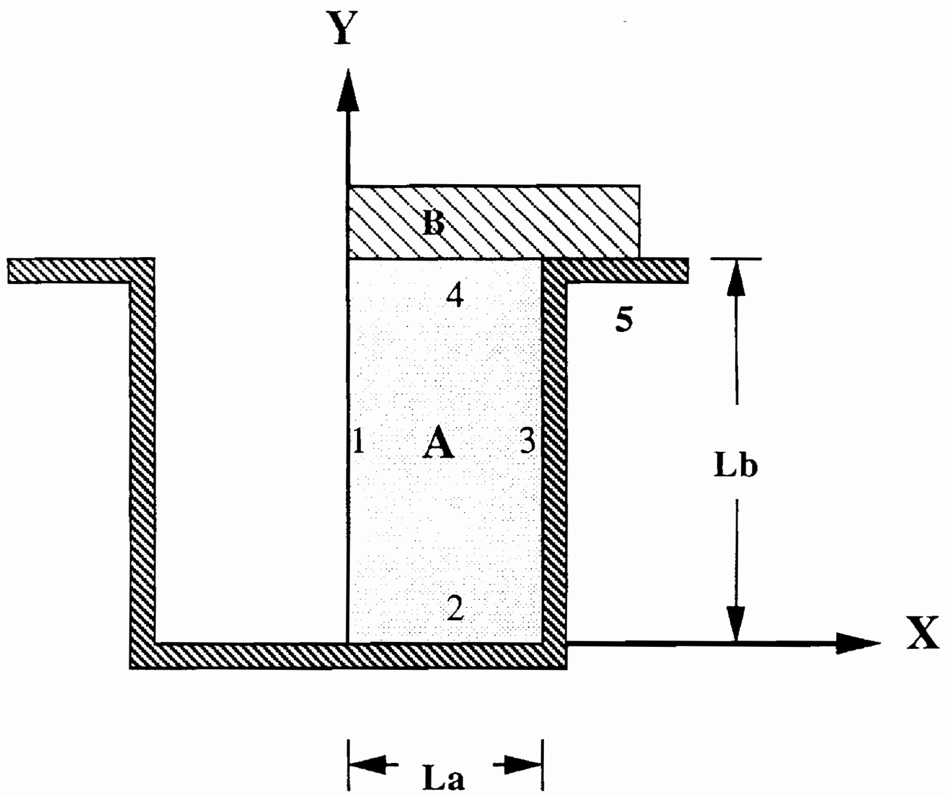


Figure 2.1 Illustrations of the Domain and Associated Boundaries Considered in the Step Coverage Modeling

With the following group of dimensionless parameters,

Equation (2.1)

$$X^* = X/L_a,\ Y^* = Y/L_b,\ D_{am} = \text{Damkohler number} = kL_b/D_k$$

$$C^* = C/C_0 = \text{Dimensionless concentration}$$

$$\lambda = L_a/L_b = \text{Half of the trench width/depth ratio}$$

the governing equation and boundary conditions of the 2–D step coverage model can be written as:

Governing Equation

$$\frac{\partial^2 C}{\partial X^2} + \lambda^2 \frac{\partial^2 C}{\partial Y^2} = 0 \tag{2.2}$$

Boundary Conditions

$$\text{Along boundary 1}: \frac{\partial C}{\partial X} = 0 \tag{2.3a}$$

$$\text{Along boundary 2}: \frac{\partial C}{\partial Y} + D_{am}\, C = 0 \tag{2.3b}$$

$$\text{Along boundary 3}: \frac{\partial C}{\partial X} + \lambda\, D_{am}\, C = 0 \tag{2.3c}$$

$$\text{Along boundary 4}: C = 1 \tag{2.3d}$$

Note that the asterisk, *, had been dropped here for clarity. Also, $D_k$ ($cm^2$/sec) is the Knudsen diffusion constant of the process, k (cm/sec) is the rate constant of the surface reaction, and $C_0$ is the species concentration (mol/$cm^3$) along the trench mouth.

The finite element formulations of the 2–D step coverage model can be written as [43]:

$$\sum_{j=1}^{n} K_{ij}^{(e)} C_{j}^{(e)} = F_{i}^{(e)} \tag{2.4a}$$

with:

$$K_{ij}^{(e)} = \int_{\Omega_e} \left(\frac{\partial N_i}{\partial X}\frac{\partial N_j}{\partial X} + \lambda^2 \frac{\partial N_i}{\partial Y}\frac{\partial N_j}{\partial Y}\right) dXdY + \int_{b_2} (\lambda^2 D_{am} N_i N_j) dS + \int_{b_3} (\lambda D_{am} N_i N_j) dS$$

$$F_{i}^{(e)} = 0 \tag{2.4b}$$

The function $N_i(X,Y)$ is the corresponding interpolation function of the finite element model. In this study, four–node linear rectangular elements were used. Fortran programming codes "FEM2D", included in the appendix of the reference [43], were modified to solve the finite element formulations above.

If the species concentration can be considered constant across the transverse direction X, the 2–D step coverage model can be lumped into the 1–D step coverage model as:

<u>Governing Equation</u>

$$-\left(\frac{\partial^2 C}{\partial Y^2}\right) + \frac{D_{am} C}{\lambda} = 0 \tag{2.5}$$

<u>Boundary Conditions</u>

$$\text{At } Y = 0,\ \frac{\partial C}{\partial Y} + D_{am} C = 0 \tag{2.6a}$$

$$\text{At } Y = 1,\ C = 1 \tag{2.6b}$$

As shown in equations (2.1–2.6), both 1–D and 2–D step coverage models are fully characterized by two controlling parameters, that is, the Damkohler number

$D_{am}$ and the geometrical factor $\lambda$, which is half of the trench width/depth ratio.

In the following, the 1–D and 2–D models were compared through the parametric study of these two controlling parameters. Solutions of the 1–D model were obtained from the exact solutions of Laplace equation with the associated boundary conditions. On the other hand, the 2–D model were solved numerically by using the finite element method.

In the FEM analysis of the 2–D step coverage model, the domain was originally divided into a 5 by 5 mesh, then the mesh number in X and/or Y directions was doubled until differences of the solutions between two consecutive steps were less than 3% of the previous solutions.

### 2.3.2 Results and Discussion

Figure 2.2a illustrated the transverse concentration profiles at axial positions of 0.9, 0.4 and 0.0 with Dam = 0.1 and trench width/depth ratio = 1.0. Under these conditions, the species concentration is almost uniform across the transverse direction, and the 1–D solutions are good approximations to the 2–D solutions. The corresponding deposition thickness profiles based on both 1–D and 2–D models are shown in Figure 2.3a. It is interesting to note that the film thickness is almost uniform across the trench bottom under these conditions.

Transverse profiles of the species concentration with Dam = 5.0 and trench width/depth ratio = 1.0 at axial positions of 0.9, 0.4 and 0.0 are shown in Figure 2.2b. The transverse concentration profiles are not uniform due to significant consumptions of the reactive species on the substrate surfaces. For example, at the axial position 0.9, the concentration level was dropped from 0.85 in the middle to

0.54 at the substrate surface. At the trench bottom, the concentration value varied from 0.08 at the middle to 0.03 at the corners. The corresponding deposition thickness profiles based on both 1–D and 2–D step coverage models are shown in Figure 2.3b. Appreciable deviations were existed between the 1–D and 2–D modeling predictions, as shown in Figures (2.2a–2.3b).

With the increase of Damkohler number from 0.1 to 5.0, the deposition thickness profile across the trench bottom based on the 2–D model started to exhibit nonuniform phenomenon. Similar results were also documented by others using the Monte Carlo simulations [29] and the Clausing–like integral equation approach [38–39]. Because of the nature of lumped geometry, the 1–D step coverage model is not capable of predicting this kind of phenomenon.

A systematic study was done to find the range of the two controlling parameters over which the lumped geometry assumption of the 1–D model is valid. The results were listed in Figure 2.4.

Values of the Damkohler number ranged from 0.01 to 20, while values of the trench width/depth ratio were varied from 0.02 to 1.0. Cases with trench width/depth ratio higher than one were not included because the formulas used to calculate the Knudsen diffusion constant, such as equation (2.14), was based on assumption of trench width/depth ratio being less than one.

In Figure 2.4, values of the numerical error, that is, $\epsilon_1$ and $\epsilon_2$, were defined as:

$$(\epsilon_1\%, \epsilon_2\%) = |U_1 - U_2| / U_2 \times 100\% \text{ at } Y/L_b = 0.9, 0.4 \qquad (2.7)$$

with $U_1$ = 1–D solution, and $U_2$ = 2–D solution

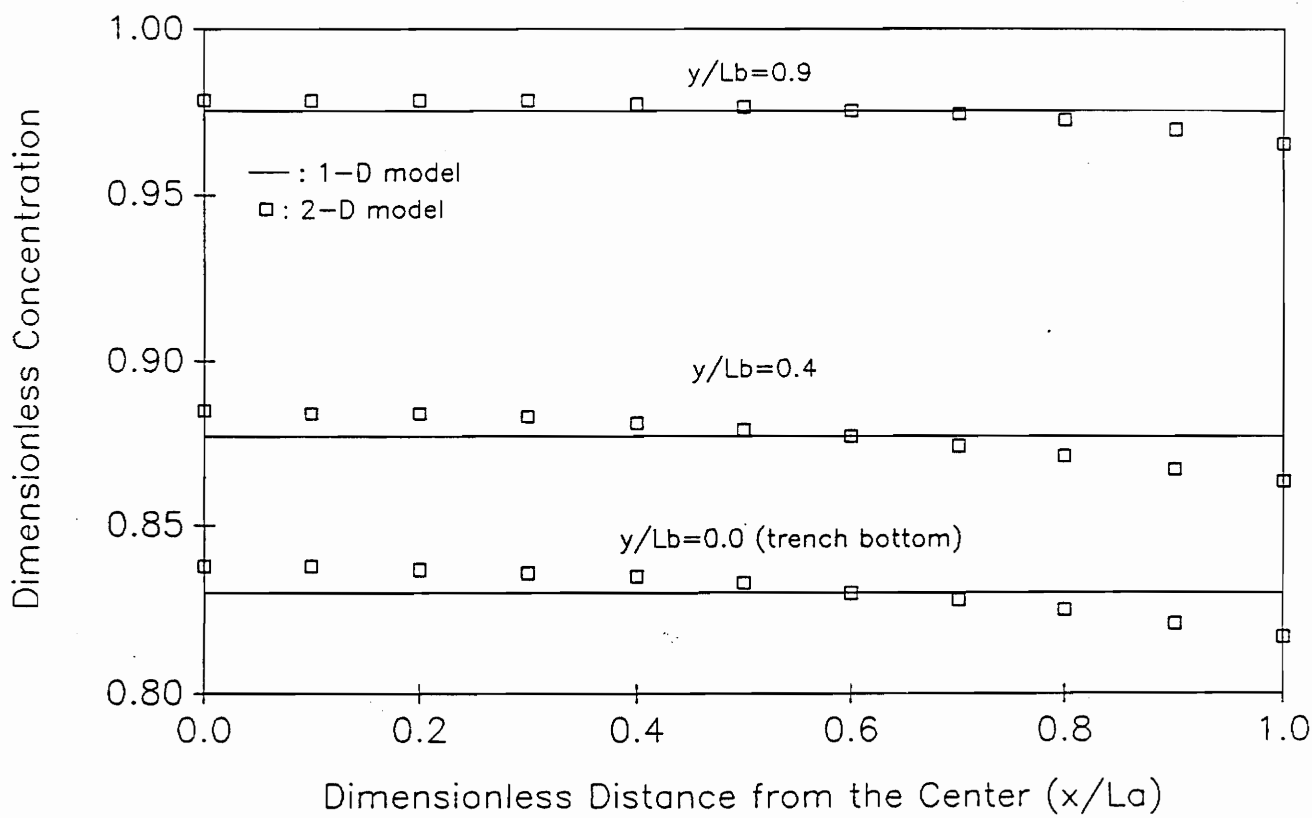


(a) $D_{am} = 0.1$ and Trench Width/Depth Ratio = 1.0

Figure 2.2 Dimensionless Transverse Concentration Profiles at $y/L_b = 0.0, 0.4, 0.9$

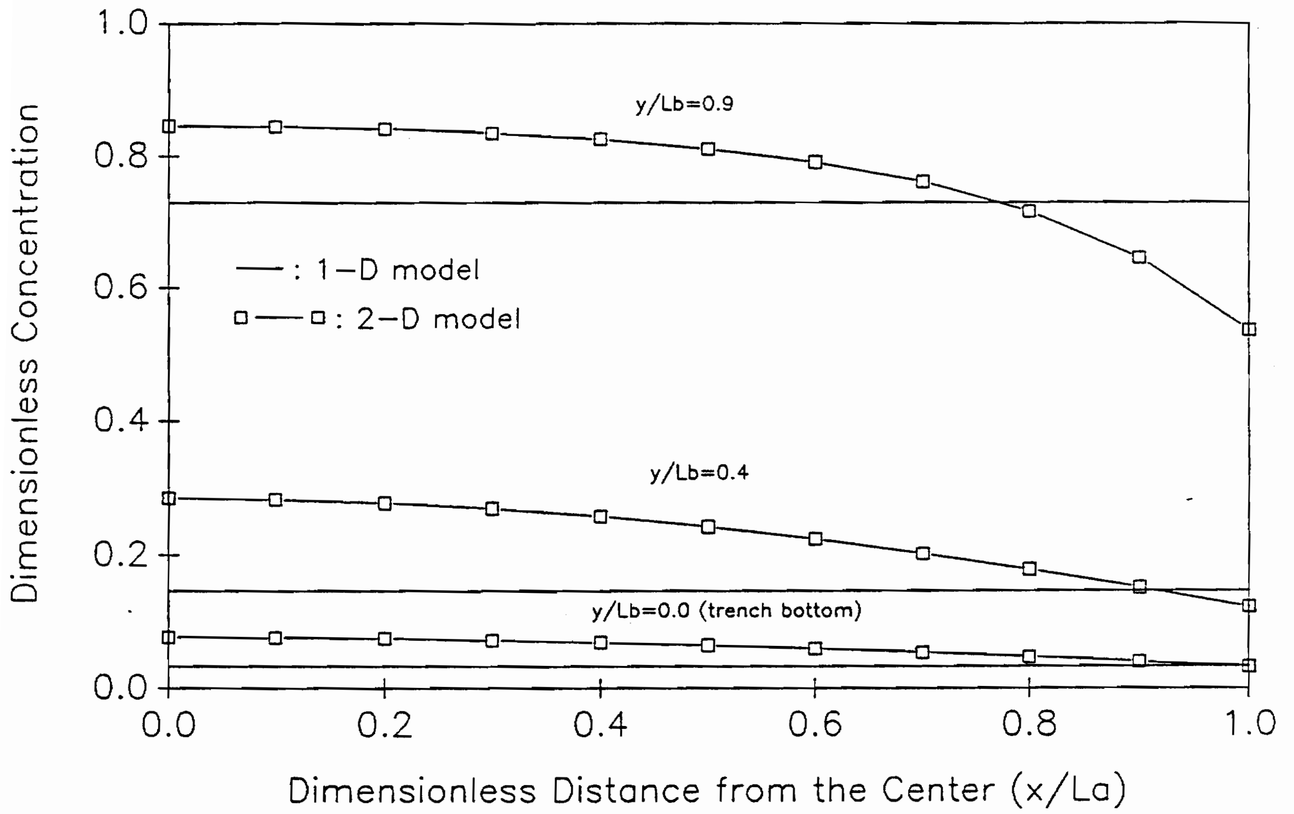


(b) $D_{am} = 5.0$ and Trench Width/Depth Ratio = 1.0

Figure 2.2 Dimensionless Transverse Concentration Profiles at $y/L_b = 0.0, 0.4, 0.9$

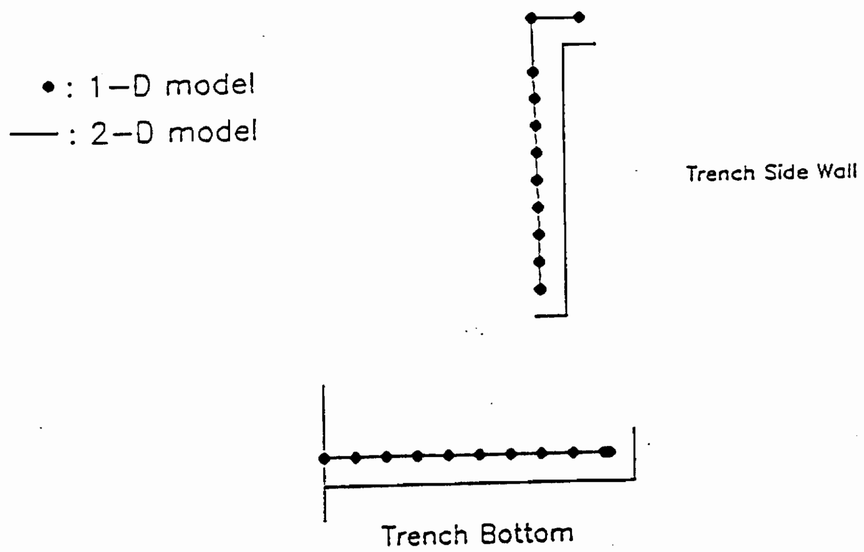


(a) $D_{am} = 0.1$ and Trench Width/Depth Ratio = 1.0

Figure 2.3 Trench Deposition Thickness Profiles

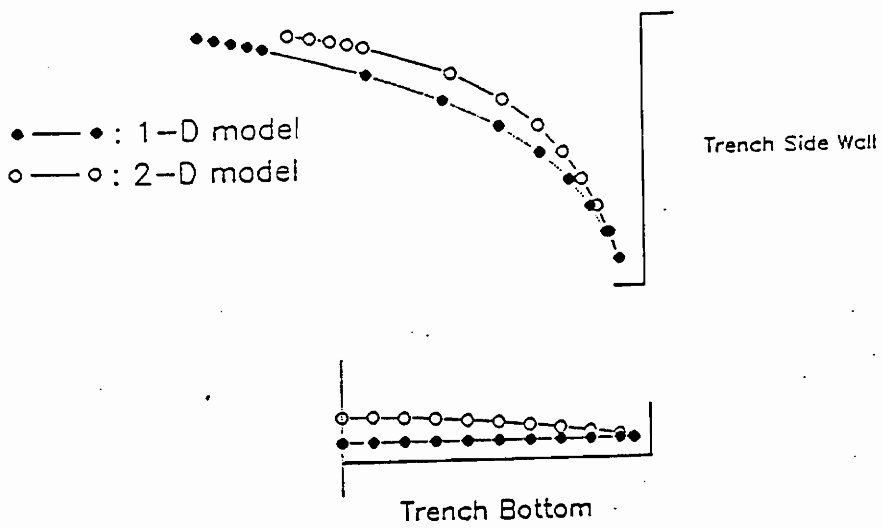


(b) $D_{am} = 5.0$ and Trench Width/Depth Ratio = 1.0

Figure 2.3 Trench Deposition Thickness Profiles

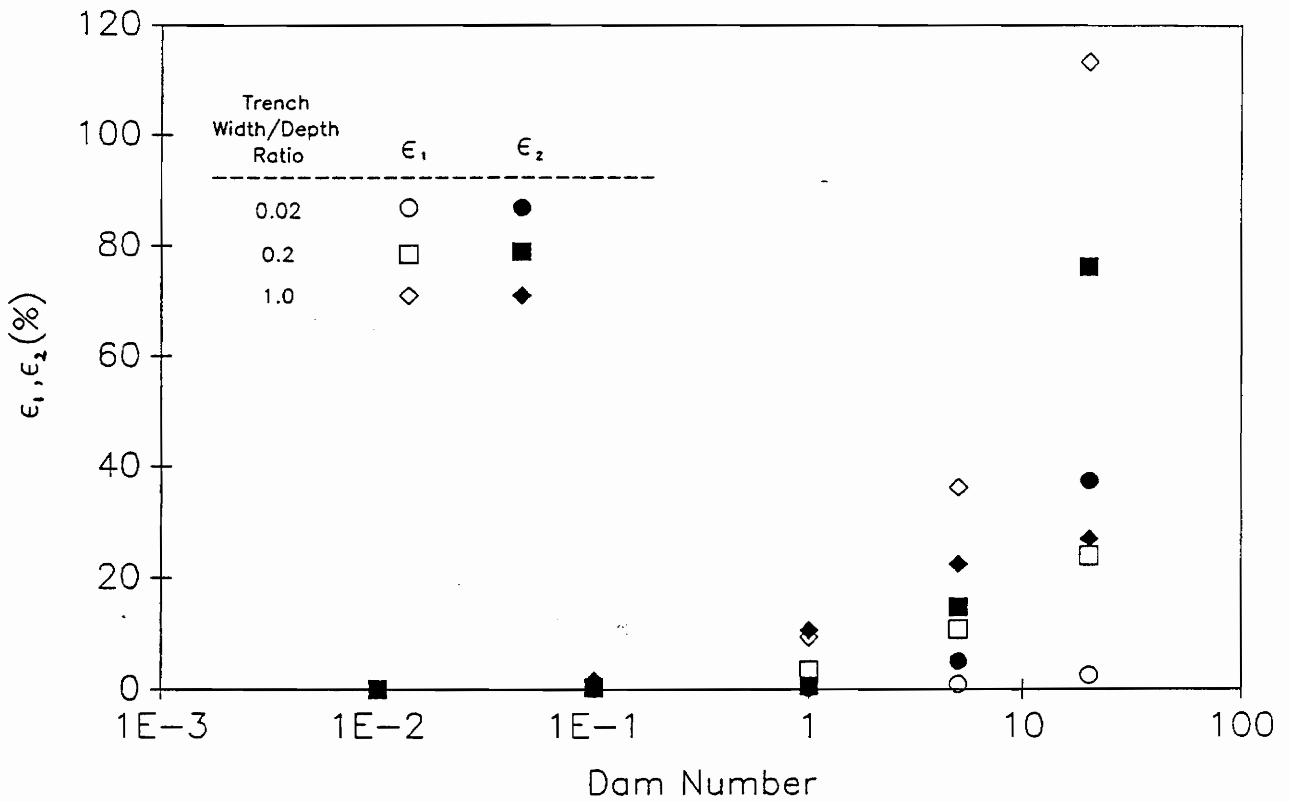


Figure 2.4 Values of the Numerical Error ($\epsilon_1$, $\epsilon_2$) of the 1–D Continuum–Like Step Coverage Model Resulting from the Lumped Geometry

As shown in Figure 2.4, the lumped geometry assumption is valid if the Damkohler number is less than 0.1. Values of the numerical error due to the lumped geometry assumption increase with increasing Damkohler number and trench width/depth ratio. For the step coverage process with Damkohler number equal to 20 and trench width/depth ratio equal to 1, the numerical error $\epsilon_1$ could be as large as 113.25%, as shown in Figures 2.4 and 2.5. Under these circumstances, the 1–D step coverage model is not appropriate for studying the step coverage process.

In general, the species concentration along the transverse direction at any particular axial position is almost uniform until very close to the substrate surfaces, where the species concentration drops due to the surface reaction. Values of the concentration gradient in the concentration boundary layer are dependent on the Damkohler number.

For a process with a small Damkohler number, the concentration gradient in the concentration boundary layer is small because only a small amount of species are being consumed on the surfaces. As a result, the lumped concentration value based on the 1–D model can provide good estimations to the concentration near the surface. However, for the step coverage processes with high Damkohler number, the 1–D model may not provide good approximations to the 2–D model due to the large concentration gradient existed in the concentration boundary layer.

Deviations between the 1–D and 2–D models may be further aggravated with increasing trench width/depth ratio. This is due to the fact that the concentration profile with sharp gradient in the concentration boundary layer, whose size is becoming smaller as compared to that of the cross section, cannot be described accurately with the average values of the whole concentration profile based on the

1–D model.

Although the 2–D model is more general than the 1–D model, the number of degrees of freedom required to solve the 2–D model is much higher than that of the 1–D model if the domain type numerical techniques, such as the finite element and finite difference methods, are used. As a result, the computational cost of the 2–D model is much more expensive than that of the 1–D model.

Moreover, for the 1–D step coverage model, it is very easy to update the moving boundaries because there are only two boundary points associated with the lumped geometry and they are not part of the irregular deposition front inside the trench.

For the 2–D step coverage model that used domain type numerical techniques to analyze the deposition thickness profiles, algorithms to update the moving boundaries and remesh the domain automatically during the trench–filling process might become very difficult because of the irregularly changing 2–D geometry resulting from the film deposition.

In the following, the boundary element method (BEM), which can reduce the dimensions of the problem domain by one, was used to calculate the deposition rate profiles and update the substrate surfaces due to deposition. Since only those points that enclose the 2–D domain have to be considered in the BEM formulation, the computational efficiency of the 2–D model is much improved, and updating algorithm is much simplified.

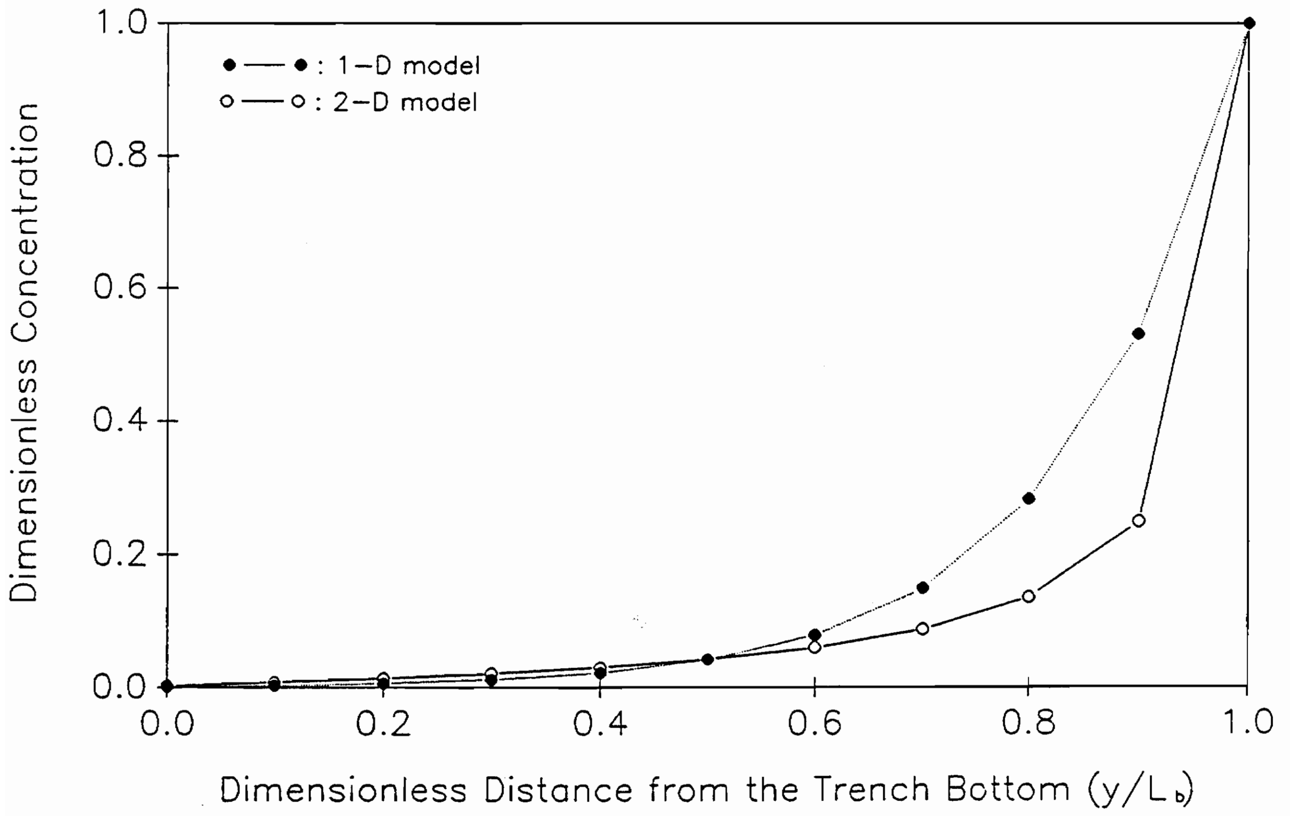


Figure 2.5 Axial Concentration Profiles along the Trench Side–Wall with $D_{am}$ = 20.0 and Trench Width/Depth Ratio = 1.0

## 2.4 The 2–D Step Coverage Model with Consideration of the Moving Deposition Fronts

During the deposition process, dimensions of the trench are continuously changing. Small amounts of reactive species can reach deep inside the trench due to the closing of the trench mouth. As a result, CVD thin films with good step coverage initially might end up with poor step coverage. Therefore, it is very important to consider the changing geometry of the trench in order to correctly predict the final step coverage.

In the following, the BEM formulation of the 2–D step coverage model and the algorithm to update the changing boundaries were introduced. The BEM step coverage model was then used to study the step coverage of $SiO_2$ deposited from $SiH_4/O_2$ precursors.

### 2.4.1 Theory

#### 2.4.1a Boundary Element Formulation of the Step Coverage Process

The boundary element method is an alternative technique which offers important advantages over the domain type solutions, such as the finite element method and the finite difference method. One of the most interesting features of the BEM technique is the considerable reduction of the number of degrees of freedom required to run the problem [44,45].

For the BEM technique, only the 1–D string that encloses the 2–D domain, shown in Figure 2.1 as 1–2–3–4 segment, has to be considered in the formulation. It

is obvious that the BEM technique is well suited to the 2–D step coverage model since only concentrations at the substrate points, which are parts of the 1–D boundary string, are interested. This desirable feature of the BEM technique also makes the boundary update scheme much easier as compared with those of the finite element and finite difference techniques. The basic concept of the BEM formulation is introduced as follows.

With the use of the weighted residual method [45], the following expression can be deduced from Laplace equation, $\nabla^2 U=0$, on a domain $\Omega$:

$$\int_{\Omega} U(\nabla^2 U^*)d\Omega = -\int_{\Gamma_2} \overline{Q}U^*d\Gamma - \int_{\Gamma_1} QU^*d\Gamma + \int_{\Gamma_2} UQ^*d\Gamma + \int_{\Gamma_1} \overline{U}Q^*d\Gamma \quad (2.8)$$

In the above expression, $U^*$ is the weighting function that has continuous first derivatives within the domain $\Omega$, Q is the normal derivatives of U, that is, $\partial U/\partial n$, and $Q^*$ is equal to $\partial U^*/\partial n$. The corresponding boundary conditions of the problem can be either of the essential type boundary conditions, that is, $U=\overline{U}$, along the portion of boundary $\Gamma_1$, or the natural type boundary conditions, that is, $Q=\overline{Q}$, over the portion of boundary $\Gamma_2$.

If the weighting function $U^*$ is chosen such that at a point i the equation $\nabla^2 U^*+\delta_i=0$ is satisfied, the equation (2.8) can be written as:

$$U^i + \int_{\Gamma_2} UQ^*d\Gamma + \int_{\Gamma_1} \overline{U}Q^*d\Gamma = \int_{\Gamma_2} \overline{Q}U^*d\Gamma + \int_{\Gamma_1} QU^*d\Gamma \quad (2.9)$$

Solutions of the equation $\nabla^2 U^*+\delta_i=0$ are called the fundamental solutions, where $\delta_i$ is the Dirac delta function.

The equation (2.9) is valid for any point in the domain. With the consideration of only the boundary points, the equation (2.9) can be simplified as:

$$0.5U^i + \int_{\Gamma} UQ^* d\Gamma = \int_{\Gamma} QU^* d\Gamma \tag{2.10}$$

with $\Gamma = \Gamma_1 + \Gamma_2$.

For a smooth boundary that are divided into n segments, the equation (2.10) can be written as:

$$0.5U^i + \sum_{j=1}^{n} \int_{\Gamma_j} UQ^* d\Gamma = \sum_{j=1}^{n} \int_{\Gamma_j} QU^* d\Gamma \tag{2.11}$$

From equation (2.11), the solution at the boundary point i can be obtained by integrating the fundamental solutions and variables along the boundaries only. The boundary element model for the system of n boundary nodes can be expressed in the matrix form as:

$$[H]\{U\}=[G]\{Q\} \tag{2.12a}$$

with:

$$H_{ij} = \int_{\Gamma_j} U^* d\Gamma, \text{ when } i \neq j; \quad H_{ij} = 1/2 + \int_{\Gamma_j} Q^* d\Gamma, \text{ when } i=j \tag{2.12b}$$

$$G_{ij} = \int_{\Gamma_j} U^* d\Gamma \tag{2.12c}$$

With the specification of either the concentration, $\overline{U}$, or the flux, $\overline{Q}$, solutions at the n boundary points can be obtained from equations (2.12a–2.12c). For the 2–D step coverage problem, since the boundary conditions on the substrate surfaces are of the Robin type conditions, that is, $Q_i+EU_i=0$, neither the concentration U nor the flux Q is specified. However, the relationship $\{Q\} = -[E]\{U\}$ can be substituted into the equation (2.12a) to provide the solvable system of equations $([H]+[G][E])\{U\}=\{0\}$. After solving the system of equations for the primary variables at the substrate boundary points, values of the flux at those points can be computed from the relationship $Q_i+EU_i=0$.

In order to perform the integrations of both equations (2.12b) and (2.12c), the fundamental solution $U^*$ must be obtained in advance from the equation $\nabla^2U^*+\delta_i=0$. The fundamental solution $U^*$ for both rectangular and cylindrical coordinate systems can be written as [44–45]:

$$U^* = 1/(4\pi r) \text{ for the 3–D rectangular coordinate system (X,Y,Z)}$$

$$U^* = \ln(1/r)/2\pi \text{ for the 2–D rectangular coordinate system (X,Y)}$$

$$U^* = 4K(m)/\sqrt{(a^2+b^2)} \text{ for the 2–D axisymmetric coordinate system (R,Z)}$$

with:

K(m): The complete elliptic integral of the first kind

r: The distance between the point of application of Dirac delta function and the point considered

a,b: $a=R^2(\xi)+R^2(X)+\{Z(\xi)-Z(X)\}^2$, $b=2R(\xi)R(X)$, with $\xi$ be the point of application of Dirac delta function and X be the point considered

The Fortran codes included in the reference [45] were modified to calculate the deposition rate profiles of the step coverage problem. Linear elements were used in the BEM model.

### 2.4.1b Scheme for Updating the Substrate Surfaces during the Deposition Process

With the implementation of the BEM technique in the 2–D step coverage model, we were able to calculate the deposition rate profiles on the trench surfaces by integrating the fundamental solution and variable along the string that encloses the 2–D domain. Since only the 1–D string has to be considered, the procedure of updating the deposition front of the trench is much simplified.

An approach that is similar to the string–advancing algorithm [46] was used in this study to update the trench surfaces due to the film deposition. The schematic diagram of the string moving algorithm was shown in Figure 2.6. For those non–corner points, the direction of the segment movement was assumed to be perpendicular to the current substrate surface at that point. The magnitude of the movement is proportional to the species concentration at that point. On the other hand, advancements of those corner points were determined by the intersection of the two adjoining surfaces.

### 2.4.2 Results and Discussion

So far, the 2–D step coverage model and its associated string–moving algorithm to update the moving boundaries has been presented. For each CVD system, the Knudsen diffusion constant, $D_k$, and the reaction rate constant, k, have to be

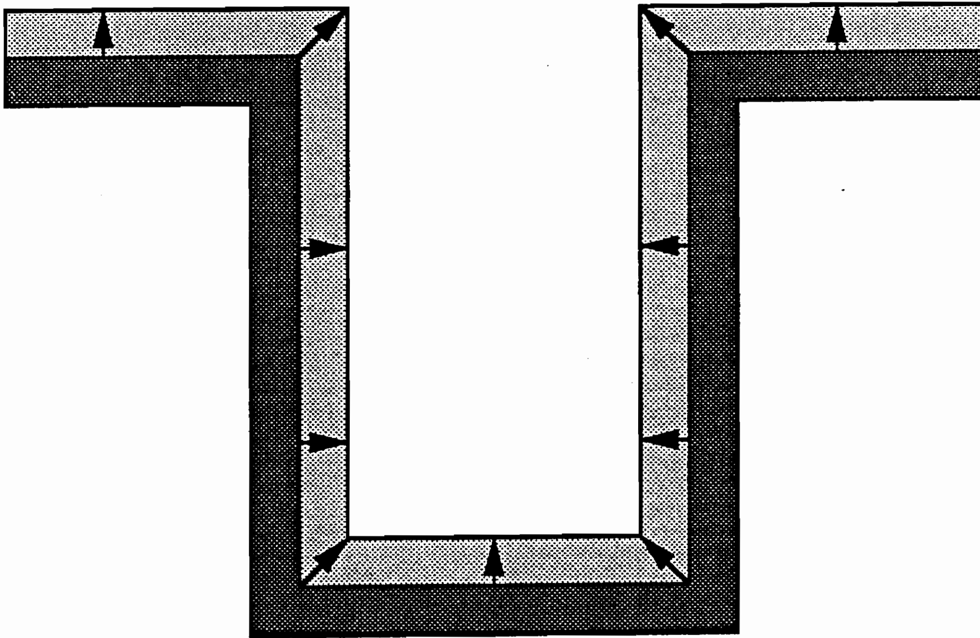

Figure 2.6 Illustrations of the String Advancing Algorithm Used to Update the Deposition Fronts

specified in order to calculate the deposition rate profiles.

The Knudsen diffusion constant can be determined from the following expression [47],

$$D_k(t)\ (cm^2/sec) = 3638L_b(t)\sqrt{T/M}\ /\ (1+3L_b(t)/8W(t))$$
$$= 3638L_b(t)\sqrt{T/M}\ /\ (1+3L_b(t)/16L_a(t)) \quad (2.13)$$

with:

M: Molecular weight of the gas species (gm/mole)

T: Deposition temperature (°K)

W: Trench width (cm)

$L_b$: Trench depth (cm)

Note that for the pores with the trench width/depth ratio being much lower than one, the equation (2.13) can be reduced to the familiar equation [27]:

$$D_k(t) = 9700L_a(t)\sqrt{T/M} \quad (2.14)$$

The reaction rate constant, k, is dependent on the particular CVD system. For the deposition of $SiO_2$ from the precursors $SiH_4/O_2$, the rate constant k can be estimated from the following expression [33],

$$k\ (cm/sec) = 0.25S_cV_t \quad (2.15)$$

where:

$S_c$ is the sticking coefficient of the reactive species, and $V_t$ is the mean thermal velocity of the reactive species given by $\sqrt{8kT/(\pi M)}$ (cm/sec).

For the deposition of $SiO_2$ from the precursor $SiH_4/O_2$, the overall sticking coefficient and deposition rate reported by Kawahara et al. (1991) are listed in Table 2.1 [41]:

Table 2.1

The Temperature Dependence of Deposition Rates and Sticking Coefficients of $SiO_2$ Thin Films Deposited from $SiH_4/O_2$ Precursors

| T(°K) | $\beta$ | DR(Å/min) |
|---|---|---|
| 450 | 0.697 | 35.62 |
| 520 | 0.359 | 41.78 |
| 540 | 0.200 | 43.15 |
| 640 | 0.055 | 43.15 |

$\beta$ — Sticking Coefficient

DR — Deposition Rate

For the calculation of the concentration $C_0$ (mol/cm$^3$), the following expression was used [33]:

$$\text{Deposition Rate (mol/cm}^2\text{–sec)} = 0.25 S_c V_t C_0 \qquad (2.16)$$

Density of the $SiO_2$ thin film was assumed to be 2.19 gm/cm$^3$. For the calculations of the Knudsen diffusion constant and the mean thermal velocity, the molecular weight was taken to be that of $SiH_2$, or, 30.09 gm/mole. Although other species, such as $SiH_3$, might also be responsible for the deposition of the $SiO_2$ from the $SiH_4/O_2$ system [29], differences between their molecular weight and that of $SiH_2$ are small.

Simulation results were compared with the experimental results reported by Kawahara et al. [41] in Figure 2.7. The step coverage is defined as $t_{min}/t_{max}$, where $t_{min}$ is the minimum film thickness on the side walls, and $t_{max}$ is the film thickness on the flat surface, that is, the boundary 5. In Figure 2.7, both initial step coverage and the step coverage when $t_{max}=0.1L_b$, which was the condition of the reported step coverage data, were presented.

In this study, the time interval was chosen such that increments of the deposition thickness at the trench mouth were less than 5% of the current trench width. With this consideration, the steady state solutions were good approximations to the transient solutions within each time interval, since the reactive species can reach the steady state very quickly. Because the time increment was allowed to be adjusted automatically according to the updating trench geometry, the balance between the computation time and accuracy can be achieved.

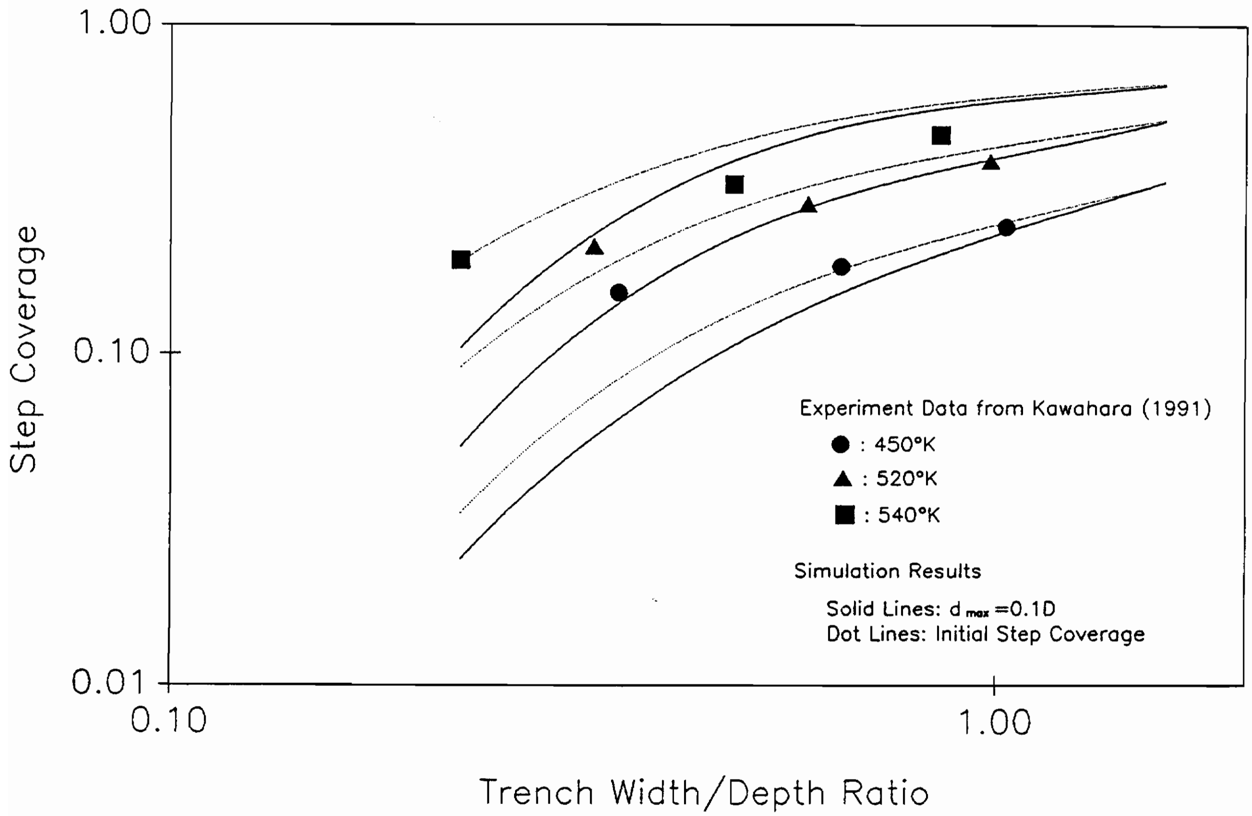


Figure 2.7 Comparisons of the Modeling Predictions and Experimental Results of $SiO_2$ Step Coverage Using $SiH_4/O_2$ Precursors

As shown in Figure 2.7, the predicted step coverage is in good agreement with the reported experimental data. In general, for the $SiO_2$ CVD process using $SiH_4/O_2$ precursors, as the deposition temperature increases, the overall sticking coefficient decreases. Because the Damkohler number decreases with respect to the temperature increase according to equations (2.13–2.15) , the step coverage improves with the increase of the deposition temperature. This feature was also found by Watanabe et al. [33] and Ikegawa et al. [34].

To study the effect of the moving deposition fronts on the step coverage during the deposition process, deposition thickness profiles with the trench widths equal to $0.5\mu m$, $1.25\mu m$; and deposition temperatures equal to $540^\circ K$ and $640^\circ K$ are shown in Figures (2.8a–2.8d). The trench depth is 2.5 $\mu m$ for these cases. For these two deposition temperatures, the deposition rate at the trench mouth is about the same, while the ratio of the two sticking coefficients is 3.64, as shown in Table 2.1.

Axial concentration profiles for these cases are also shown in Figures 2.9a–2.9d. Note that coordinates of the two end points of each curve in Figures 2.9a–2.9d are different due to the deposition occurred on the trench bottom and mouth during the step coverage process.

For the trench with an opening width of $0.5\mu m$ and deposition temperature of $540^\circ K$, very few reactive species can reach to the trench bottom during the whole trench–filling process. The concentration level at the trench bottom was only 15.7% of that at the trench mouth initially. After approximate an hour, this concentration percentage dropped down to 3.8%, and the step coverage was changed from 0.16 initially to 0.082.

For the same trench sizes, as the deposition temperature was increased to $640^\circ K$, the axial concentration profiles were much more uniform initially due to the

lower sticking coefficient, as shown in Figure 2.9b. The concentration level at the trench bottom was increased to 48.5% of that at the trench mouth in the beginning. This concentration percentage was decreasing during the step coverage process because of the narrowing trench width and elongating trench depth. As shown in Figure 2.9b, after 27.15 minutes, this value was changed from 48.5% to 26.1%. Thereafter, film depositions on the trench bottom became scarce. The step coverage changed from 0.49 initially to 0.28 in 51.27 minutes.

As illustrated above, the final $SiO_2$ step coverage was improved from 0.082 to 0.28 by increasing the deposition temperature from 540°K to 640°K. Another way to improve the step coverage is to enlarge the trench width. If the trench mouth width was changed from 0.5$\mu$m to 1.25$\mu$m, the final $SiO_2$ step coverage can be improved from 0.082 to 0.26 with the deposition temperature still equal to 540°K. The deposition thickness and axial concentration profiles of this case were shown in Figures 2.8c and 2.9c. In this calculation, the trench mouth closing time was 138.2 minutes as compared to 51.2 minutes of the trench with 0.5 $\mu$m trench width.

If both strategies were used, the $SiO_2$ step coverage can be improved significantly, as shown in Figure 2.8d. The axial concentration profile with the conditions of low sticking coefficient and high Knudsen diffusion constant was almost uniform initially, as shown in Figure 2.9d. At the beginning, the concentration value at the trench bottom was 76.8% of that at the trench mouth. After 94.35 minutes, this percentage was dropped to 45.1%, which is still higher than the initial concentration value with 540°K deposition temperature, as shown in Figure 2.9c. The final step coverage was 0.54, which is about two folds of the final step coverage with 540°K deposition temperature and 1.25$\mu$m trench width.

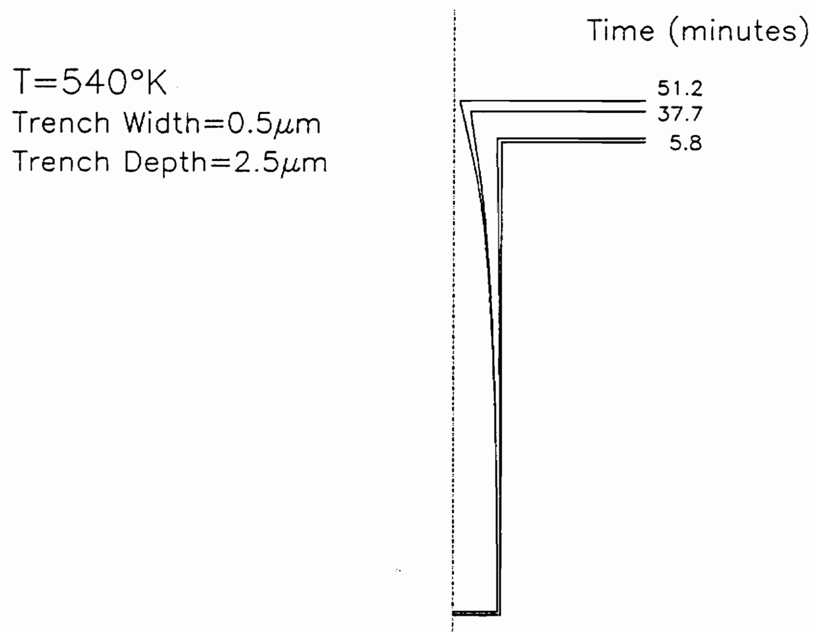


(a) Trench Width = $0.5\mu m$, Trench Depth = $2.5\mu m$

Deposition Temperature = $540^\circ K$

Figure 2.8 Trench Deposition Thickness Profiles

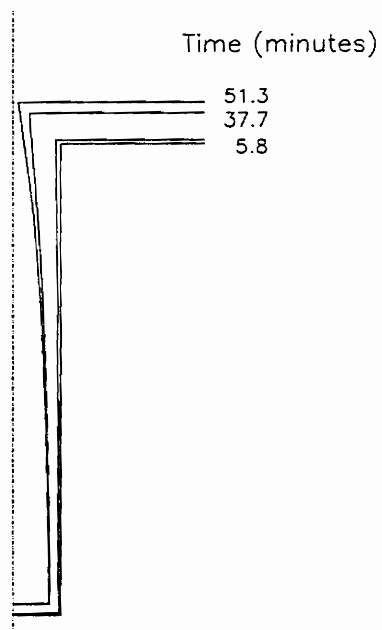


(b) Trench Width = 0.5$\mu$m, Trench Depth = 2.5$\mu$m

Deposition Temperature = 640° K

Figure 2.8 Trench Deposition Thickness Profiles

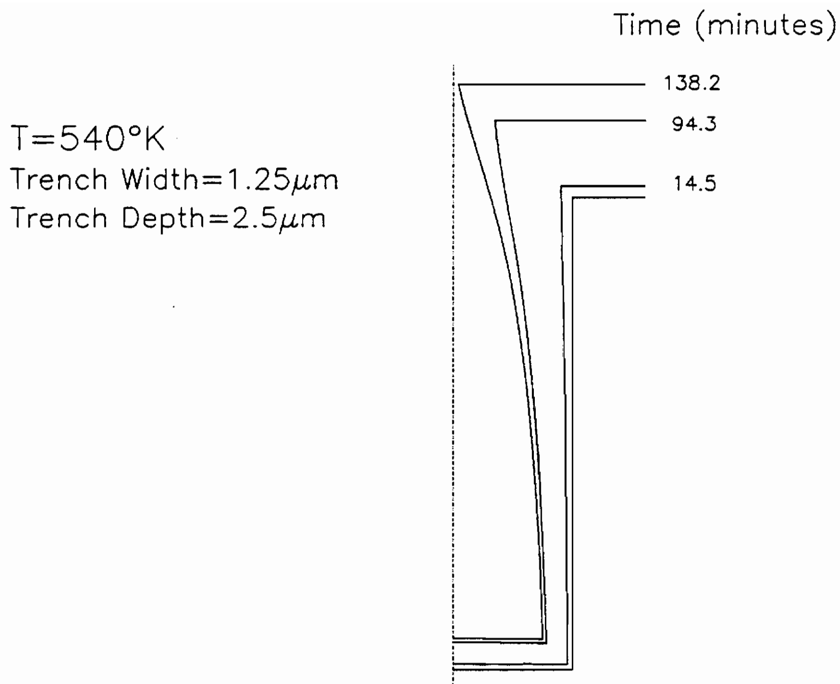


(c) Trench Width = 1.25$\mu$m, Trench Depth = 2.5$\mu$m

Deposition Temperature = 540° K

Figure 2.8 Trench Deposition Thickness Profiles

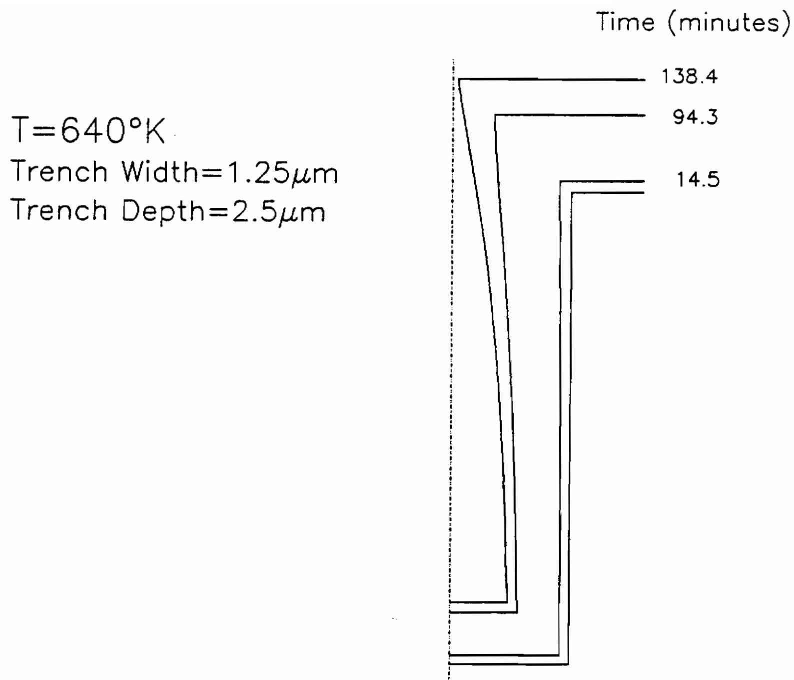


(d) Trench Width = 1.25$\mu$m, Trench Depth = 2.5$\mu$m

Deposition Temperature = 640° K

Figure 2.8 Trench Deposition Thickness Profiles

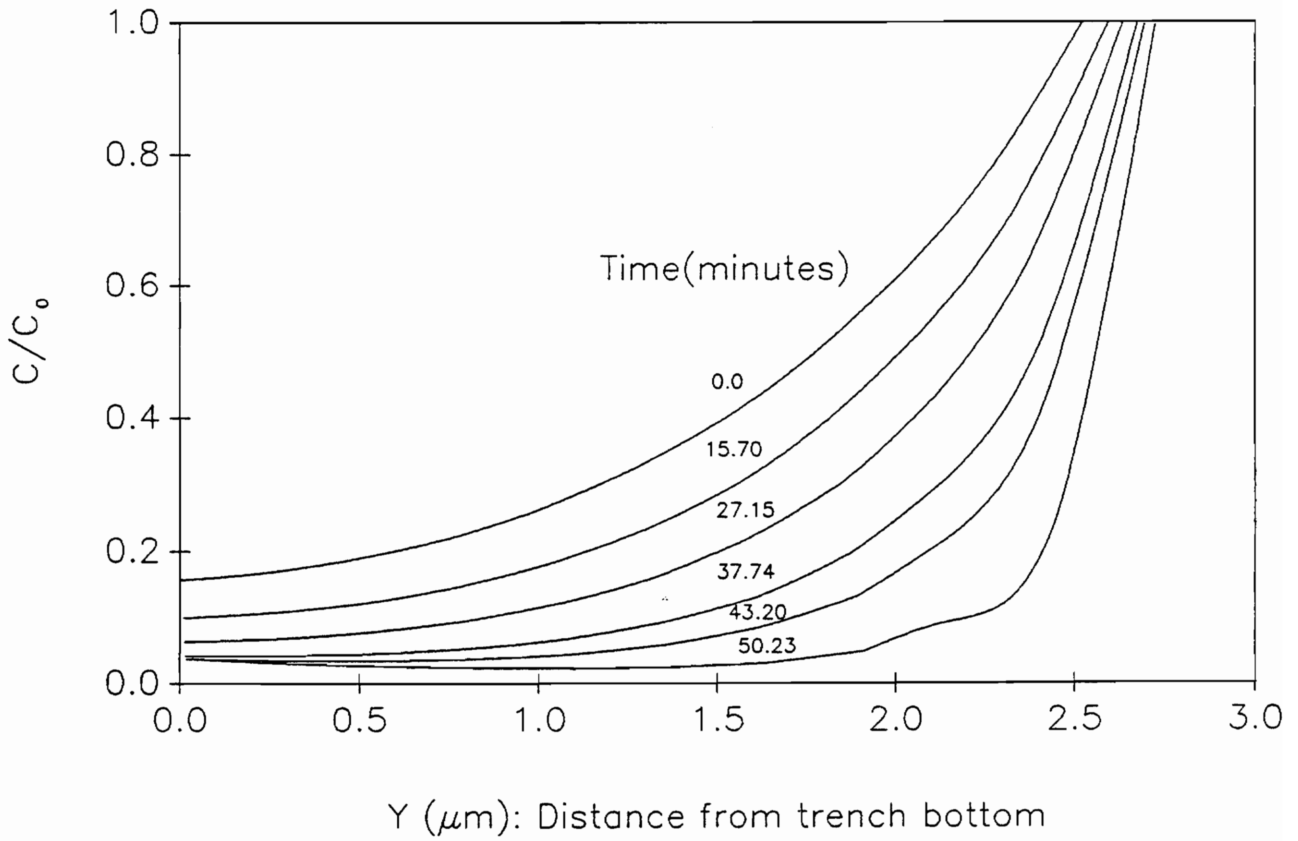


(a) Trench Width = 0.5$\mu$m, Trench Depth = 2.5$\mu$m

Deposition Temperature = 540° K

Figure 2.9 Axial Concentration Profiles along the Trench Side–Wall

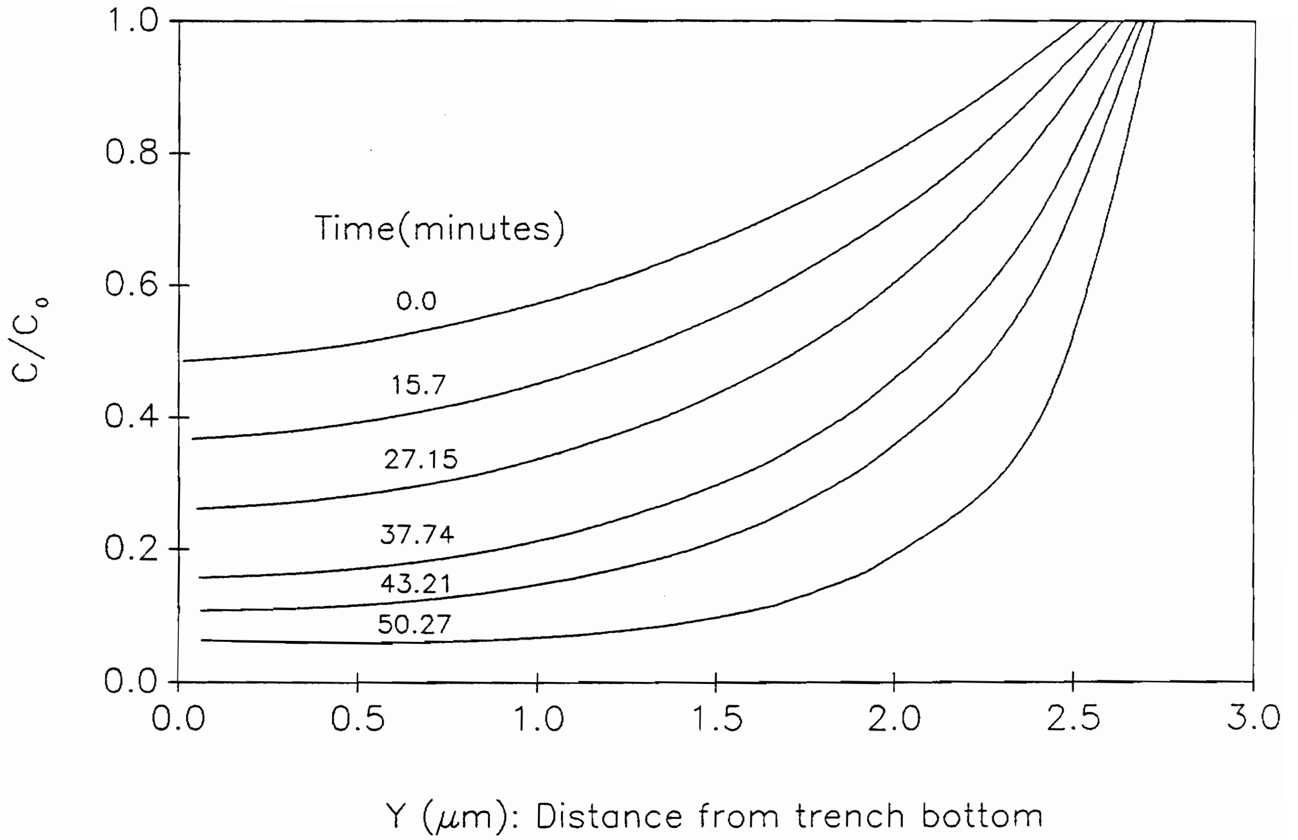


(b) Trench Width = $0.5\mu m$, Trench Depth = $2.5\mu m$

Deposition Temperature = $640^{\circ}$ K

Figure 2.9 Axial Concentration Profiles along the Trench Side–Wall

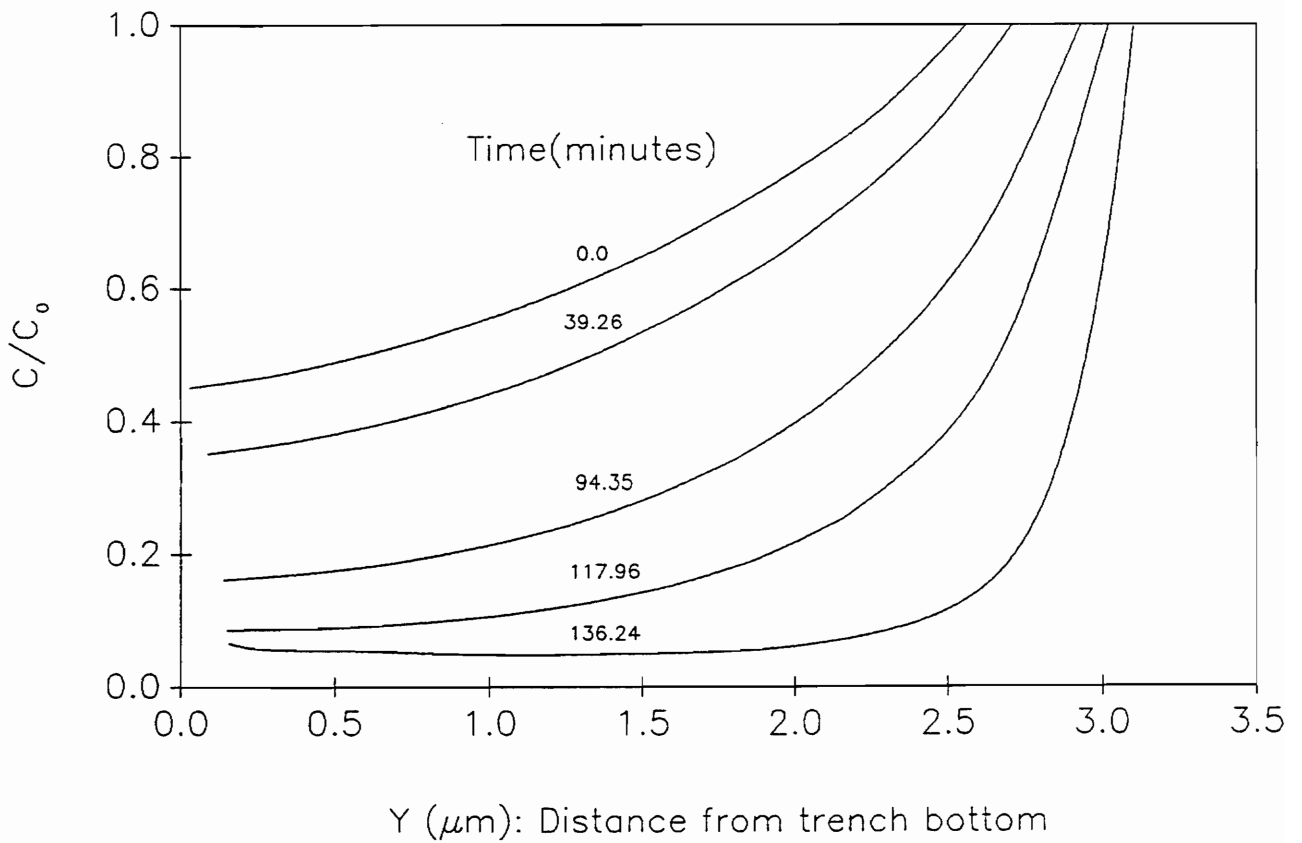


(c) Trench Width = 1.25$\mu$m, Trench Depth = 2.5$\mu$m

Deposition Temperature = 540°K

Figure 2.9 Axial Concentration Profiles along the Trench Side–Wall

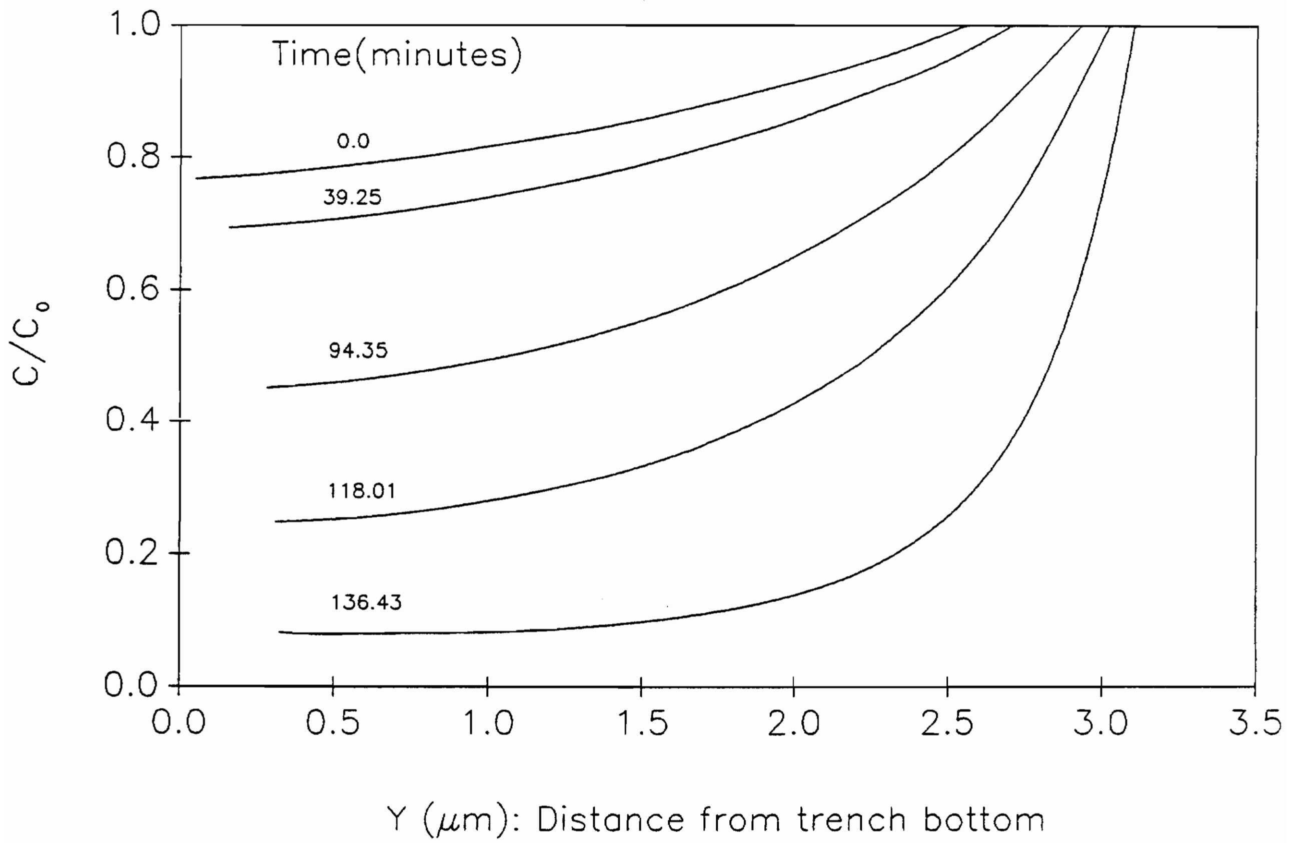


(d) Trench Width = 1.25$\mu$m, Trench Depth = 2.5$\mu$m

Deposition Temperature = 640° K

Figure 2.9 Axial Concentration Profiles along the Trench Side–Wall

## 2.5 Summary

A 2–D continuum–like step coverage model, which includes the effect of the moving deposition fronts, was presented in this paper. The BEM technique was used to solve the 2–D step coverage problem. Since only the 1–D string that encloses the 2–D trench domain has to be considered in the BEM formulations, the number of degrees of freedom of the problem is reduced significantly, and procedures to update the moving boundaries during the step coverage process become very simple. As a result, the computational efficiency of this 2–D step coverage model is greatly enhanced and is comparable to that of the 1–D step coverage model.

Numerical results of the 2–D step coverage model were compared with the reported $SiO_2$ step coverage data using $SiH_4/O_2$ precursors. Agreements between the reported data by Kawahara et al. (1990) and the modeling calculations were found to be good. It was also found that considerations of the moving deposition surfaces are important in predicting the final step coverage, especially for those with high initial step coverage.

Values of the numerical error for the 1–D step coverage model, resulting from the lumped geometry assumption, was evaluated by comparing with this 2–D step coverage model. It was found that for the step coverage with the Damkohler number being lower than 0.1, the 1–D step coverage model can provide excellent approximations to the 2–D step coverage model. However, under high Damkohler number and trench width/depth ratio conditions, such as the case with 20.0 Damkohler number and 1.0 trench width/depth ratio, the numerical error might be as high as 113.25%. Under these circumstances, the use of the 1–D step coverage model is not suggested.

Moreover, due to the assumption of lumped geometry, the 1–D step coverage model is incapable of predicting the occurrence of nonuniform thickness profile over the trench bottom with increasing sticking coefficient. This phenomenon can be simulated by other techniques, such as the Monte Carlo simulation and the Clausing–like integral equation approach. The 2–D step coverage removed the lumped geometry assumption and is capable of predicting this kind of phenomenon.

It is concluded that although the 1–D step coverage model is simple and can closely approximate the 2–D model under low Damkohler number and trench width/depth ratio conditions, deviations between the 1–D and 2–D models may become too large to be neglected as both the Damkohler number and trench width/depth ratio are increasing.

This paper titled

"The Role of Gas-Phase Reactions in Modeling of the Forced-Flow Chemical Vapor Infiltration Process"

was published in
Journal of Electrochemical Society
Vol. 140, No. 7, pp. 2121-2124 (1993)

# Chapter 3 The Role of Gas–Phase Reactions in Modeling of the Forced–Flow Chemical Vapor Infiltration Process

## 3.1 Abstract

An analytical model is presented, which includes the effects of both gas–phase and surface reactions, and the pressure changes due to the chemical reactions in the forced–flow chemical vapor infiltration (FCVI) process.

For the FCVI process controlled by the gas–phase reactions, improvements of the process by using the forced–flow are limited. However, for the FCVI process controlled by the surface reactions, the process can be improved with the use of the forced–flow technique.

For the surface reaction controlled FCVI process, the degree of improvement increases with increasing permeability of the composite preform. In other words, advantages due to the forced–flow are higher at the initial stage of the process when the porosity of the composite preform is high.

## 3.2 Introduction

Ceramic matrix composites (CMCs) can be fabricated by infiltrating the composite preform with gas precursors containing the elements of the matrix. The gas precursors react inside the porous composite preform to form the matrix of the composite. This fabrication method is known as the chemical vapor infiltration (CVI) technique.

Because of the cost and slow rates of deposition, the chemical vapor infiltration process was initially viewed as a useful technique only for coating fibers rather than as a means for forming the matrix. However, the CVI technique has received a lot of attention recently as a strong candidate for the fabrication of CMCs because of its versatility in creating all major families of ceramic matrices by a single, continuous deposition step; low processing temperature capability; and geometry–preserving features.

One of the critical issues associated with the CVI technique is that the matrix usually deposits more rapidly at the outer sides of the composite, and thus a large amount of trapped porosity remains inside the composite. The resultant CMCs with high porosity do not have good mechanical properties. Several techniques such as grinding of the blocked pores, imposition of a thermal gradient, and the forced–flow CVI (FCVI) process [6], have been used in order to alleviate this serious problem.

In addition to those techniques mentioned above, extensive work is being carried out in the area of the CVI process modeling [7–17,23,28] to better understand the process. The modeling results can serve as a basis for choosing experimental conditions and preform geometry so that desirable properties of the

resultant CMCs can be achieved.

A self–consistent CVI model usually consists of three sub–models, covering chemical reactions, transport processes, and preform geometry, respectively.

With the complexity and randomness associated with the geometry of the fibrous preform, it is extremely difficult to have a precise and full scale description of the fibrous preform. Several structure element models, such as the single pore model [7–10], overlap pore model [11], unit–cell model [13–14], and effective medium model [15–16] were proposed to mimic the composite preform thus leading to a tractable analysis of the infiltration process.

As for the transport process, the diffusion of the gas species is assumed to be the main transport mechanism [7–9,11,13,15]. Depending on the CVI process to be modeled, convective flow (forced–flow) was also incorporated [10,14,16–17].

Most of the traditional CVI models lumped the chemical reactions into one single overall reaction for simplicity [8–9,11–17]. Recently, Middleman [7] and Sheldon [23] investigated the importance of controlling the gas–phase kinetics in the traditional CVI process in order to optimize the densification profiles. Both Middleman and Sheldon have shown that by controlling the gas–phase kinetics, it is theoretically possible to have faster matrix deposition in the middle of the composite, and thus eliminate the premature pore blockage problem.

The gas–phase reaction was also included in the study of the chemical vapor deposition (CVD) process by Desu et al. [24] to determine the rate controlling step of the CVD processes. It was shown that deposition rate profiles were significantly different for CVD processes controlled by different reactions. For the CVD processes controlled by the gas–phase reaction, the deposition rate profiles decrease with an increase in the flow velocity. These results suggest that advantages of the

FCVI may be limited.

Most of the models that were proposed for the FCVI process [14,16–17] neglect the contribution of gas–phase reactions even though their importance has been documented for both the traditional CVI process and the CVD process as mentioned above. In this work, an analytical model, which incorporates the effects of gas–phase and surface reactions in the FCVI process, is presented. The pressure buildup due to both chemical reactions and the applied external pressure was considered. The model is nonlinear due to the viscous flow terms resulting from the pressure gradient. The finite element method (FEM) was used to solve the problem numerically. Changes of the deposition rate profiles resulting from the application of the forced flow under different rate controlling regimes are the main subjects of this study.

### 3.3 Mathematical Modeling of the Forced–Flow CVI Process

For the study of the FCVI process with both gas–phase and surface reactions, it is assumed that the reagent species, $SP_{1(g)}$, which is diluted in the inert gas, $DG_{5(g)}$, is decomposed into the gas–phase intermediate species, $IP_{2(g)}$, and the by–product, $BP_{3(g)}$. The intermediate species, $IP_{2(g)}$, is adsorbed onto the surface of the growing film, and react to produce the solid film, $Film_{(s)}$, and the other by–product, $BP_{4(g)}$. The whole process is described in equations (3.1–3.2):

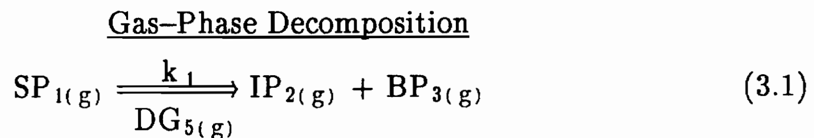

Gas–Phase Decomposition

$$SP_{1(g)} \xrightarrow[DG_{5(g)}]{k_1} IP_{2(g)} + BP_{3(g)} \tag{3.1}$$

Surface Reaction

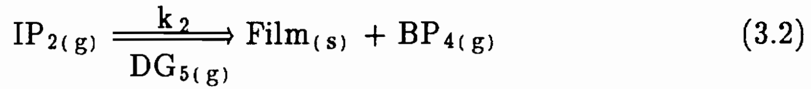

$$IP_{2(g)} \xrightarrow[DG_{5(g)}]{k_2} Film_{(s)} + BP_{4(g)} \quad (3.2)$$

The equation of continuity for the gas component i can be written [26]:

$$\nabla \cdot (N_i^{cv} + N_i^{du}) = \Sigma R_{ij} \quad (3.3)$$

where $N_i^{cv}$ and $N_i^{du}$ are the convection and diffusion flux of the component i, respectively, and $\nabla \cdot$ is the divergence operator. $R_{ij}$ is the reaction flux of the chemical reaction j associated with the gas species i. For the above system, the value of the index i ranged from 1 to 5, and the value of the index j ranged from 1 to 2.

For simplicity, variations of the species concentration along one direction, say, the Z–direction, was assumed to be much larger than those along the other two spatial directions, that is, the X and Y directions. The precursor $SP_{1(g)}$ is assumed to be highly diluted such that the Fick's law type relationship can be used to relate the diffusion flux and the concentration gradient of the species. The fluid flow within the porous medium is assumed to follow Darcy's law [14,17].

For the purposes of the discussion and presentation of the results, it is convenient to introduce the following parameters:

Equation 3.4

$Z^* = Z/L_0$ = Dimensionless spatial distance

$T^* = T/T_0$ = Dimensionless temperature

$D_i^* = D_i/D_0$ = Dimensionless diffusion constants of the species i, with

$D_i^{-1} = D_{ik}^{-1} + D_{i5}^{-1}$, where $D_{ik}$ is the Knudsen diffusion constant of the species i, and $D_{i5}$ is the binary diffusion constant of the pair $(i, DG_5)$

$P_i^* = P_i/P_0$ = Dimensionless pressure of the component i

$D_{a1} = BP_0/(\mu D_0)$ = Peclet number, with B being the permeability of the fibrous medium, and $\mu$ is the viscosity of the gas mixture

$D_{a2} = k_1 L_0^2/D_0$ = Gas–phase Damkohler number

$D_{a3} = k_2 L_0/D_0$ = Surface Damkohler number

$A/V$ = Surface area per unit volume

$L_0$ = Length of the medium in the Z–direction

$\Sigma(dP_i^*/dZ^*)$ = Dimensionless total pressure gradient

The governing equations of the one–dimensional (1–D) FCVI process can thus be expressed as [17,26,48]:

$$-\frac{d}{dZ}\left(\frac{D_1}{T}\frac{dP_1}{dZ}\right) - \frac{D_{a1}}{T}\left(\sum\frac{dP_i}{dZ}\right)\frac{dP_1}{dZ} + \frac{D_{a2}}{T}P_1 = 0 \quad (3.5a)$$

$$-\frac{d}{dZ}\left(\frac{D_2}{T}\frac{dP_2}{dZ}\right) - \frac{D_{a1}}{T}\left(\sum\frac{dP_i}{dZ}\right)\frac{dP_2}{dZ} - \frac{D_{a2}}{T}P_1 + \frac{D_{a3}}{T}(AL_0/V)P_2 = 0 \quad (3.5b)$$

$$-\frac{d}{dZ}\left(\frac{D_3}{T}\frac{dP_3}{dZ}\right) - \frac{D_{a1}}{T}\left(\sum\frac{dP_i}{dZ}\right)\frac{dP_3}{dZ} - \frac{D_{a2}}{T}P_1 = 0 \quad (3.5c)$$

$$-\frac{d}{dZ}\left(\frac{D_4}{T}\frac{dP_4}{dZ}\right) - \frac{D_{a1}}{T}\left(\sum\frac{dP_i}{dZ}\right)\frac{dP_4}{dZ} - \frac{D_{a3}}{T}(AL_0/V)P_2 = 0 \quad (3.5d)$$

$$-\frac{d}{dZ}\left(\frac{D_5}{T}\frac{dP_5}{dZ}\right) - \frac{D_{a1}}{T}\left(\sum\frac{dP_i}{dZ}\right)\frac{dP_5}{dZ} = 0 \quad (3.5e)$$

Note that the asterisk, *, has been dropped in equations (3.5a–3.5e) for simplicity.

The back pressure of the inert gas $DG_{5(g)}$, that is, the inert gas pressure at the position $Z^*=1$, is assumed to be one. The entrance pressure of the inert gas $DG_{5(g)}$, that is, the inert gas pressure at the position $Z^*=0$, is assigned based on

the forced–flow conditions.

The entrance pressure of the reagent species $SP_{1(g)}$ is assigned according to the dilution ratio. Values of the entrance pressure of the components $IP_{2(g)}$, $BP_{3(g)}$, and $BP_{4(g)}$ are assumed to be zero.

At the exit side ($Z^*=1$), the adiabatic condition ($dP^*/dZ^*=0$) is used for all the gas components except for the inert gas component.

In the governing equations above, the total pressure gradient, $\Sigma(dP_i/dZ)$, may come from both the pressure changes due to the chemical reactions and the external pressure gradient (forced–flow). It is obvious from equations (3.5a–3.5e) that the deposition rate profiles depend mainly on three controlling parameters, that is, $D_{a1}$ (Peclet number), $D_{a2}$ (Gas–phase Damkohler number), and $D_{a3}$ (Surface Damkohler number).

In the following study, the dimensionless parameters $D_{i5}^*$ ($=D_{i5}/D_0$), $D_{ik}^*$ ($=D_{ik}/D_0$), and $T^*$ are assumed to be unity. The parameter ($AL_0/V$) is characteristic of the geometry of the composite preform and is fixed for a given geometry. The FCVI model described by equations (3.5a–3.5e) above will be called as simple flux model thereafter as compared to the multi–component dusty gas model, which will be introduced shortly.

The governing equations (3.5a–3.5e) are nonlinear due to the total pressure gradient term. The finite element method (FEM) [43] was used to numerically solve the equations (3.5a–3.5e) with the associated boundary conditions. The numerical solutions were assumed to be convergent if the following criterion of convergence is satisfied for each of the gas species:

$$\frac{\sum_{i=1}^{m} \{(\text{Solution}_i)_k - (\text{Solution}_i)_{k-1}\}^2}{\sum_{i=1}^{m} \{(\text{Solution}_i)_k\}^2} \leq 0.01 \tag{3.6}$$

In equation (3.6), $(\text{Solution}_i)_k$ represents the solution at node i in the k–th iteration step for a particular gas species, and m is equal to the total number of nodes.

With the assumption that the precursor is highly diluted, the Fick's type flux relationship was used in the simple flux model above to decouple the diffusion flux of one species from the other. Interactions among fluxes of the gas species were neglected. As a result, the simple flux model may not give good approximations to the FCVI process depending on the diluted condition of the FCVI process.

Recently, the multi–component dusty gas model, originally proposed by Maxwell in 1860 [25], was used by Sotirchos [17] to study the FCVI process. With the use of the dusty gas model, for example, the relationship between the pressure gradient of the reagent species $SP_{1(g)}$ and the diffusion fluxes of all the species can be written as:

$$-\frac{1}{RT}\frac{dP_1}{dZ} = (\alpha_2/D_{12}+\alpha_3/D_{13}+\alpha_4/D_{14}+\alpha_5/D_{15}+1/D_{1k})N_1 - (\alpha_1 N_2/D_{12}+\alpha_1 N_3/D_{13}+\alpha_1 N_4/D_{14}+\alpha_1 N_5/D_{15}) \tag{3.7}$$

where:

$\alpha_i$=Molar fraction of the species i

$D_{ij}$=Binary diffusion constant of the pair (i,j)

$D_{ik}$ = Knudsen diffusion constant of the species i

$R$=Gas law constant

$T$=Temperature

$N_i$=Diffusion flux of the species i

As the reagent precursor $SP_{1(g)}$ becomes more highly diluted, the molar fraction of the dilute gas $\alpha_5$ approaches unity while the molar fractions of all other species approach zero. Eventually, the equation (3.7) can be reduced to the familiar Fick's type flux relationship,

$$-\frac{1}{RT}\frac{dP_1}{dZ} = (1/D_{15}+1/D_{1k})N_1 \tag{3.8}$$

From the expressions above, it is obvious that the simple flux model is a limiting case of the multi–component dusty gas model.

In the subsequent calculations, the dilution ratio, that is, $P_1/P_5$ at the position $Z^*=0$, was assumed to be 0.01. It was found that the results obtained from both the simple flux model and the dusty gas model were almost identical when using this dilution ratio. Therefore, further studies were conducted using the simple flux model.

## 3.4 Results and Discussion

In the following text, the parameter $\Delta P$ is defined as the inert gas pressure difference between the entrance and the exit sides of the medium. The thickness ratio $\alpha$ is defined for a given deposition rate profile as the ratio between the deposition rate at the exit side and the maximum deposition rate. The optimum

profile is defined as the deposition rate profile with a constant deposition rate being equal to the maximum deposition rate of the deposition rate profile. Deposition rate profiles with higher thickness ratio $\alpha$ can result in composites with lower residual porosity. The thickness ratio $\alpha$ of the optimum profile is always unity.

Figure 3.1 shows a typical example of the deposition rate profile of the FCVI process. Values of the parameters used are: $D_{a1}$=1.0, $D_{a2}$=20.0, $D_{a3}$=0.02, $AL_0/V$=100.0.

As shown in Figure 3.1, both the thickness ratio $\alpha$ and the total deposition rates increase with increasing flow velocity. The corresponding thickness ratios $\alpha$ with $\Delta P$ being equal to (0.1, 0.5, 1.0, 1.5) are (0.63, 0.70, 0.77, 0.81) respectively. With further increase in the pressure difference $\Delta P$, the deposition rate profile is expected to approach the optimum profile.

For the FCVI process illustrated in Figure 3.1, because the deposition rate profiles are descending and the deposition rates increase with the increase in the flow velocity, it can be concluded that this kind of FCVI process is controlled by the surface reaction rate [24]. For the FCVI processes that are controlled by the surface reaction, a higher pressure difference $\Delta P$ should result in ceramic matrix composites with lower residual porosity.

Although the use of the forced–flow can improve the surface reaction controlled FCVI process, the efficiency of this technique depends heavily on the permeability of the fibrous preform. This can be illustrated by comparing the deposition rate profiles of Figure 3.1 with those of Figure 3.2. For Figure 3.2, the parameters used are the same as those of Figure 3.1 with only the Peclet number being reduced from 1.0 to 0.2.

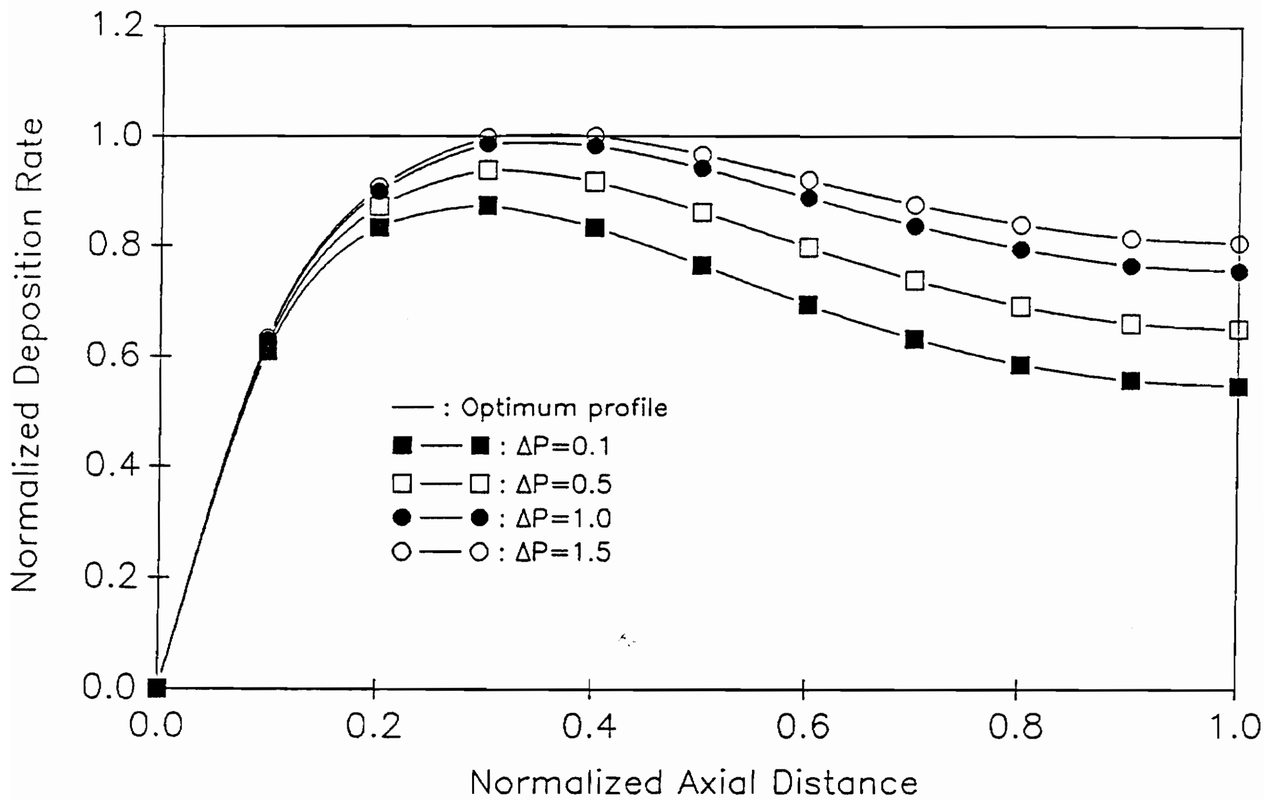


Figure 3.1 Deposition Rate Profiles of Surface Reaction Controlled FCVI Processes with $\Delta P$ being Equal to 0.1, 0.5, 1.0 and 1.5

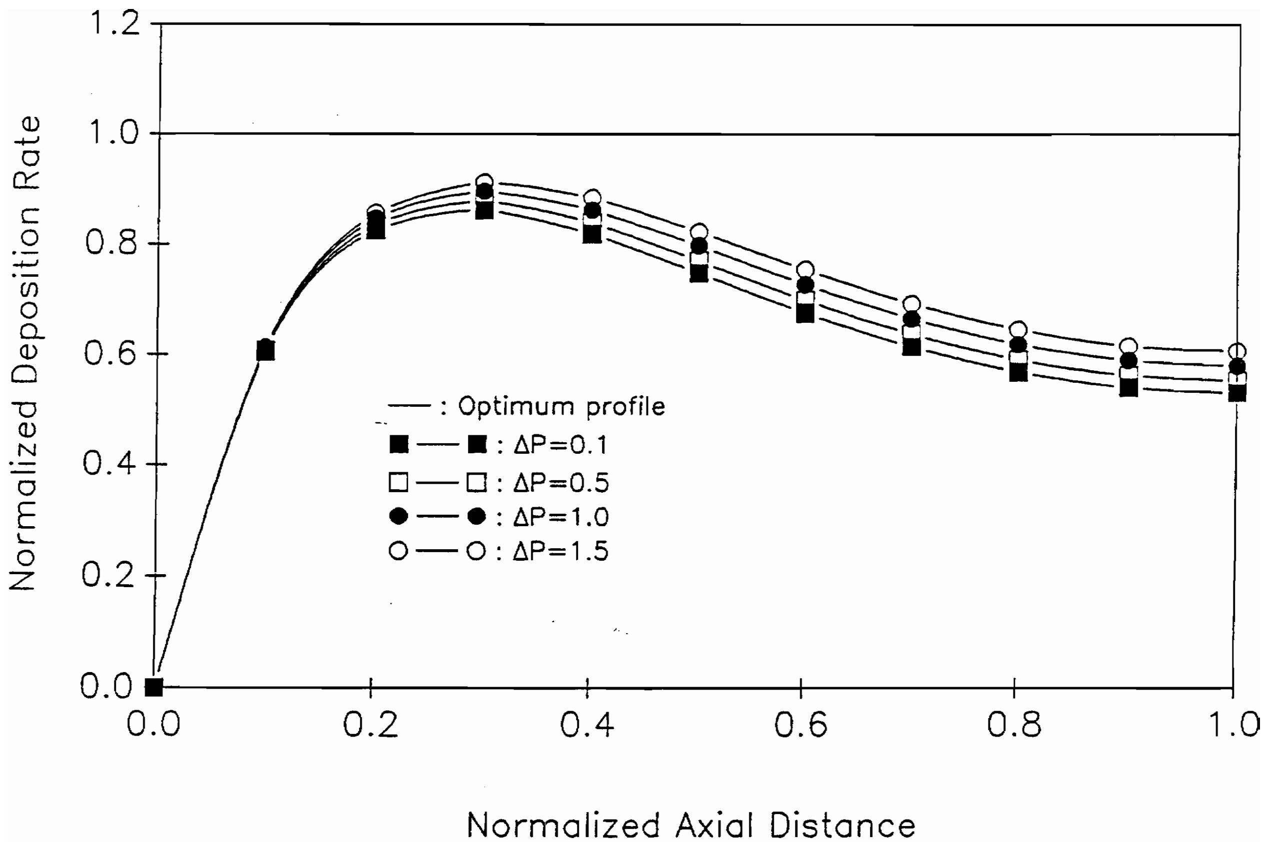


Figure 3.2 Efficiency of the Forced–Flow Technique on Improving the Deposition Rate Profiles of Surface Reaction Controlled FCVI Processes. The Peclet number was changed from 1.0 in Figure 3.1 to 0.2 to simulate changes of the medium permeability

As shown in Figure 3.2, all the corresponding deposition rates are reduced because of the decrease in forced–flow with the decrease in permeability. The corresponding thickness ratios $\alpha$ with $\Delta P$ being equal to (0.1, 0.5, 1.0, 1.5) are (0.62, 0.63, 0.65, 0.67). With further decrease in the permeability of the medium, improvements in the thickness ratios $\alpha$ with the use of forced–flow are expected to disappear.

From the definition of the Peclet number, it can be said that large Peclet numbers imply composites with higher porosity, or the composites at the initial stage of the FCVI process. On the other hand, small Peclet numbers represent composites with lower porosity, or the composites at the final stage of the FCVI process.

Therefore, for the application of the forced–flow process, the control of the magnitude and duration of the forced–flow is crucial. The efficiency of the forced–flow process is higher at the initial stage than at the later stage of the process.

Another example of the FCVI process is shown in Figure 3.3. Parameters used in this case are: $D_{a1}=3.0$, $D_{a2}=0.1$, $D_{a3}=0.1$, $AL_0/V=1.0$.

As shown in Figure 3.3, the thickness ratio $\alpha$ is independent of the pressure difference $\Delta P$ since the maximum deposition rate for each deposition rate profile is always at the exit side. In contrast to the deposition rate profiles shown in Figure 3.1 and Figure 3.2, the deposition rates in this case decreased with increasing flow velocity. The ratios between the maximum deposition rates with $\Delta P$ equal to (0.1, 0.2, 0.3, 0.5) and the maximum deposition rate with $\Delta P$ being equal to 0.01 are (0.88, 0.77, 0.68, 0.62) respectively.

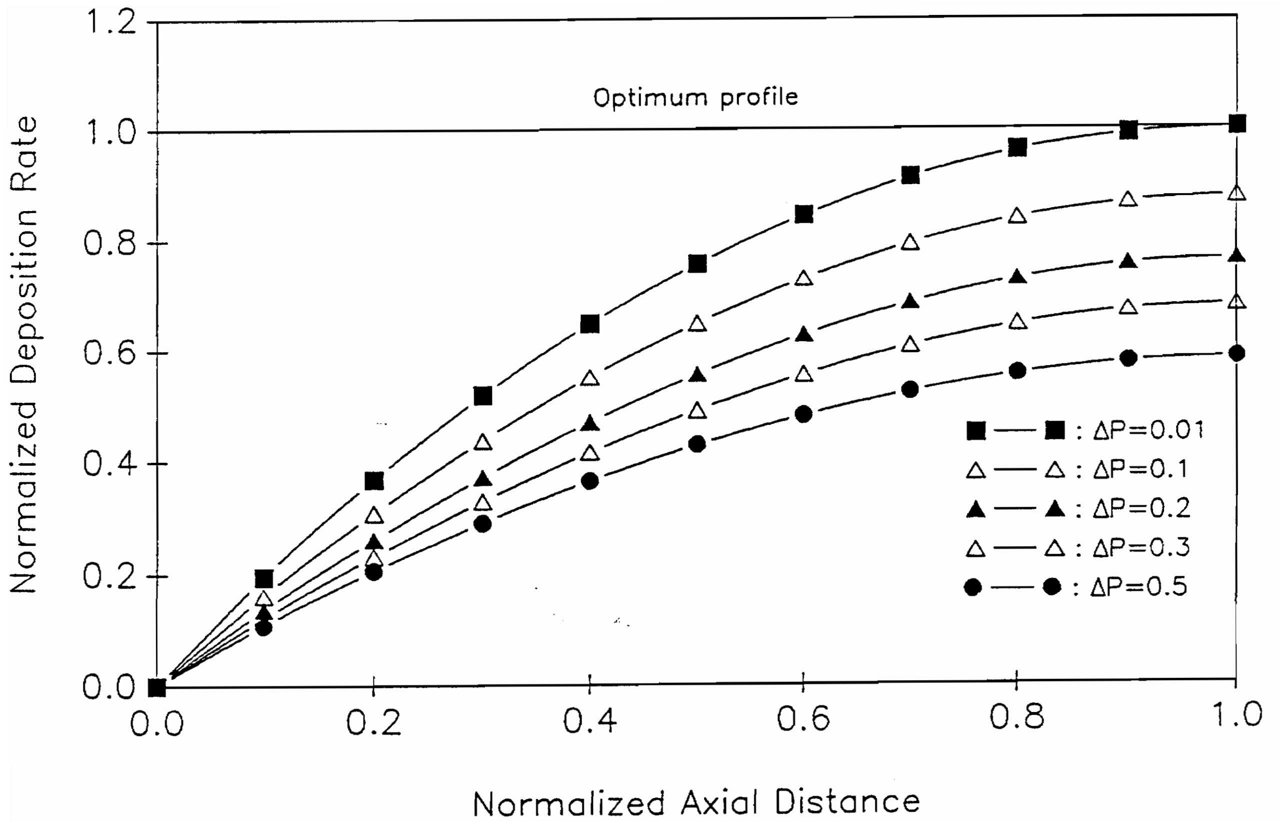


Figure 3.3 Deposition Rate Profiles of Gas–Phase Reaction Controlled FCVI Processes with $\Delta P$ being equal to 0.01, 0.1, 0.2, 0.3 and 0.5

The decrease in the deposition rate with increased flow velocity can be attributed to the decrease in residence time of the gas mixture, which in turn decreases the percentage of completion of the gas–phase decomposition process, as described in the equation (3.1).

For the FCVI process shown in Figure 3.1, the ascending deposition rate profiles and the decrease in deposition rates with an increase in flow velocity lead us to the conclusion that this kind of FCVI process is controlled by the gas–phase reaction [24]. For the FCVI processes controlled by the gas–phase reactions, the use of forced–flow technique is unnecessary.

In addition to using the forced–flow technique, the deposition rate profiles could be improved by reducing the deposition temperature. The deposition rate profiles in Figure 3.1 are changed by reducing the surface Damkohler number $D_{a3}$ from 0.02 to 0.004, 0.002 and 0.0004. The value of $\Delta P$ is assumed to be 0.1. The gas–phase Damkohler Number $D_{a2}$ is assumed to be constant which implies that the activation energy of the gas–phase decomposition process is small in this case.

As shown in Figure 3.4, the thickness ratio $\alpha$ can be improved by decreasing the surface Damkohler number. Values of the thickness ratio $\alpha$ for $D_{a3}$ values of (0.02, 0.004, 0.002, 0.0004) are (0.63, 0.96, 0.99, 1.00). Although improved thickness ratios are obtained by decreasing the temperature, the deposition rates also decrease resulting in longer processing times.

For the surface reaction controlled FCVI process, the forced–flow technique can be used together with the temperature decrease scheme to alleviate the long processing time problem. For example, for the above FCVI process with $D_{a3}$=0.004, the deposition rate can be increased up to 1.15 times by changing $\Delta P$ from 0.1 to 1.5.

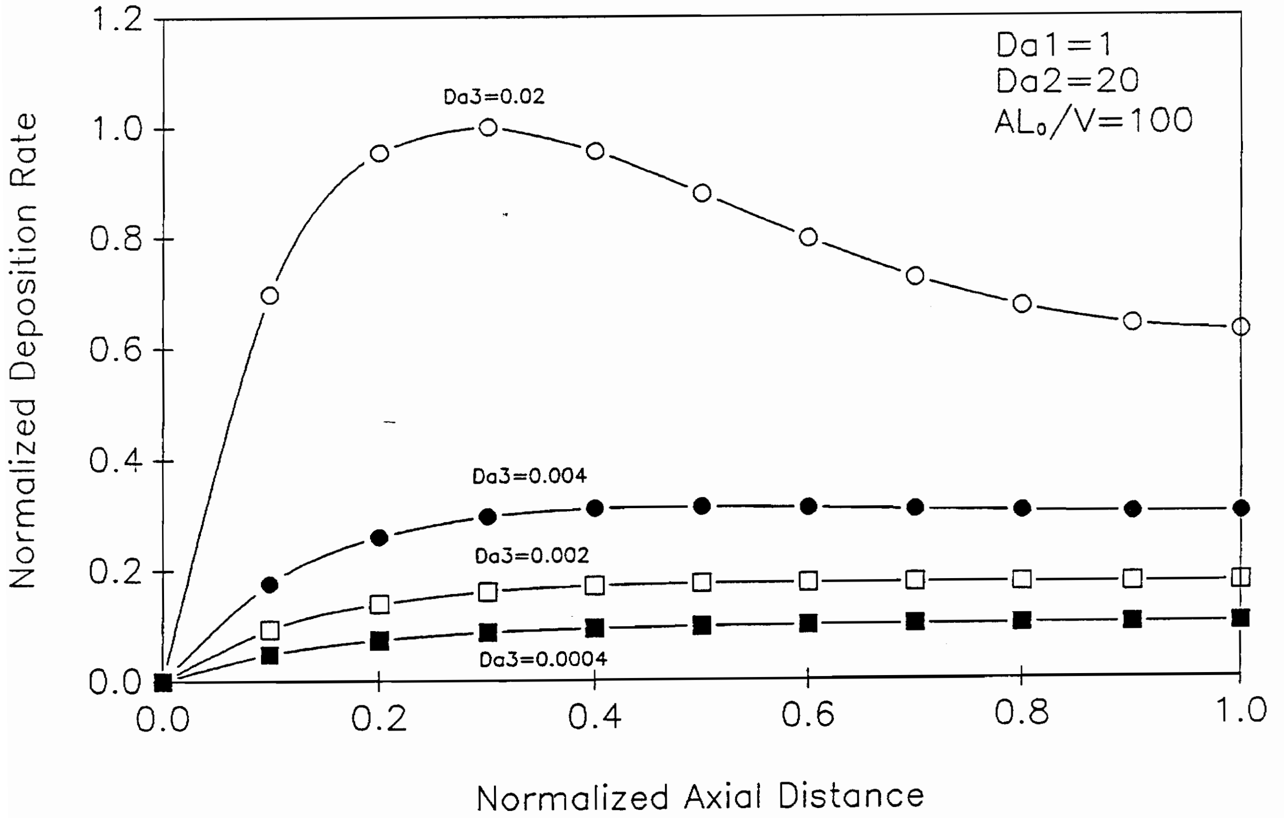


Figure 3.4 Changes of Deposition Rate Profiles of Figure 3.1 with the Surface Damkohler Number being Changed from 0.02 to 0.0004, 0.002 and 0.004

Similarly, the deposition rate profiles in Figure 3.3 are changed by reducing the gas–phase Damkohler number $D_{a2}$ from 0.1 to 0.05, 0.02 and 0.01. The value of $\Delta P$ is also assumed to be 0.1. The surface Damkohler number $D_{a3}$ is assumed to be constant in this case which implies that the activation energy of the surface reaction is very small.

As shown in Figure 3.5, although the shape uniformity of the deposition rate profiles can be improved by decreasing the deposition temperature, this temperature reduction seems to be unnecessary since the thickness ratio $\alpha$ remains the same for all the $D_{a2}$ values. As a result, improvements of the residual porosity resulting from the temperature reduction is limited for the gas–phase controlled FCVI process. However, the processing time is expected to be much longer with the decrease in deposition rates.

From the above studies, it can be concluded that strategies to optimize the FCVI process are fundamentally different for processes with different controlling steps. The use of forced–flow can improve the deposition rate profiles for the surface reaction controlled FCVI process. On the other hand, it may prove detrimental for the gas–phase controlled FCVI process.

Similarly, although reducing the deposition temperature improves the deposition rate profiles of the FCVI processes that are controlled by the surface reactions, the application of this technique to improve the deposition rate profiles of the gas–phase controlling FCVI process is unnecessary.

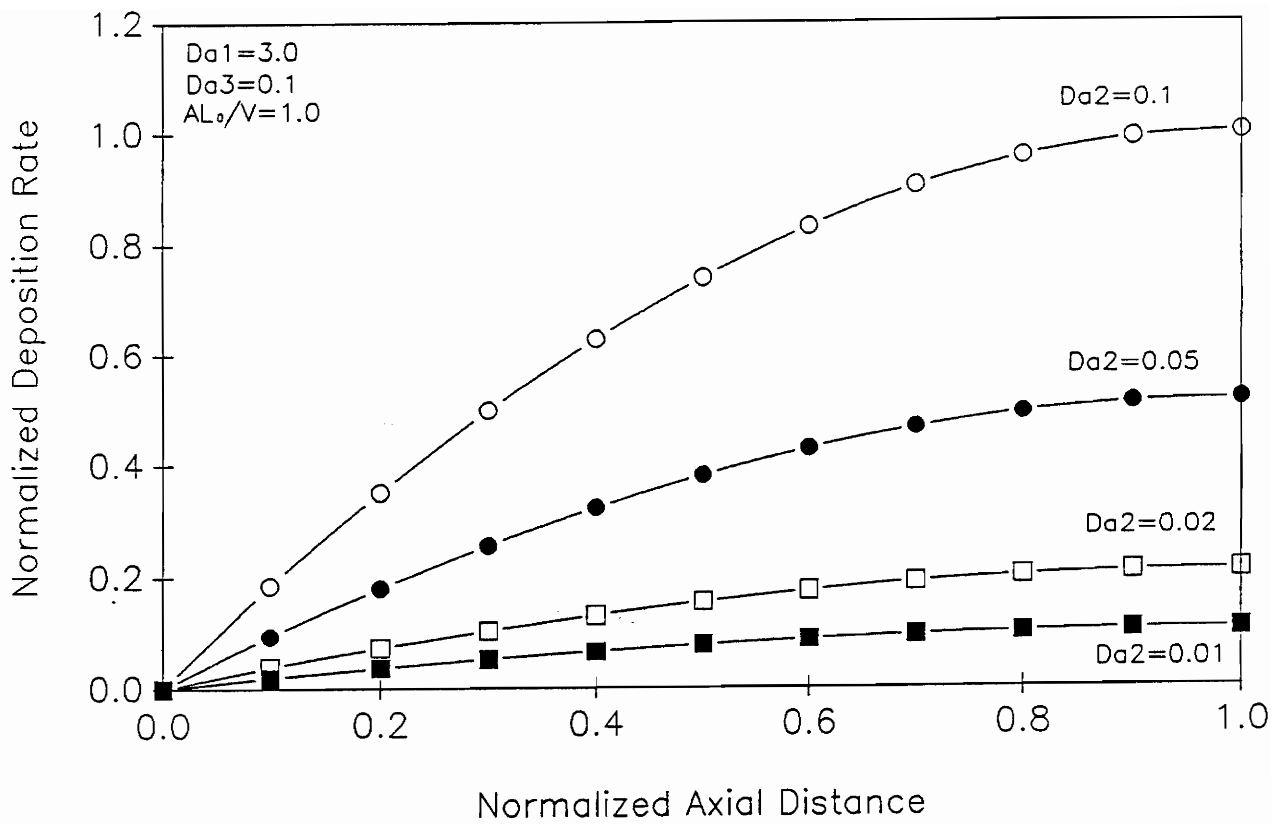


Figure 3.5 Changes of Deposition Rate Profiles of Figure 3.3 with the Gas–Phase Damkohler Number being Changed from 0.1 to 0.01, 0.02 and 0.05

### 3.5 Summary

The use of the forced–flow technique to improve the deposition rate profile in the forced–flow CVI process was studied with the simple flux model which incorporates both the gas–phase and surface reactions, and the pressure changes due to the applied pressure gradient as well as the chemical reactions.

For the surface reaction controlled FCVI processes, the use of forced–flow can improve the deposition rate profiles, and results in lower residual porosity, as expected. The efficiency of the forced–flow technique is a function of the permeability of the porous medium. The forced–flow technique is more effective in the early stages of the process when the permeability of the porous medium is still relatively high.

On the other hand, for the FCVI processes that are controlled by the gas–phase reactions, improvements in the deposition rate profiles by using the forced–flow are limited. Unlike the trends in the surface reaction controlled FCVI processes, the deposition rates in the gas–phase reaction controlled FCVI processes decreased with an increased forced–flow due to the decrease in the completion of the gas–phase decomposition process. Under this circumstance, uses of the forced–flow are not suggested.

For the thermal gradient FCVI processes, the controlling step of the processes may change with respect to different thermal gradient patterns. Even for the FCVI processes with a fixed thermal gradient, the thermal profile of the medium may change due to changes of the permeability and thermal conductivity of the composite medium during the deposition process.

Therefore, for the modeling of the FCVI process, including the thermal gradient FCVI process, it is very important to consider explicitly the individual reactions, that is, the gas–phase and surface reactions, in order to study the optimum processing conditions, such as the temperature profile and the pressure gradient.

This paper titled

"Kinetic Study of Silicon Carbide Deposited from Methyltrichlorosilane Precursor"

was submitted to
Journal of Materials Research

# Chapter 4 Kinetic Study of Silicon Carbide Deposited from Methyltrichlorosilane Precursor

## 4.1 Abstract

The kinetics of silicon carbide (SiC) deposition, in a hot–wall chemical vapor deposition (CVD) reactor, were modeled by analyzing our own deposition rate data as well as reported results. In contrast to the previous attempts which used only the first order lumped reaction scheme, the present model incorporates both homogeneous gas phase and heterogeneous surface reactions.

The SiC deposition process was modeled using the following reactions — (1) : gas phase decomposition of methyltrichlorosilane (MTS) molecules into two major intermediates one containing silicon and the other containing carbon; (2) : adsorption of the intermediates onto the surface sites of the growing film; (3) : reaction of the adsorbed intermediates to form silicon carbide.

The equilibrium constant for the gas phase decomposition process was divided into the forward and backward reaction constants as 2.0E+25 exp[(–448.2 kJ/mol)/RT] and 1.1E+32 exp[(–416.2 kJ/mol)/RT], respectively. Equilibrium constants for the surface adsorption reactions of silicon–carrying and carbon–carrying intermediates are 0.5E+11 exp[(–21.6 kJ/mol)/RT] and 7.1E+09 exp[(–33.1 kJ/mol)/RT], while the rate constant for the surface reaction of the intermediates is 4.6E+05 exp[(–265.1 kJ/mol)/RT].

## 4.2 Introduction

In addition to being a high temperature semiconductor, SiC possesses excellent mechanical properties. Due to these interesting properties, SiC is an excellent candidate for both structural and electronic applications at high temperatures [49]. Chemical vapor deposition is one of the best techniques to deposit dense SiC in high purity. Due to the absence of impurities in the grain boundaries, SiC prepared by the CVD process has significantly better properties. As a result, the CVD SiC material has been widely used in applications such as protective coatings for corrosive or abrasive environments, and as a material for semiconductor devices in aggressive environments.

Most of the SiC CVD processes involve either the Si–C–H system: such as $SiH_4/C_3H_8$ [50] and $Si_2H_6/C_2H_2$ precursors [51]; or Si–C–H–Cl system: such as $CH_3SiCl_3/H_2$ [52–60], $SiCl_4/CH_4$ [61–63] and $SiHCl_3/C_3H_8$ [64] precursors. Among the chemical systems mentioned above, the $CH_3SiCl_3$ (MTS)/$H_2$ system is often chosen for both economical and practical reasons [65].

Since most of the physical or chemical properties of SiC are strongly dependent on the processing conditions, a knowledge of the deposition mechanisms, including the transport phenomena and kinetic data of the chemical reactions, is highly desirable.

For example, one of the design goals of the hot–wall CVD reactor is to attain uniform deposition rate profiles over the length of the reactor. On the other hand, for the chemical vapor infiltration (CVI) process, the purpose of applications of both forced–flow and temperature gradient techniques is to obtain an ascending deposition rate profile so that the premature pore blockage problem could be

avoided. As pointed out by Desu et al. [24] for the hot–wall CVD process and Tsai et al. [66] for the forced–flow CVI process, in order to simulate the deposition rate profiles through modeling calculations, both gas phase and surface reactions of the deposition process should be explicitly considered in the analytical model.

For the SiC CVD process using the MTS/$H_2$ precursors, it is generally agreed, based on thermodynamic studies, that the MTS molecules are decomposed into gaseous intermediates containing either carbon or silicon at first [56,67]. The silicon and carbon are then independently provided to the substrate to form the SiC films. Depending on the experimental conditions, the SiC CVD process may not have a first order dependence in MTS concentration as assumed usually.

Although the importance of including gas phase reactions in the modeling calculations was documented [7,23–24,66], most studies (as summarized by Besmann et al. [56] and Schlichting [65]) concerning the kinetic data of the SiC deposited from the MTS/$H_2$ precursors simply neglected the gas phase reactions and used a lumped first order reaction to obtain the effective activation energy of the deposition process. Using this simplified model, widely different effective activation energies were reported for the SiC deposition from MTS/$H_2$ by different authors [56], which indicates the ineffectiveness of this simple model for different processing conditions.

In this work, a deposition mechanism, including both gas phase and surface reactions, was proposed for the SiC CVD process using the MTS/$H_2$ precursors. Kinetic data were obtained by analyzing our own as well as reported deposition rate data by a finite element (FEM) model, which incorporates both the proposed deposition mechanism and the transport phenomena of the gas species.

Changes of the effective activation energy and reaction order of the deposition process with respect to changes of the experimental conditions were in agreement with the FEM predictions. These changes were due to the consumption of gas species on the hot reactor walls.

## 4.3 Experimental Procedure

A schematic diagram of the hot–wall CVD reactor used in this study is shown in Figure 4.1. The CVD reactor used was a quartz tube with inner and outer diameters of 5.08 cm and 5.43 cm, respectively. The total length of the reactor was 50.8 cm, with the heating zone length of 30.48 cm. A uniform temperature ($\pm$ 5° C) zone of 6 cm long was located around the center of the reactor. Thermal profiles of this SiC CVD experiment are shown in Figure 4.2.

Single crystal Si (100) substrates were used in this study. Before the deposition of SiC thin films with the MTS/$H_2$ precursors, a thin SiC buffer layer was grown by reaction of acetylene ($C_2H_2$) and the Si (100) substrates. Details of the procedure to convert the Si (100) to the SiC buffer layer by $C_2H_2$ in a hot–wall CVD reactor can be found in reference [68].

For each run of the SiC deposition, substrates were placed around the center of the hot–wall CVD reactor after the experimental parameters stabilized at the set values. The run time of each experiment was about 3 to 5 hours depending on the deposition temperature and the MTS concentration. Weight increases of the substrate located at the reactor center were measured to calculate the deposition rate of the SiC CVD process.

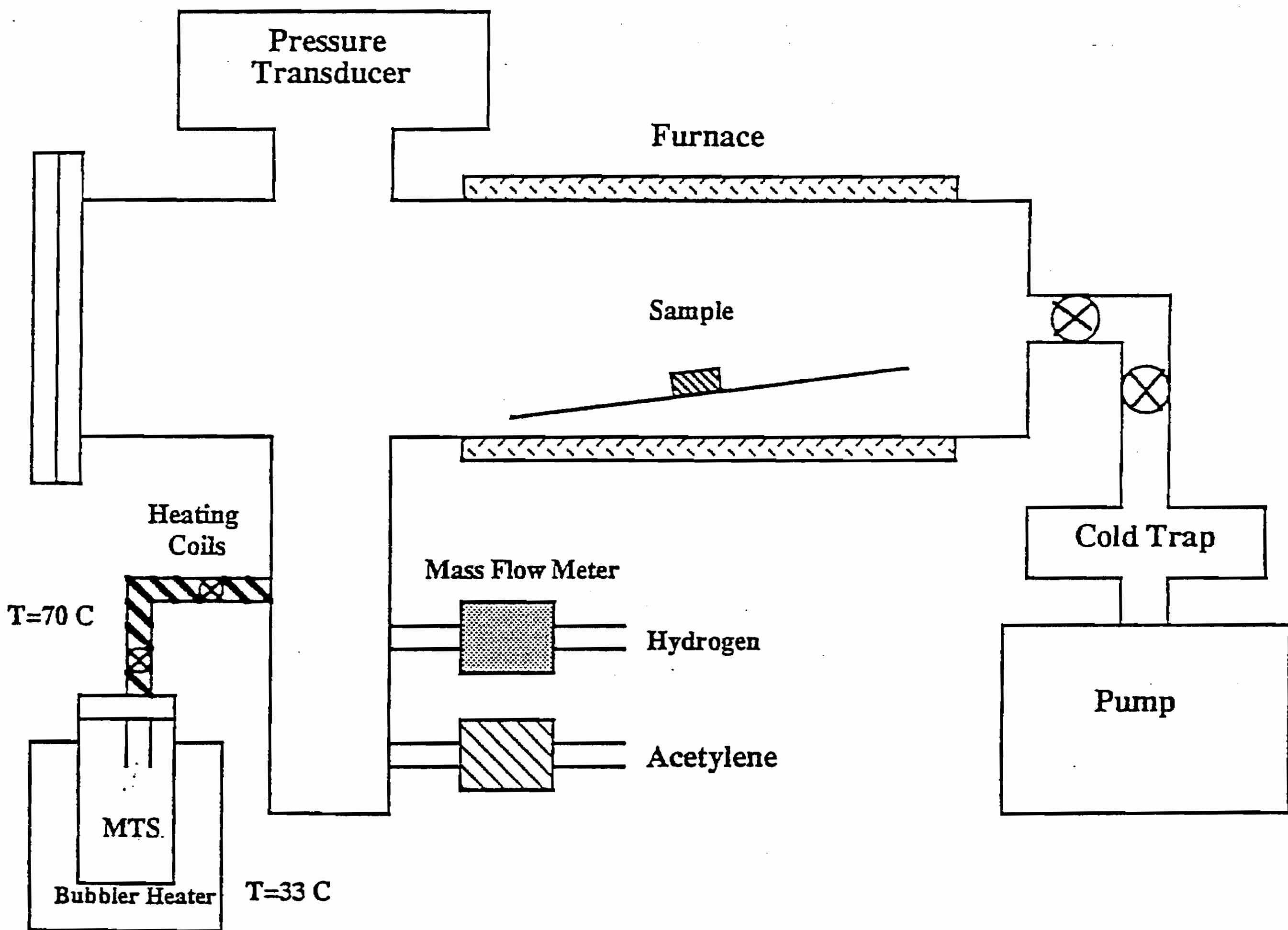


Figure 4.1 A Schematic Diagram of the Hot–Wall CVD Reactor

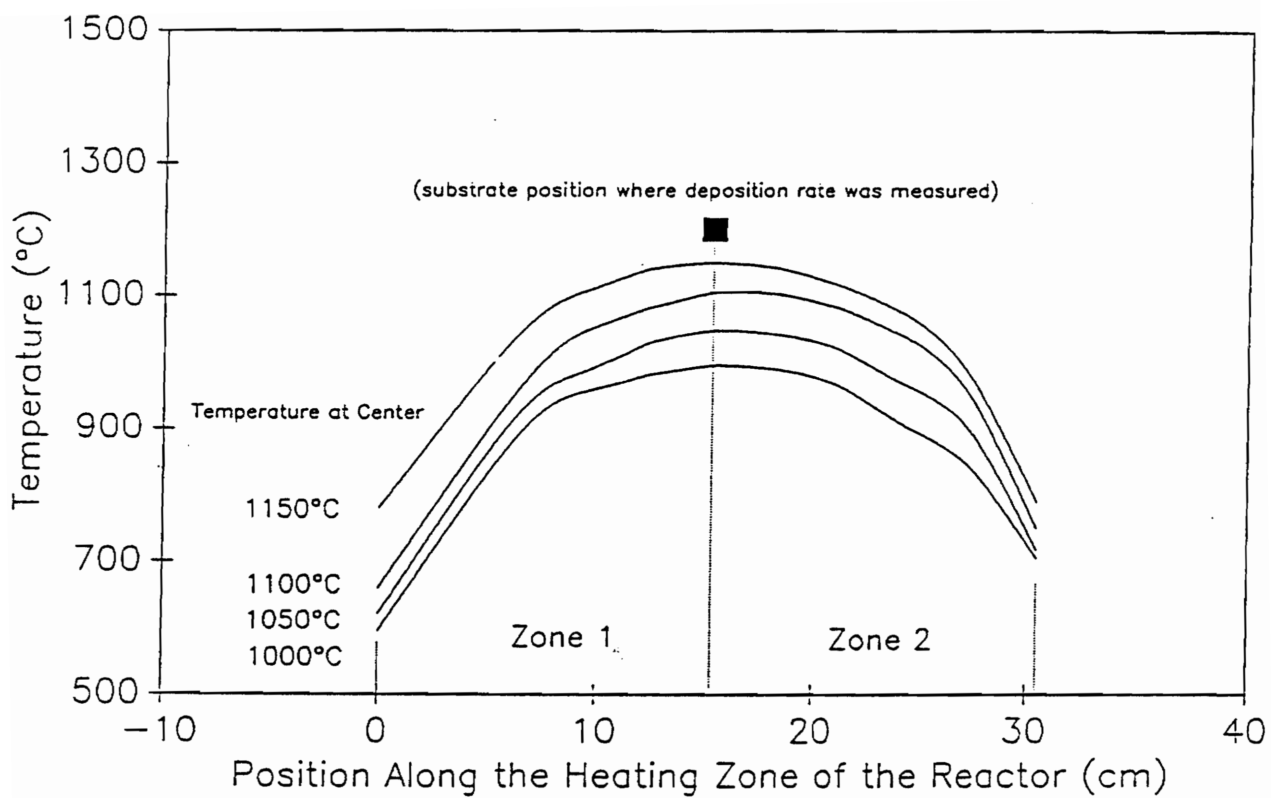


Figure 4.2 Thermal Profiles of the Hot–Wall CVD Reactor

Deposition temperatures were varied from 1000°C to 1150°C in intervals of 50°C. The total inlet gas pressures used were 1.8 Torr, 5.0 Torr, and 8.0 Torr. The flow rate of $H_2$ was about 300 sccm. The ratio of $H_2$ and MTS concentrations was adjusted to be around 50.

## 4.4 Modeling Calculations

In this section, the kinetic model of SiC deposited from MTS/$H_2$ precursor is introduced first. Then, a CVD FEM model, which incorporated both the kinetic model and the transport phenomena of the gas species, was formulated to calculate the SiC deposition rate along the hot–wall CVD reactor.

### 4.4.1 Deposition Mechanism

It is known that the MTS precursor is first decomposed into a gaseous mixture of chlorosilanes and hydrocarbons species, and then these gas species react together to form silicon carbide [56,67,69].

Therefore, the following reaction sequence was proposed for the deposition of SiC from MTS: MTS molecules in the gas phase were first assumed to be decomposed into two major intermediates one containing silicon and the other containing carbon (reaction 4.1); the intermediates were then adsorbed onto the surface sites of the growing films (reactions 4.2a and 4.2b) and later react to form silicon carbide (reaction 4.3a).

The steps involved in the deposition of SiC from MTS/$H_2$ precursor are as follows:

(1). Gas phase decomposition of the MTS molecules

This reaction produces two intermediate species, one bearing silicon ($IP_{si}$) and the other bearing carbon ($IP_c$), and a gaseous by-product $BP_1$.

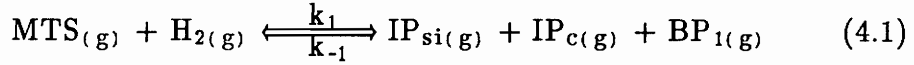

$$MTS_{(g)} + H_{2(g)} \underset{k_{-1}}{\overset{k_1}{\rightleftharpoons}} IP_{si(g)} + IP_{c(g)} + BP_{1(g)} \qquad (4.1)$$

$k_1$ ($cm^3/mol$–sec) and $k_{-1}$ ($cm^6/mol^2$–sec) represent the rate constants of the forward and backward reactions, respectively. Note that the equilibrium constant $K_g$ ($mol/cm^3$) of the gas phase decomposition process is equal to $k_1/k_{-1}$.

(2). Adsorption of the intermediate species

Equilibrium constants of the adsorption processes associated with the species $IP_{si}$ and $IP_c$ are $K_{a1}$ and $K_{a2}$ ($cm^3/mol$), respectively.

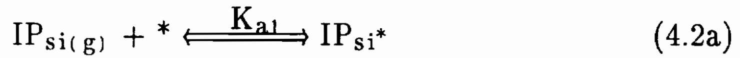

$$IP_{si(g)} + * \overset{K_{a1}}{\rightleftharpoons} IP_{si}* \qquad (4.2a)$$

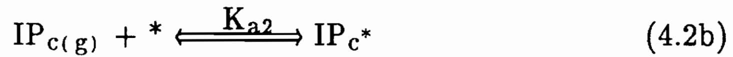

$$IP_{c(g)} + * \overset{K_{a2}}{\rightleftharpoons} IP_c* \qquad (4.2b)$$

where the asterisk, *, represents the vacant surface sites and $IP_{si}*$ and $IP_c*$ represent the adsorbed species.

(3). Reaction of the adsorbed intermediates

This step results in $Si_{(s)}$, $C_{(s)}$, $SiC_{(s)}$, and other gaseous by-products.

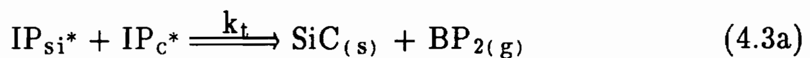

$$IP_{si}* + IP_c* \xrightarrow{k_t} SiC_{(s)} + BP_{2(g)} \qquad (4.3a)$$

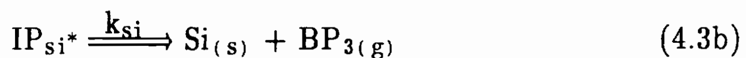

$$IP_{si}* \xrightarrow{k_{si}} Si_{(s)} + BP_{3(g)} \qquad (4.3b)$$

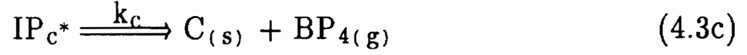

$$IP_{c^*} \xrightarrow{k_c} C_{(s)} + BP_{4(g)} \qquad (4.3c)$$

Since the SiC films of the CVD experiments used to derive the kinetic data in this study are stoichiometric, the surface reactions (4.3b,4.3c) were neglected in the following calculations. In other words, the derived kinetic data are based on the stoichiometric film condition.

According to the Langmuir isothermal expression, the deposition rate of the silicon carbide, based on the above proposed kinetic model, can be expressed as [70],

$$\text{Deposition Rate of SiC (mol/cm}^2\text{–sec)} = k_t[IP_{si}^*][IP_c^*]$$
$$= k_t K_{a1} K_{a2}[IP_{si}][IP_c]/(1+K_{a1}[IP_{si}]+K_{a2}[IP_c])^2 \qquad (4.4)$$

4.4.2 Modeling of the Hot–Wall CVD Process

The equation of continuity for gas species i of the SiC CVD process can be expressed as [26]:

$$\nabla \cdot (\vec{N}_i^{du} + \vec{N}_i^{cv}) = \Sigma R_{ij} \qquad (4.5)$$

with:

- $\vec{N}_i^{du}$ (mol/cm$^2$–sec) = Diffusion flux of gaseous species i
- $\vec{N}_i^{cv}$ (mol/cm$^2$–sec) = $\vec{V} p_i/RT$ = Convection flux of gaseous species i, where $\vec{V}$ is the flow velocity; $p_i$ is the pressure of the gaseous species i; R is the gas law constant; T is the deposition temperature

- $R_{ij}$ (mol/cm$^3$–sec) = Reaction flux of gaseous species i associated with the chemical reaction j

In this SiC CVD model, values of index i ranged from 1 to 5, that is, values of the pressure of MTS, $H_2$, $IP_{Si}$, $IP_C$ and $BP_1$ were evaluated at each position. Both gas phase reaction and surface reaction were considered in this kinetic model.

The binary diffusion constant of the gas species was assumed to be proportional to $T^{1.5}$(°K)$P$(atm)$^{-1}$ [26]. Values of the binary diffusion constant used in the modeling calculations with 1273°K deposition temperature and 0.1 atm total pressure are given in Table 4.1 [26,71].

Table 4.1 Bulk Diffusion Constants of five Gaseous Components Used in the SiC CVD Modeling Calculations

| <Binary Diffusion Constants><br>$D_{ab}$ (cm$^2$/sec) at T=1273°K, P=0.1atm (b = $H_2$) | |
|---|---|
| MTS | 48.1 [71] (estimated from that of $SiHCl_{3(g)}$) |
| $H_2$ | 210.0 [71] |
| $IP_{Si}$ | 55.8 [71] (estimated from that of $SiCl_{2(g)}$) |
| $IP_C$ | 81.7 [26] (estimated from that of $CH_{4(g)}$) |
| $BP_1$ | 84.8 [71] (estimated from that of $HCl_{(g)}$) |

The Knudsen diffusion constants were estimated from the following equation [27]:

$$D_{ki}\,(cm^2/sec) = 9700\ r(cm)\ [T(^\circ K)/M_i(g/mol)]^{0.5} \qquad (4.6)$$

where r is the radius of the CVD reactor and $M_i$ is the molecular weight of the gas component i.

The effective diffusion constant is approximated as [25]:

$$1/D_{eff} = 1/D_{binary} + 1/D_{knudsen} \qquad (4.7)$$

Estimations of the flow velocity $\vec{V}$, which is equal to $V_0$ in this one–dimensional flow problem, was based on the well–known Hagen–Poiseuille equation for laminar flow in straight pipes of circular cross section [72]:

$$V_0\,(cm/sec) = \frac{r^2}{8\mu}\,\frac{\Delta \Sigma p_i}{\Delta x} \qquad (4.8)$$

where $\frac{\Delta \Sigma p_i}{\Delta x}$ is the total pressure gradient, and $\mu$ is the viscosity of the gas mixture.

Experimental observations indicate that the Hagen–Poiseuille equation is valid for pipe flows with Reynolds number less than 2000. Values of the calculated Reynolds number are well below the criterion in this work. The flow velocity profile with 1373°K deposition temperature and 1.8 Torr total pressure is shown in Figure 4.3. The flow velocity is decreased at the exit due to the use of the adiabatic

boundary conditions. With the low pressure system used, the mass transfer is primarily attributed to the diffusion mechanism.

Equation (4.5) is nonlinear because of the chemical reaction and convection flow terms. The finite element method [43,73] was used to solve the SiC CVD model numerically. Fortran programming codes "FEM1D", included in the appendix of reference [43], were modified to analyze the CVD FEM model. The following criterion was used to ensure that solutions of each of the gas species have converged:

$$\frac{\sum_{i=1}^{m} \{(Solution_i)_k - (Solution_i)_{k-1}\}^2}{\sum_{i=1}^{m} \{(Solution_i)_k\}^2} \leq 0.02 \qquad (4.9)$$

where $(Solution_i)_k$ represents the solution at node i in the k–th iteration step of a particular gas species, and m is equal to total number of nodes.

An under–relaxation coefficient $\omega$ [74], ranging from 0.1 to 0.5, was chosen to help the CVD FEM model in reaching the convergence.

Forty linear elements were used in all the simulation cases. The calculated deposition rate at node 21, positioned at the reactor center, was used to compare with our own experimental results.

Thermal profiles of the hot–wall CVD reactor, as shown in Figure 4.2, were also considered in the modeling calculations. The gas mixture viscosity has a square root dependence on the deposition temperature [26]. The calculated SiC deposition rate at node 21, at 1.8 Torr total pressure and various deposition temperatures, was

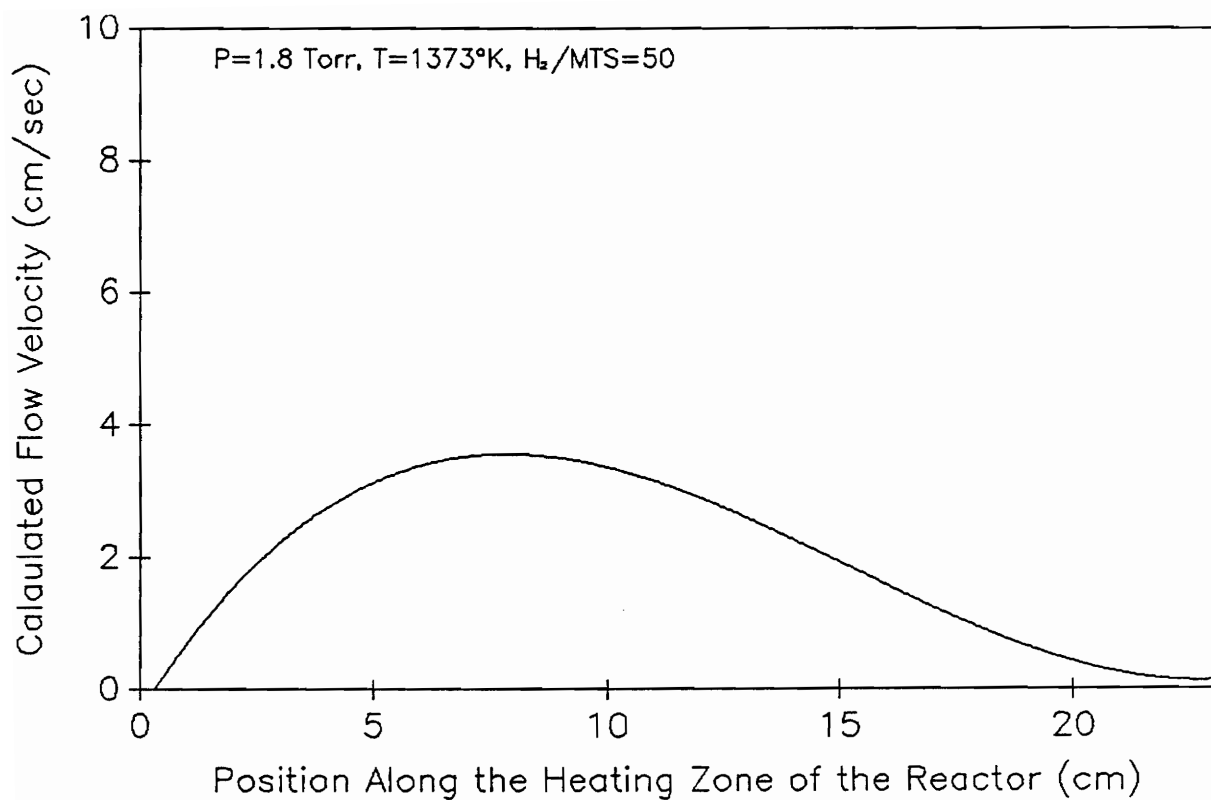


Figure 4.3 The Flow Velocity Profile with Total Gas Pressure = 1.8Torr; Deposition Temperature = 1373° K and $H_2$/MTS = 50

found to be almost identical with or without considering this viscosity–temperature dependence. In fact, with the range of temperatures used, changes of the viscosity coefficient due to considering the viscosity–temperature dependence are very small. Therefore, viscosity of the gas mixture was assumed to be constant for all the calculations to improve the computational efficiency of the CVD FEM model.

As far as the boundary conditions are concerned, at the front end of the CVD reactor, concentrations of the MTS and hydrogen species were given according to the dilution ratio, while concentrations of other species were assumed to be zero. At the exit, the adiabatic condition was used for all the gas species.

Details of the hot–wall CVD process modeling can be found in references [48,66].

## 4.5 Results and Discussion

### 4.5.1 Deposition Rates of SiC at T=1273°K to 1423°K; P=1.8, 5.0, 8.0 Torr; and $H_2$/MTS=50

Typical examples of cross–section SEM of SiC thin films deposited on Si(100) substrates are shown in Figure 4.4 with the following experimental conditions: deposition temperature = 1050°C, $H_2$/MTS = 100, total inlet gas pressure = 1.8, 5.0, 8.0 Torr.

Relatively rough SiC film surface with small defects on the Si substrate was observed for the deposition with a 8.0 Torr gas pressure, as shown in Figure 4.4c. The formation of these defects on the Si substrate are because of the Cl radicals from the MTS precursor. For the depositions with lower gas pressures (i.e., 1.8 Torr

and 5.0 Torr), the Si substrate is found to be free of defects, and the SiC film surface is much more smooth compared to the deposition with a 8.0 Torr gas pressure.

Deposition rates versus deposition temperatures at various pressures are shown in Figure 4.5. The deposition rates were measured on a specimen positioned in the center of reactor, as shown in Figure 4.2. For Figure 4.5, the value of "m" is equal to the slope of the regression line, while "r" represents the fitness of the regression line. Note that the value of "m" represents the effective activation energy for the deposition process using the lumped reaction scheme.

As the total pressure was increased from 1.8 Torr to 5.0 Torr, the effective activation energy of the deposition process was decreased to 44% of the previous value. With further increase of the total pressure to 8.0 Torr, the effective activation energy was reduced significantly, especially when the deposition temperature was higher than 1273°K. Under these conditions, the effective activation energy was almost zero.

For the study of effective order of the reaction, the deposition rates were plotted in Figure 4.6 as a function of the total pressure with deposition temperatures varied from 1273°K to 1423°K in intervals of 50°K.

Below 1423°K, the effective order of the reaction decreased with an increasing gas pressure. At 1423°K, the SiC deposition rate at the reactor center was independent of the gas pressure.

One may quickly interpret these changes, in both the effective activation energy and reaction order of the SiC deposition process, as an indication of changes in the deposition mechanism. However, one should be very careful before drawing such conclusions because precursor depletion due to the deposition on the reactor

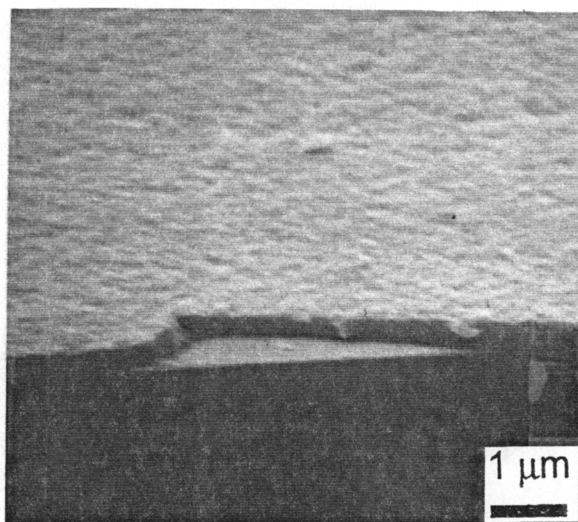


(a): 1.8 Torr

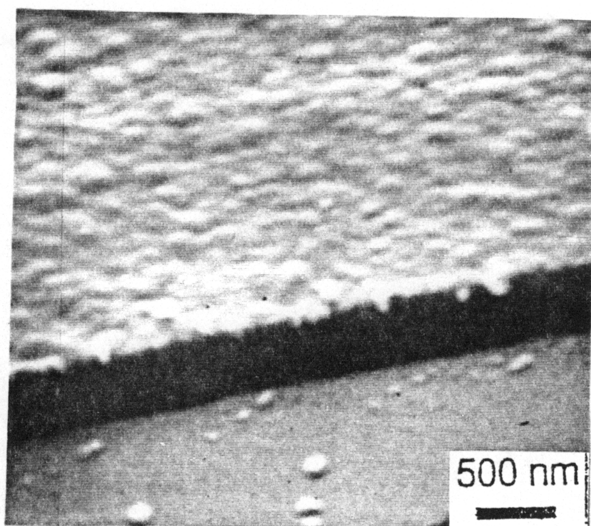


(b): 5.0 Torr

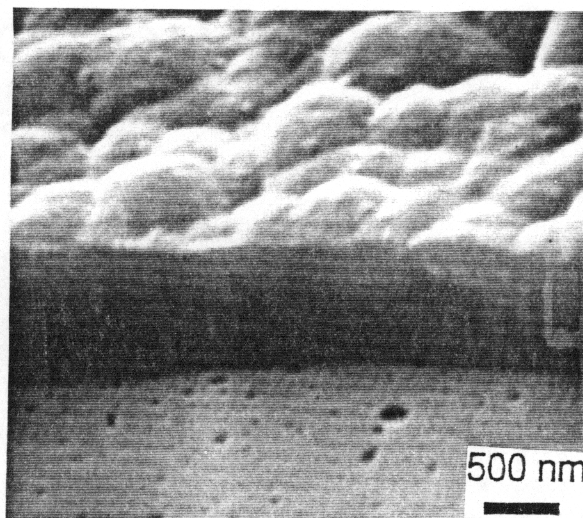


(c): 8.0 Torr

Figure 4.4 SEM Micrographs of the SiC Thin Films on Si(100) Substrates Growth at T = 1050° C and $H_2$/MTS = 100

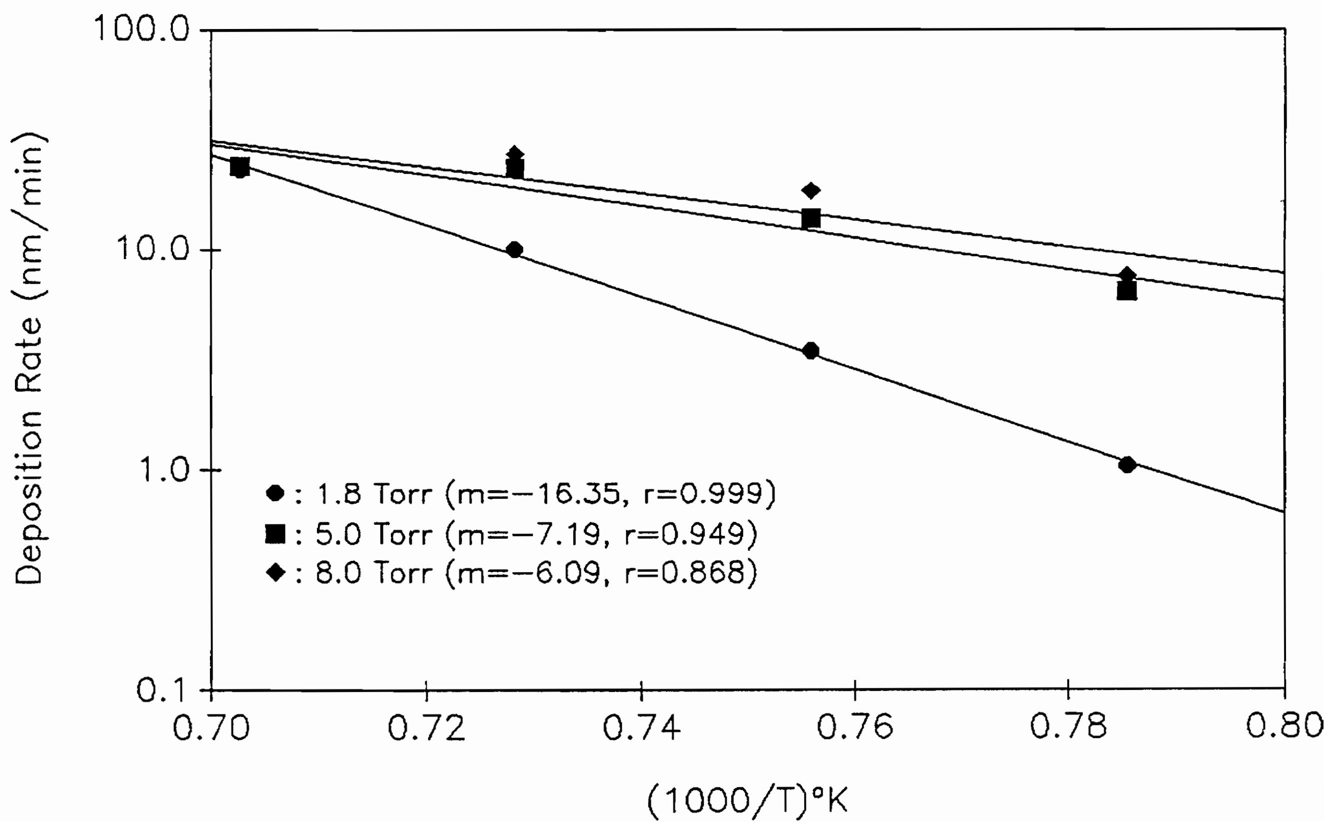


Figure 4.5 SiC Deposition Rates as a Function of Deposition Temperatures

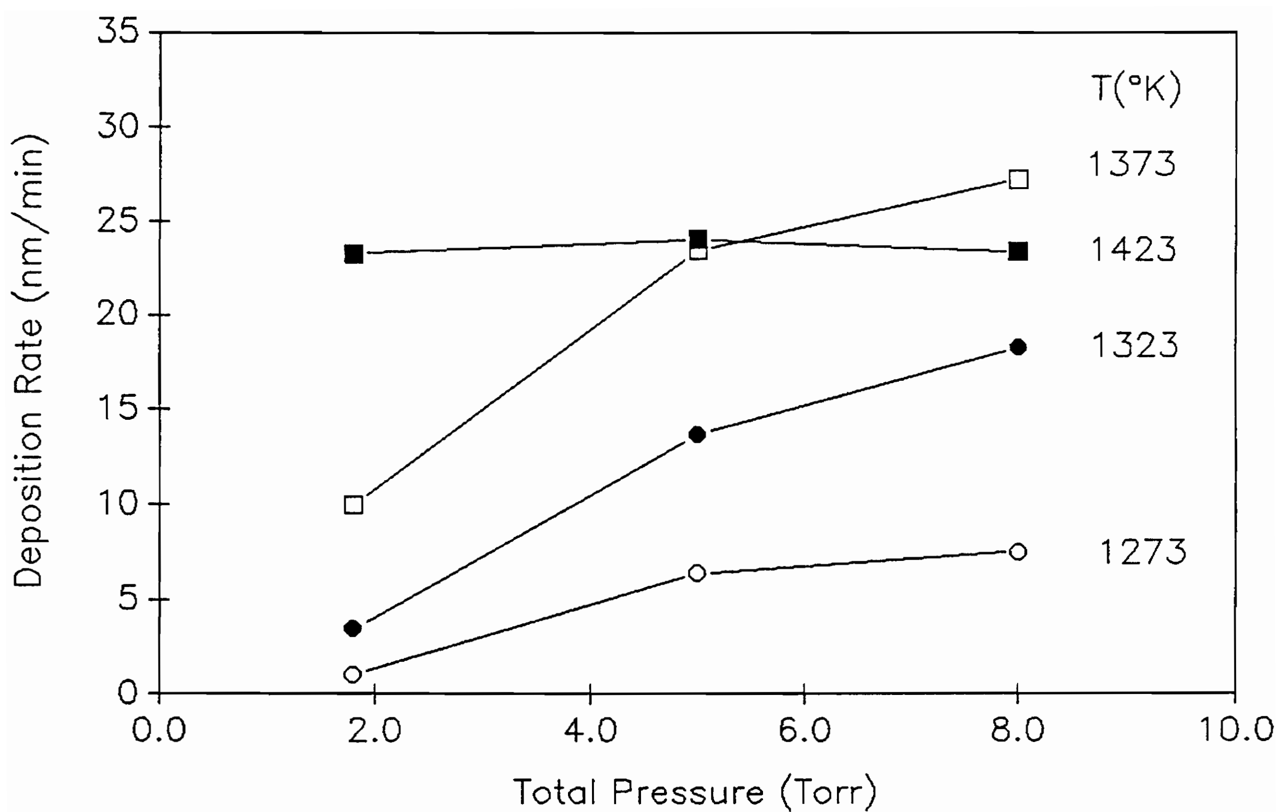


Figure 4.6 SiC Deposition Rates as a Function of the Total Inlet Gas Pressure

walls in zone 1, as shown in Figure 4.2, might significantly change the deposition rates on the specimen at the center of the reactor depending on the experimental conditions.

Typical pressure profiles are shown in Figure 4.7 for $MTS_{(g)}$ and $IP_{Si(g)}$ components with 1373°K deposition temperature and 1.8 and 5.0 Torr total pressure. In general, as the total pressure is increased, concentrations of the intermediates are increased. As a result, the SiC deposition rate at the center of the reactor is increased.

On the other hand, when the residence time of the gas mixtures increases due to the pressure increase, more gas species, including MTS, intermediates, and by–products, are consumed on the reactor walls before they can reach the center of the reactor. This depletion process decreases local concentrations of the intermediate species at the reactor center, which results in a lower deposition rate.

The deposition temperature has a similar effect on the SiC deposition rate at the reactor center, that is, a hot–wall CVD process with higher deposition temperatures produces more intermediate species, which can result in higher deposition rates. However, higher temperatures might also lead to lower deposition rates at the reactor center because the depletion effect is more active as the temperature is increased.

For our hot–wall CVD experiments, the depletion effect is becoming more prominent as both the total pressure and deposition temperature are increased, as shown in Figure 4.5. As a result, the effective activation energy of the deposition process is decreased as the total pressure is increased. This phenomena can also be used to explain changes of effective order of the reaction, as shown in Figure 4.6. At 1423°K, the concentration increase of the intermediates due to the pressure increase

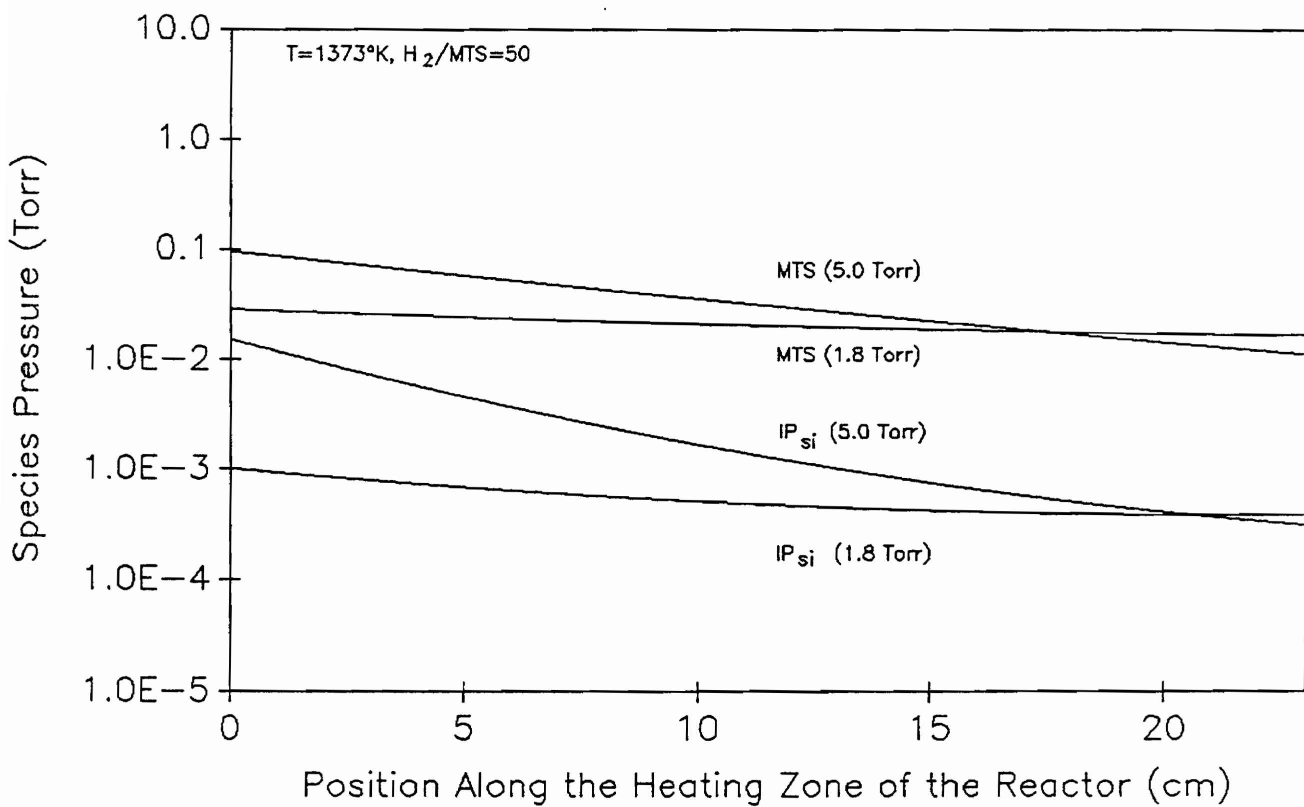


Figure 4.7 Pressure Profiles of $MTS_{(g)}$ and $IP_{si(g)}$ Components with P=1.8, 5.0 Torr, T=1373° K, $H_2/MTS$ = 50

is offset by the depletion effect. As a result, effective order of the reaction is deteriorated to zero.

It is obvious that changes in the deposition rate at the center of a hot–wall reactor resulting from changes in the deposition temperature and total pressure cannot be easily determined without the understanding of the concentration profiles of various species as a function of reactor geometry and experimental conditions. In other words, the depletion effect must be taken into consideration in analyzing the deposition rate data for understanding the reaction mechanism.

We have successfully incorporated the depletion effects in a CVD FEM program by coupling the transport processes with the deposition kinetics. With the help of such a program, the deposition rate changes are interpreted and a model for SiC deposition was proposed and the kinetic data were obtained.

### 4.5.2 Determination of the Kinetic Data

Neuschutz et al. conducted a series of SiC CVD experiments using $MTS/H_2$ precursors with deposition temperature ranging from 750° C to 850° C, and the total pressure being equal to 1 bar. In Neuschutz's CVD experiments, the methane gas ($CH_4$) was added in order to suppress the formation of elemental silicon [59].

Methane ($CH_4$) is known to be the major gas species that contains the carbon molecules of the decomposed MTS gas mixture [56,69,75] in this low temperature range. Therefore the addition of the $CH_{4(g)}$ (the concentration of which is about the same as that of the hydrogen) not only increases the concentration of the carbon–carrying species, but also hinders the decomposition of the MTS precursor according to equation (4.1). It was thus assumed that the degree of dissociation, $\alpha$,

of the MTS molecules is lower than 10% in this low deposition temperature range.

The concentration of the carbon–carrying species, $IP_{c(g)}$, was assumed to be that of the methane gas. From equation (4.1), the concentration of the silicon–carrying species, $IP_{si(g)}$, can be expressed as,

$$[IP_{si}] = \alpha[MTS] = \sqrt{K_g[H_2]/[CH_4]}\sqrt{[MTS]} \qquad (4.10)$$

Note that the assumption that $\alpha$ was less than 10% was used in the derivation of equation (4.10).

From equation (4.4), the deposition rate ($mol/cm^2$–sec) of the SiC can thus be written as,

$$k_tK_{a1}K_{a2}[CH_4]\sqrt{K_g[H_2]/[CH_4]}\sqrt{[MTS]}/(1+K_{a1}\sqrt{K_g[H_2]/[CH_4]}\sqrt{[MTS]}+K_{a2}[CH_4])^2 \qquad (4.11)$$

Note that with all these simplifications, the resulting expression of the SiC deposition rate is proportional to the square root of the MTS concentration, as was also indicated by Neuschutz et. al [59].

Three groups of parameters, that is, $(k_tK_{a1}K_{a2}\sqrt{K_g})$, $(K_{a1}\sqrt{K_g})$, and $K_{a2}$, can be found in equation (4.11). Values of these parameters were determined by fitting the deposition rate data of Neuschutz et al. with equation (4.11). The density of the SiC film was assumed to be 3.17 $g/cm^3$ in these calculations.

The temperature dependence of the three groups of parameters is listed in Table 4.2. As shown in Figure 4.8, the agreement between the modeling results and the reported data by Neuschutz et al. is very good.

Values of the rate constant of the surface reaction (4.3a) can be obtained from the division of ($k_t K_{a1} K_{a2} \sqrt{K_g}$) by ($K_{a1}\sqrt{K_g}$) and $K_{a2}$. Arrenhius expressions of kinetic data were found to be,

$$k_t \ (mol/cm^2\text{–}sec) = 4.6E+05 \exp[(-265.1 \ kJ/mol)/RT] \quad (4.12a)$$

$$K_{a1}\sqrt{K_g} = 2.2E+07 \exp[(-37.7 \ kJ/mol)/RT] \quad (4.12b)$$

$$K_{a2} \ (cm^3/mol) = 7.1E+09 \exp[(-33.1 \ kJ/mol)/RT] \quad (4.12c)$$

The free energy of the equilibrium constant ($K_{a1}$) of the adsorption process (4.2b) is around 30 kJ/mol, which is reasonable for the physisorption process [70].

Table 4.2 Temperature Dependence of the Kinetic Data ($k_t K_{a1} K_{a2}\sqrt{K_g}$, $K_{a1}\sqrt{K_g}$, $K_{a2}$) of SiC Deposited from MTS/$H_2$ Precursors. These kinetic data were used to fit the SiC deposition rates reported by Neuschutz et al., as shown in the Figure 4.8

| T(°K) | $k_t K_{a1} K_{a2}\sqrt{K_g}$ | $K_{a1}\sqrt{K_g}$ | $K_{a2}$ |
|---|---|---|---|
| 1118 | 1.9E+08 | 3.9E+05 | 2.0E+08 |
| 1093 | 7.9E+07 | 3.5E+05 | 1.9E+08 |
| 1043 | 1.4E+07 | 2.9E+05 | 1.6E+08 |

In order to determine the equilibrium constant ($K_g$) of the gas phase decomposition process (4.1), the equilibrium constant ($K_{a1}$) of the adsorption process (4.2a) has to be determined first.

Furthermore, as pointed out by Kalidindi et al. [48], for the chemical vapor deposition process with an extended heating zone, such as the hot–wall CVD process and the CVI process, systems with the same equilibrium constant $K_g$, which is equal to $k_1/k_{-1}$, but different values of the forward and backward rate constants may result in dramatically different deposition rate profiles due to the depletion effect of the precursors over the heating zone. Therefore, it is important to decompose the kinetic data $k_1$ and $k_{-1}$ from the equilibrium constant $K_g$.

The three kinetic parameters, that is, $K_{a1}$, $k_1$ and $k_{-1}$, were obtained by matching the deposition rates of our own hot–wall CVD experiments with the CVD FEM model. Comparisons between the modeling predictions and the experimental results are shown in Figure 4.9. The agreement between the modeling calculations and experimental results is good except for the case of T=1423°K and P=8.0 Torr, at which the modeling calculation predicted a higher depletion effect.

Estimated values of the three kinetic constants with respect to the deposition temperature are listed in Table 4.3. The Arrenhius expressions of the parameters can be written as,

$$K_{a1}\ (cm^3/mol) = 0.5E{+}11\ \exp[(-21.6\ kJ/mol)/RT] \qquad (4.13a)$$

$$K_g\ (mol/cm^3) = 0.2E{-}6\ \exp[(-32.0\ kJ/mol)/RT] \qquad (4.13b)$$

$$k_1\ (cm^3/mol\text{-}sec) = 0.2E{+}26\ \exp[(-448.2\ kJ/mol)/RT] \qquad (4.13c)$$

$$k_{-1}\ (cm^6/mol^2\text{-}sec) = 1.1E{+}32\ \exp[(-416.2\ kJ/mol)/RT] \qquad (4.13d)$$

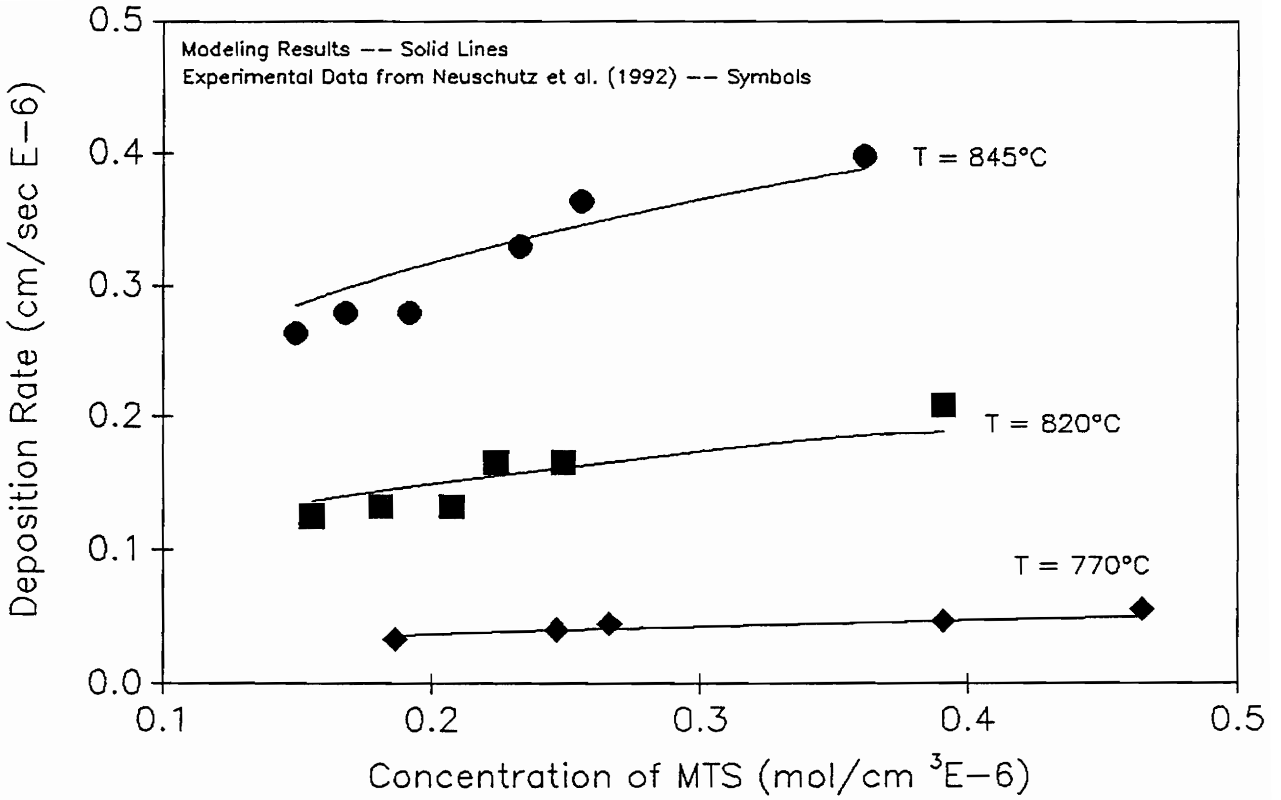


Figure 4.8 Comparisons between Modeling Predictions and Reported Data from Neuschutz's SiC CVD Experiments

Table 4.3 Temperature Dependence of the Kinetic Data ($K_{a1}$, $k_1$, $k_{-1}$) of SiC Deposited from $MTS/H_2$ Precursors. These kinetic data together with $K_{a2}$ and $K_t$ obtained in Table 4.2 were used in the CVD FEM model to calculate the SiC deposition rates, as shown in the figures 4.9 and 4.10

| T(°K) | 1273 | 1323 | 1373 | 1423 |
|---|---|---|---|---|
| $K_{a1}$(E+09) | 6.5 | 7.0 | 7.5 | 8.0 |
| $k_1$(E+07) | 0.9 | 3.5 | 15.0 | 80.0 |
| $k_{-1}$(E+15) | 0.9 | 3.3 | 13.0 | 61.0 |

The free energy of the equilibrium constant ($K_{a1}$) of the adsorption reaction (4.2a) is smaller than that of the reaction (4.2b), and the value of $K_{a1}$ is about two orders of magnitude higher than $K_{a2}$. This result implies that the surface concentration of the silicon–carrying species is much higher than that of the carbon–carrying species.

The kinetic data obtained were further used to estimate the SiC deposition rates with the $H_2/MTS$ ratio being equal to 10 and 100. For these deposition experiments, the total pressure was equal to 1.8 Torr, and the deposition temperature were varied from 1273°K to 1423°K. The correlation between the modeling results and experimental data is good, as shown in Figure 4.10.

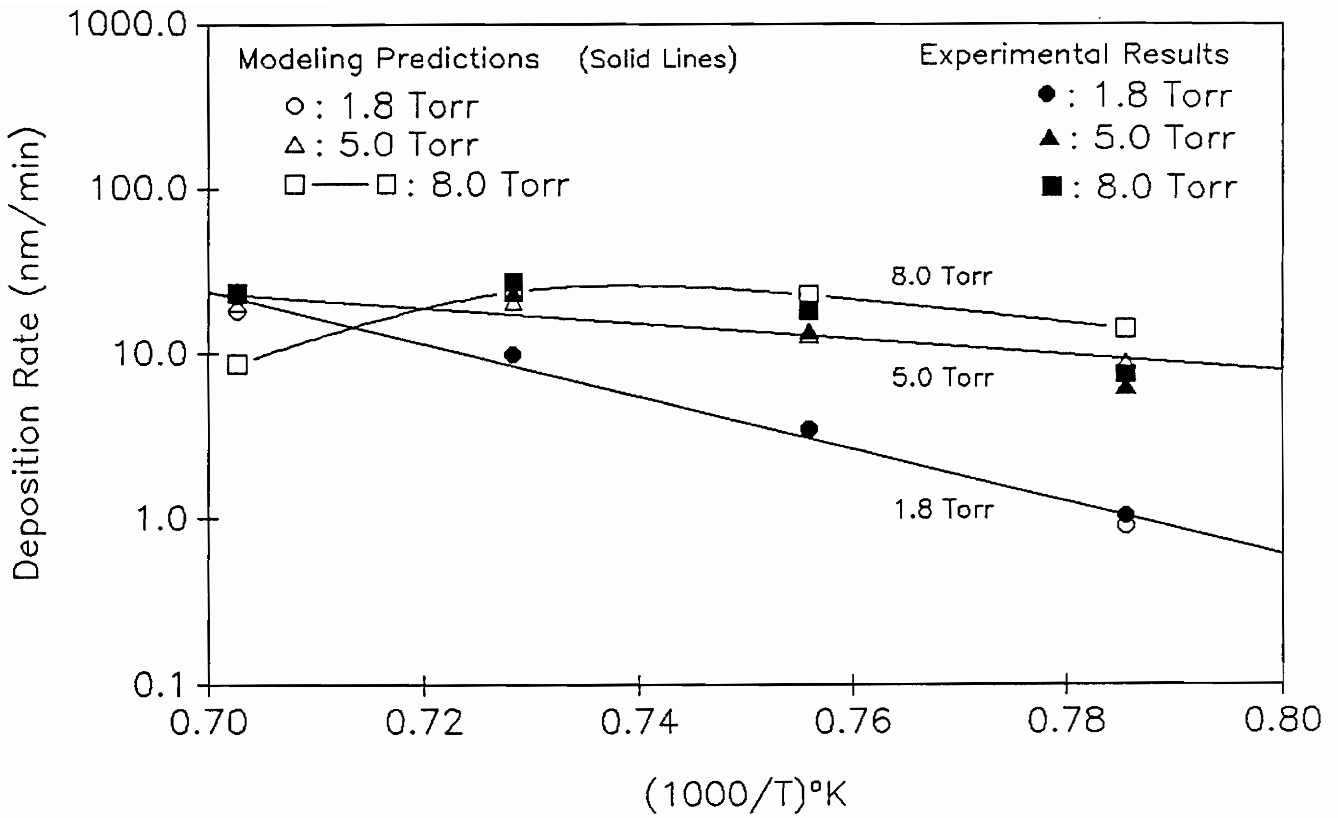


Figure 4.9 Comparisons between Modeling Predictions and Experimental Results; with P=1.8, 5.0 and 8.0 Torr; T={1273, 1323, 1373, 1423}° K; $H_2$/MTS = 50

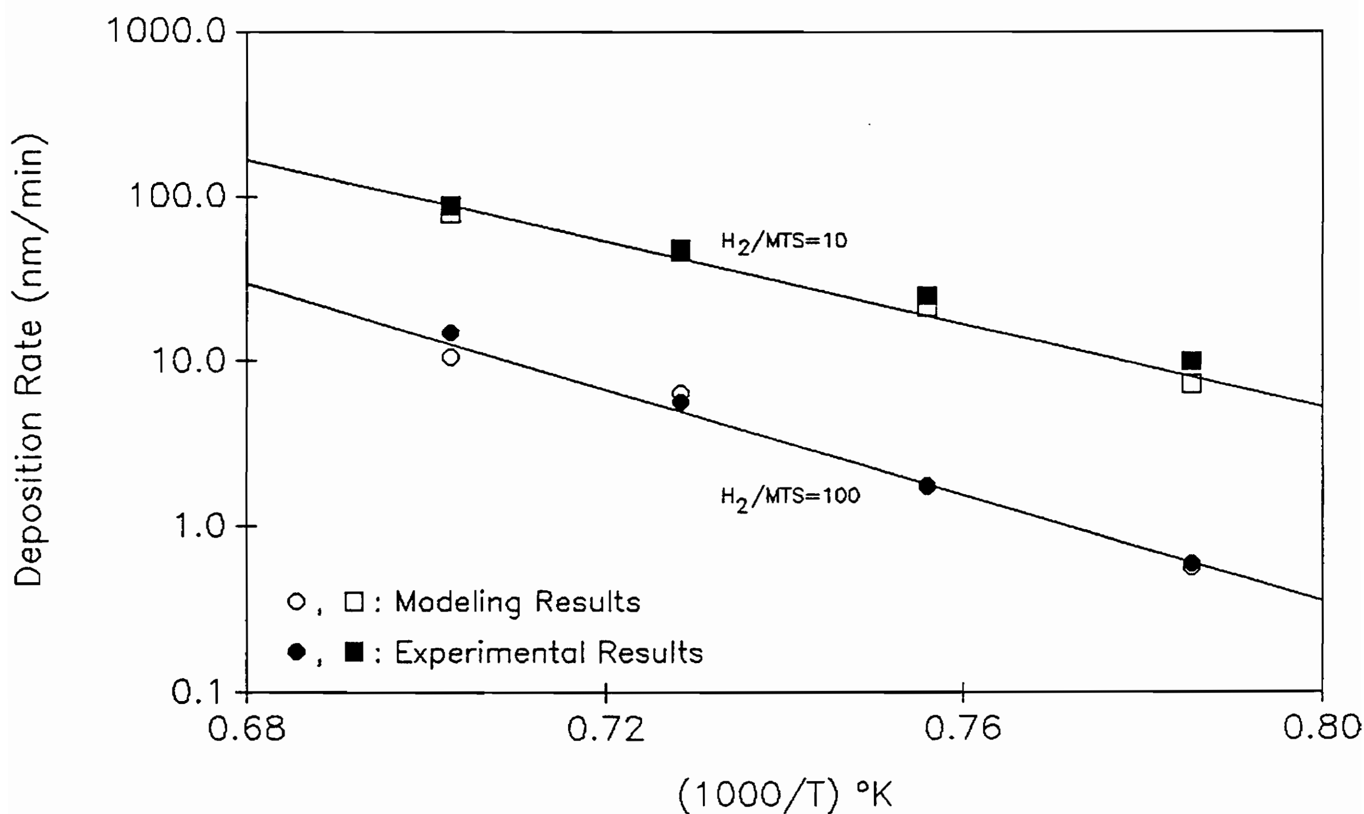


Figure 4.10 Comparisons between Modeling Predictions and Experimental Results; with P=1.8Torr; T={1273, 1323, 1373, 1423}° K; $H_2$/MTS=10, 100

## 4.6 Summary

A kinetic model, including gas phase decomposition process, adsorption process of the intermediate species and surface reaction of the adsorbed intermediate species, for the SiC deposited from $MTS/H_2$ precursors was presented in this paper. The proposed model is a definite improvement over the previously used lumped first order reaction model.

A finite element model, which considers the kinetics and transport process of the gas species, was developed to analyze the hot–wall CVD process. Values of the obtained equilibrium constant ($K_{a1}$) of the adsorption process of silicon–carrying species was about two orders of magnitude higher than that of the carbon–carrying species. The equilibrium constant ($K_g$) of the gas phase decomposition process was decomposed into individual forward ($k_1$) and backward ($k_{-1}$) reaction rate constants , respectively, as 0.2E+26 exp[(–448.2 kJ/mol)/RT] and 1.1E+32 exp[(–416.2 kJ/mol)/RT].

Experimental data of hot–wall SiC CVD process with respect to the variance of system pressure and temperature were in good agreement with the modeling predictions. Changes of the effective activation energy and reaction order of the deposition process can be attributed to the consumption of gas species on the hot reactor walls. With the incorporations of both gas phase and surface reactions of the SiC CVD process, this kinetic model is more suitable for analyzing the deposition rate profiles in both the CVI and hot–wall CVD processes than the traditional lumped first order kinetic model.

This paper titled

"A Finite Element Model for the Study of the Forced-Flow Thermal-Gradient Chemical Vapor Infiltration Process"

was submitted to
Journal of Electrochemical Society

# Chapter 5
# A Finite Element Model for the Study of the Forced–Flow Thermal–Gradient Chemical Vapor Infiltration Process

## 5.1 Abstract

A mathematical model was developed to study the forced–flow thermal–gradient chemical vapor infiltration (FCVI) process of silicon carbide using methyltrichlorosilane and hydrogen precursors. Based on a previous study by the same authors, both gas phase and surface reactions were considered in this FCVI model to predict appropriate deposition rate profiles under forced–flow conditions. The pressure gradient, resulting from both chemical reactions and imposed hydrogen pressure gradient, was used to calculate the induced forced–flow based on Darcy's law. With inclusion of the gas phase reaction, deposition rates near the entrance were found to increase during the FCVI process as a result of the increased residence time of the gas species. This resulted in higher residual porosity under certain processing conditions.

Effects of deposition temperature and vapor pressure variations on the density profiles of the composite preform were studied. Because advantages of the ambient–pressure FCVI process (APFCVI) are likely to be limited by the equipment, other options, such as the low pressure FCVI process (LPFCVI), were investigated to obtain desirable deposition rate profiles. These two processes were combined to optimize the FCVI process for large size specimens.

## 5.2 Introduction

Recently, the chemical vapor infiltration (CVI) process has emerged as a strong candidate for fabrication of ceramic matrix composites (CMCs) because of its ability to create all major families of ceramic matrices, to produce well–defined shapes with little dimensional changes, to process at low temperature, and to reduce the interactions between the fiber and the matrix [3–5]. The development of forced–flow thermal–gradient chemical vapor infiltration (FCVI) processes makes the CVI processes even more competitive because they ensure better uniformity of the deposited matrix and can reduce the processing time significantly [6] under certain conditions.

In this work, a mathematical model was developed to study the FCVI process of silicon carbide (SiC) using methyltrichlorosilane (MTS) and hydrogen ($H_2$) precursors. The finite element method (FEM) was used to solve the nonlinear equations of continuity governing the FCVI processes.

Most FCVI models [14,16–17] use lumped reaction kinetics to describe the chemical reactions of the FCVI processes. However, based on a previous study by the same authors [66], it was found that improvements in the deposition thickness profiles by using the forced–flow technique are fundamentally different for FCVI processes with different rate–controlling steps. For the surface reaction controlled FCVI process, the deposition rates increase with an increase in forced–flow rate. On the other hand, the deposition rate profiles of the gas phase reaction controlled FCVI process decrease with a forced–flow rate increase. Because the rate controlling step of the FCVI process might be changed with changes in the thermal profiles during the deposition process, it is very important to consider explicitly the

individual reactions in order to study the optimum processing conditions.

The kinetic model developed by the same authors [76], which considered both the gas phase and surface reactions of SiC deposited from MTS precursor, was used in this modeling work.

Relationships between the operational conditions, including thermal profiles and vapor pressures, and the quality of the FCVI process, as determined by the processing time and resultant composite density profiles, were particularly investigated.

This process model will be highly valuable in optimizing the FCVI process to produce high quality components and eliminate the need for expensive trial experiments.

### 5.3 Mathematical Formulations of the FCVI Process

It was assumed that the fluid flow within the fibrous preform follows Darcy's law. The heat generated by chemical reactions was neglected due to the small reaction rate. Based on these assumptions, the FCVI process can be described by the law of conservation of mass and energy as [14,17,26,66]:

<u>Law of conservation of mass</u>

$$\nabla \cdot (\vec{N}_i^{du} + \vec{N}_i^{cv}) = \Sigma R_{ij} \tag{5.1}$$

<u>Law of conservation of energy</u>

$$-\nabla \cdot (K \nabla T) + \rho_g C_p (\vec{V} \cdot \nabla T) = 0 \tag{5.2}$$

with:

- $\vec{N}_i^{du}$ (mol/cm$^2$–sec) = Diffusion flux of gaseous species i $= -\frac{D_{i\,(eff)}}{RT}\nabla p_i$; both Knudsen diffusion and ordinary diffusion mechanisms were considered
- $\vec{N}_i^{cv}$ (mol/cm$^2$–sec) = Convection flux of gaseous species i = $\vec{V}p_i$

$$= -\frac{Bp_i}{\mu RT}\nabla\Sigma p_i$$

- $R_{ij}$ (mol/cm$^3$–sec) = Reaction flux of gaseous species i associated with the chemical reaction j
- $p_i$ (atm) = Vapor pressure of the gaseous species i
- T ($^\circ$K) = Deposition temperature
- $\rho_g$ (mol/cm$^3$), $\mu$ (atm–sec) and $C_p$ (j/mol–$^\circ$K) = Density, viscosity and thermal capacity of the mixture gas
- $D_{i\,(eff)}$ (cm$^2$/sec) = Effective diffusion constant of species i in the porous medium
- K (Watt/cm–$^\circ$K) = Effective thermal conductivity of the porous medium
- B (cm$^2$) = Permeability of the porous medium
- R = Gas law constant = 82.05 cm$^3$atm/mol–$^\circ$K = 1.987 cal/mol–$^\circ$K

A schematic diagram of the FCVI process is shown in Figure 5.1. Note that only half of the domain shown in Figure 5.1 has to be considered due to the symmetrical nature of the domain and its associated boundary conditions.

Chemical reactions considered in this study are those of the SiC chemical vapor deposition (CVD) process using MTS and $H_2$ precursors. The kinetic model proposed by Tsai et al. [76], which considered both gas phase and surface reactions, was used in this study.

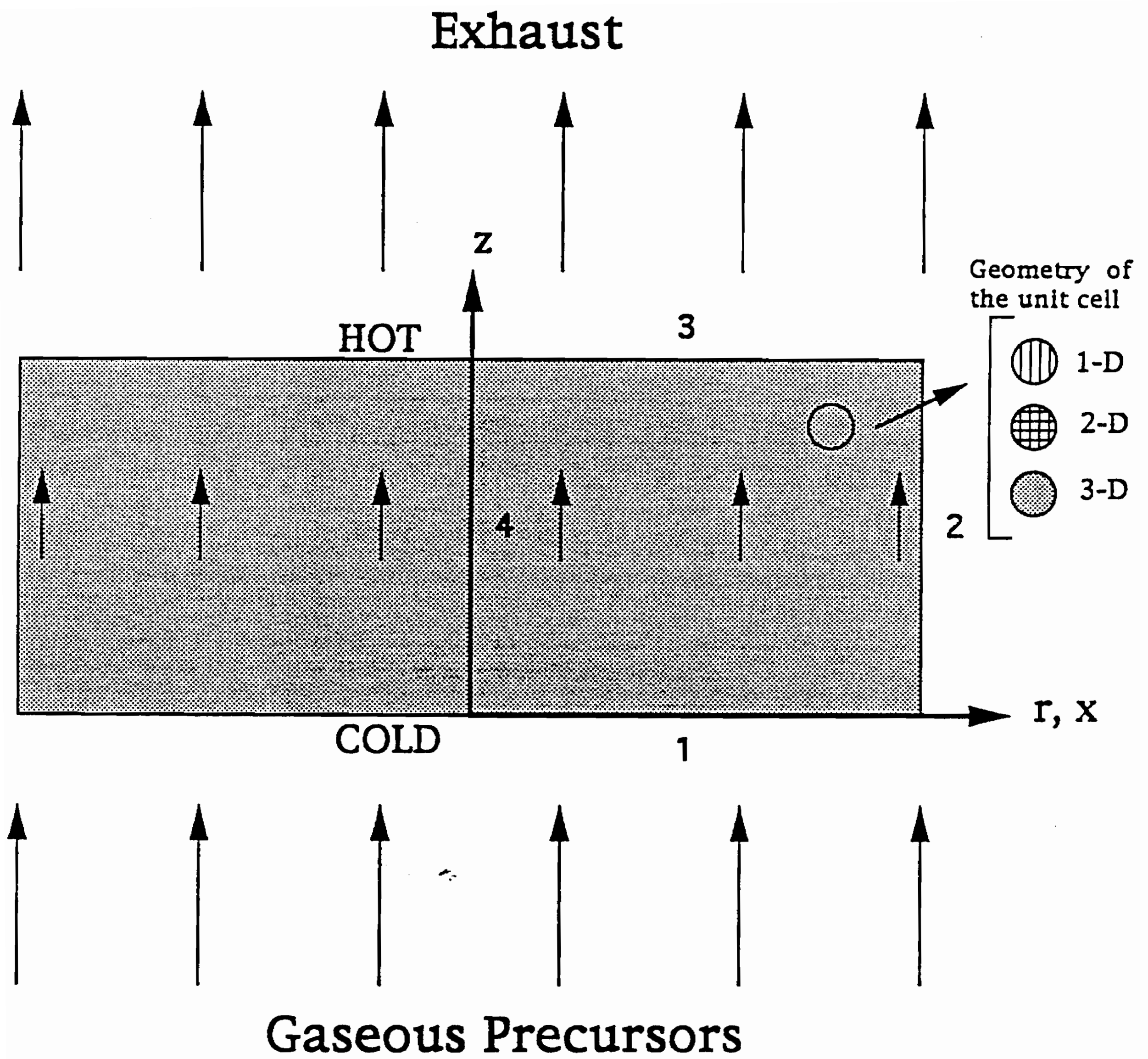


Figure 5.1 A Schematic Diagram of the Forced–Flow Thermal–Gradient Chemical Vapor Infiltration Process

In the kinetic model proposed by Tsai et al, the MTS precursor was assumed to be decomposed in the gas phase into two intermediate species, one bearing silicon ($IP_{si}$) and the other bearing carbon ($IP_c$). This assumption is based on the previous studies of the CVD SiC process using the MTS precursor [56,67,69]:

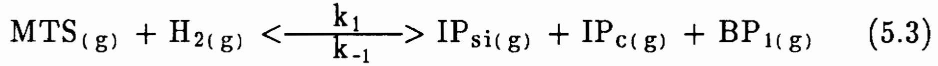

$$MTS_{(g)} + H_{2(g)} \underset{k_{-1}}{\overset{k_1}{\longleftrightarrow}} IP_{si(g)} + IP_{c(g)} + BP_{1(g)} \quad (5.3)$$

Intermediates, $IP_{si(g)}$ and $IP_{c(g)}$, were adsorbed onto the surface sites,

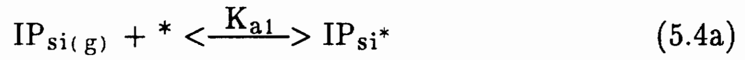

$$IP_{si(g)} + * \overset{K_{a1}}{\longleftrightarrow} IP_{si}* \quad (5.4a)$$

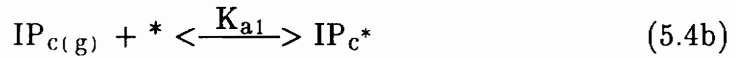

$$IP_{c(g)} + * \overset{K_{a1}}{\longleftrightarrow} IP_{c}* \quad (5.4b)$$

and reacted to form the silicon carbide and other gaseous by–product $BP_{2(g)}$.

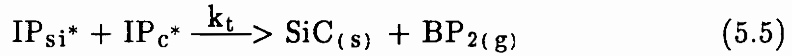

$$IP_{si}* + IP_{c}* \overset{k_t}{\longrightarrow} SiC_{(s)} + BP_{2(g)} \quad (5.5)$$

The deposition rate of SiC can be expressed as:

$$k_t[IP_{si}*][IP_c*]\ (mol/cm^2\text{–}sec) = k_t K_{a1} K_{a2}[IP_{si}][IP_c]/(1+K_{a1}[IP_{si}]+K_{a2}[IP_c])^2$$

Kinetic data of this model are listed as follows [76]:

$$K_{a1}\ (cm^3/mol) = 0.5E+11 \exp[(-21.6\ kJ/mol)/RT]$$

$$K_{a2}\ (cm^3/mol) = 7.1E+09 \exp[(-33.1\ kJ/mol)/RT]$$

$$k_t\ (mol/cm^2\text{–}sec) = 4.6E+05 \exp[(-265.1\ kJ/mol)/RT]$$

$$k_1\ (cm^3/mol\text{–}sec) = 0.2E{+}26\ \exp[(-448.2\ kJ/mol)/RT]$$

$$k_{-1}\ (cm^6/mol^2\text{–}sec) = 1.1E{+}32\ \exp[(-416.2\ kJ/mol)/RT]$$

In addition to reaction kinetics, knowledge of both the structural properties (for example: the accessible porosity, permeability and reaction area per unit volume) and transport coefficients (for example: the Knudsen and ordinary diffusion coefficients) are necessary to model the FCVI process.

In this study, fibers of the preform were assumed to be randomly overlapped. Three different arrangements of fibers inside a unit cell were assumed: one–directional (uni–directional fiber bundle), two–directional (woven type preform), and no preferred orientation, as shown in Figure 5.1.

Estimations of structural properties of fibrous medium and effective diffusion coefficients were mainly based on references [20–22]; each used the Monte Carlo simulation technique to study the gaseous diffusivities in structures of overlapping fibers. Accessible porosity for fibrous preform with different packing geometries, that is, 1–D, 2–D or 3–D microstructure, were fitted to polynomial expressions to be used in the FCVI model. Other references [77–82] were used to estimate additional modeling parameters, such as permeability, effective thermal conductivity and density of the gas mixture. The information used in estimating the structural and transport properties were included in Appendix A.

The fiber length per unit volume (L) is not uniform within the fibrous medium. For example, for the 2–D woven type fibrous preform, a high L value represents the porosity inside the fiber bundles, while a low L value represents the porosity between the fiber bundles. In order to account for this non–uniform effect, a density function, f(L), was used to describe the distribution of parameter L inside the unit

cell. Accordingly, the porosity at any point can be computed as:

$$\phi = \int_{L_1}^{L_2} \exp(-\pi L R_f^2) f(L) dL$$

$$\text{with} \int f(L)dL=1, \text{ and } R_f = \text{Fiber radius}$$

The boundary conditions of the temperature and pressure also have to be specified in order to calculate the deposition thickness profiles of the FCVI process. Temperatures were fixed at the entrance and exit sides, that is, boundary 1 and 3, of the fibrous preform. At the entrance, vapor pressures of the MTS species were given according to the dilution ratio, and vapor pressures of the intermediates and by–products were assumed to be zero. Vapor pressures of the $H_2$ species were assigned at both the entrance and exit sides to simulate the forced–flow process. At the exit, the adiabatic pressure conditions were used for all other gaseous species except $H_2$ species.

Symmetric conditions were used for both thermal and pressure calculations along the boundary 4, while the adiabatic thermal and impermeable pressure [14] conditions were used along the boundary 2. Both rectangular and cylindrical coordinates were considered in the FCVI modeling.

## 5.4 The Finite Element Modeling

A Fortran programming code based on the finite element method (FEM) [43] was developed to implement the FCVI process. There were six degrees of freedom at each node, that is, one degree of freedom for the deposition temperature and five

for the vapor pressures of each species. Three chemical reactions were considered in this FCVI modeling, that is, the forward and backward gas phase reactions and the surface reaction.

10×10 linear rectangular elements were used to discretize the two–dimensional (2–D) domain. Quasi–steady–state solutions of the temperatures and vapor pressures were obtained sequentially at each time step.

A finite element numerical scheme [83], which is included in Appendix B, was used to solve the conduction–convection equation. This technique can provide oscillation–free finite element solutions without introducing the extra upwinding parameter [84–86].

Because of the assumed chemical reaction scheme and the induced forced–flow, the vapor–pressure–solving module of the FCVI model is nonlinear. Direct iteration scheme was employed to solve the nonlinear problem. The following equation was used to ensure the convergence of the vapor pressures:

$$\frac{\sum_{i=1}^{m} \{(\text{solution}_i)_k - (\text{solution}_i)_{k-1}\}^2}{\sum_{i=1}^{m} \{(\text{solution}_i)_k\}^2} \leq 0.05 \qquad (5.6)$$

where $(\text{solution}_i)_k$ represents the solution at node i in the $k^{th}$ iteration step for a particular gaseous component, and m is equal to the total number of nodes.

## 5.5 Numerical Results and Discussion

SiC fibrous disks with the 3–D type fiber arrangement inside the unit cell were chosen to study the FCVI process. The disk radius is 1.26 cm and the disk thickness (t) ranges from 0.6 cm to 2.4 cm. The fiber radius was assumed to be 10 $\mu$m. Densities of the SiC matrix and Nicalon SiC fiber were assumed to be 3.17 g/cm$^3$ and 2.55 g/cm$^3$, respectively, in the calculation of the theoretical density of the fibrous preform.

Because of the boundary conditions used, transverse profiles of the deposition rate, temperature, and density are much more uniform compared to the corresponding axial profiles. Therefore, only the axial profiles along the disk center are shown.

For convenience, two dimensionless parameters, $\omega_1$ and $\omega_2$, are defined:

- $\omega_1 = \text{Density parameter} = \dfrac{\text{Density (at x/r=0, z/t=1.0)}}{\text{Density (at x/r=0, z/t=0.1)}}$

- $\omega_2 = \text{Deposition rate parameter} = \dfrac{\text{Deposition Rate (at x/r=0, z/t=1.0)}}{\text{Deposition Rate (at x/r=0, z/t=0.1)}}$

For the FCVI process, it is preferable to have a deposition rate profile with a deposition rate parameter $\omega_2$ being greater than one to prevent the premature pore blockage problem. For a uniformly densified composite preform, the density parameter $\omega_1$ is equal to 1.0.

### 5.5.1 Influence of the Forced–Flow on the Thermal Profiles

The thermal profile is crucial in determining the deposition rate profiles of the FCVI process. Determinations of the thermal profiles are based on the balance of the conduction and convection heat fluxes. Initially, the gas flow might have a significant effect on the thermal profiles. However, because the permeability decreases during the deposition process, eventually the thermal profile is determined by heat conduction only.

For the thermal profiles shown in Figure 5.2, the furnace temperature ($T_{fu}$) and temperature difference ($\Delta T$) were assumed to be 1223°K and 50°K, respectively. The back pressure of hydrogen was taken to be 1 atm. Thermal profiles with the inlet $H_2$ pressure ranging from 1.2 atm to 2.0 atm were illustrated.

For the fibrous preform with an initial porosity $\phi$ of 0.49, the thermal profile is almost linear, which indicates that the heat transfer is dominated by the heat conduction mechanism. On the other hand, for the fibrous preform with an initial porosity $\phi$ of 0.70, the forced–flow might have significant effects on the thermal profiles depending on the inlet $H_2$ pressure.

For example, as the inlet $H_2$ pressure was increased from 1.2 atm to 2.0 atm, the deposition temperature at axial position of 0.8 changed from 1213.0°K to 1201.7°K, a change of about 23% of the imposed temperature difference $\Delta T$.

With an increase in the medium porosity and imposed $H_2$ pressure gradient, thermal profiles tend toward the ideal thermal profile, as shown in Figure 5.2.

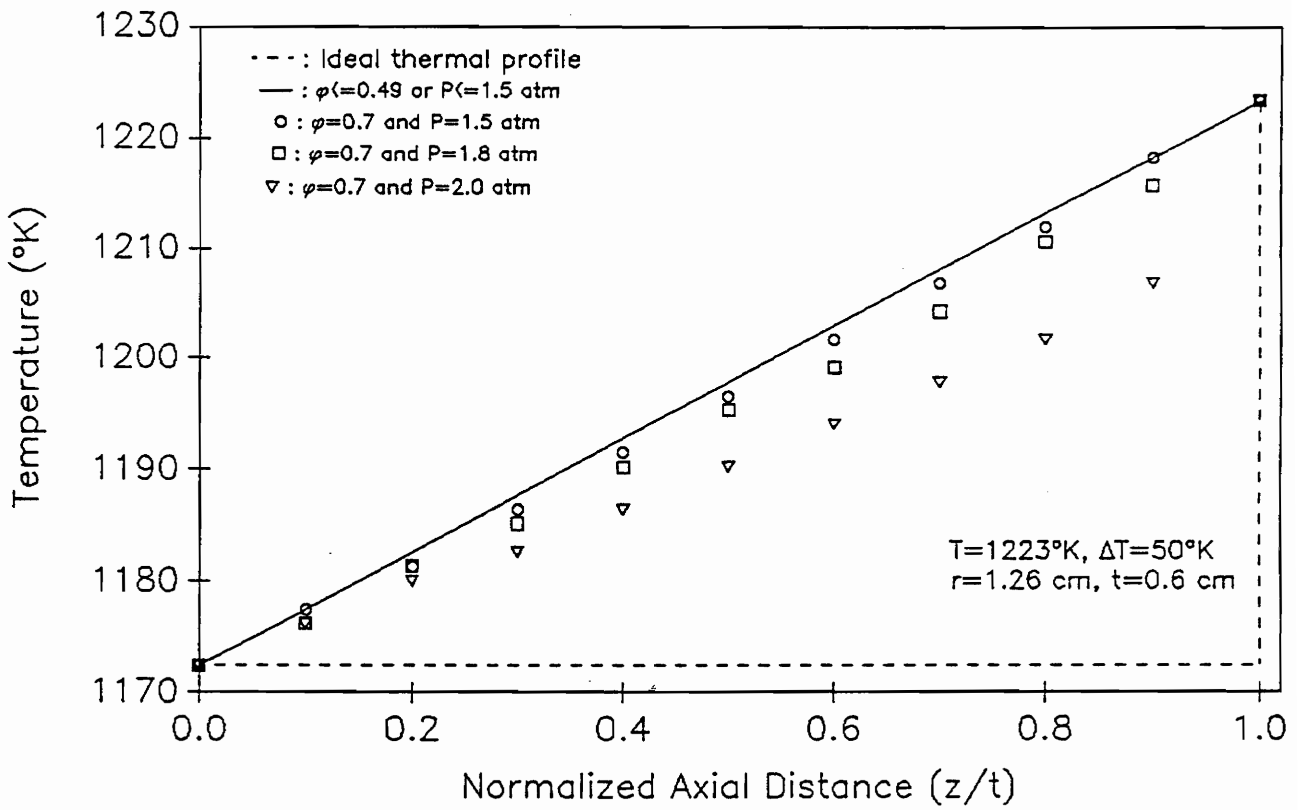


Figure 5.2 Influences of the Forced–Flow Effect on the Thermal Profiles

### 5.5.2 Ambient–Pressure Forced–Flow Thermal–Gradient Chemical Vapor Infiltration Process

Figures 5.3a and 5.4 show the time evolution of deposition rates and density profiles of the fibrous disk. The furnace temperature and temperature difference are equal to 1273° K and 50° K, respectively. Entrance vapor pressures of $H_2$ and MTS are 1.2 atm and 0.12 atm, with a 0.2 atm $H_2$ pressure difference between ends.

The initial porosity of the composite preform is 0.7, which is 25.6% of the theoretical density of the composite preform. The distribution of the parameter L was assumed to be bimodal, that is, values of the density function f(L) were equal to 10000 $\mu m^{-1}$ and 2000 $\mu m^{-1}$ with the parameter L being equal to [1.0e–4, 1.5e–4] $\mu$m and [25.0e–4, 27.5e–4] $\mu$m per unit volume, respectively.

As shown in Figure 5.3a, the deposition rate profile was ascending initially. The corresponding deposition rate parameter $\omega_2$ is 1.17. Because the porosity of the fibrous preform decreases during the deposition, more and more gas species are consumed before they can reach deep inside the preform. The deposition rate profile after 150 minutes of deposition is also shown in Figure 5.3a. As can be seen from Figure 5.3a, the deposition rate profile changed from an ascending curve to a descending curve.

It is interesting to note that, because of the inclusion of the gas phase reaction in the kinetic modeling, deposition rates near the entrance were increased during the deposition process. This phenomenon can be attributed to the higher concentrations of the intermediates near the entrance resulting from longer gas residence time due to the reduced diffusion and convection fluxes. This effect may result in more serious premature pore blockage problem. On the other hand, for those FCVI

models with no consideration of gas phase reactions, deposition rates near the entrance were decreased during the densification process.

In fact, the gaseous residence time effect is of no importance for the FCVI model using the single reaction scheme. With the same entering concentration of reactant species, a more uniform deposition thickness profile with higher deposition rates can always be obtained by increasing the diffusive and/or convection fluxes of the gas species. In other words, the optimum processing condition is the condition with the highest mass transport fluxes possible. This appears to be unreasonable because if the mass transport fluxes are too high, the reactant species might not have enough time to be decomposed into intermediates and reacted on the surfaces to form the solid matrices. On the other hand, for the FCVI model using the multi–reaction scheme, the gaseous residence time effect is crucial in predicting the optimum processing conditions. The diffusive and/or convection fluxes should be chosen such that abundant intermediate species can be produced from the the reactant species before they exit the samples.

The time evolution of corresponding density profiles is shown in Figure 5.4. Medium points with porosity smaller than 0.037 [20–22] were assumed to be blocked. After 195 minutes of deposition, the total density changed from 25.6% to 80.6% of the theoretical density. The density parameter $\omega_1$ was changed from 1.0 to about 0.84.

To improve the uniformity of the density profile and possibly shorten the processing time, the $H_2$ pressure at the entrance was increased to 1.8 atm with other conditions being the same as before. Deposition rate profiles at the beginning and after 60 minutes are shown in Figure 5.3b. Initially, there was an increase of about 50% in the deposition rates due to the forced–flow increase. After 60 minutes of

deposition, the composite density was increased from 25.6% to 64.4% of the theoretical density, as shown in Figure 5.4. At that time, the exit deposition rate decreased from 0.49 $\mu m/min$ to 0.35 $\mu m/min$.

As can be seen in Figure 5.4, with increase in the induced forced–flow by increasing the entrance $H_2$ pressure, the uniformity of the composite is greatly enhanced even with shorter processing time.

### 5.5.3 The Thickness Effect on the Densification

The effect of preform thickness on the densification was also investigated by increasing the disk thickness from 0.6 cm to 1.2 cm and 2.4 cm, respectively. Time histories of the resultant density, with the entrance $H_2$ pressure being equal to 1.2 atm and 1.8 atm, are shown in Figure 5.5.

For the disk with a thickness of 1.2 cm, the final density parameter $\omega_1$ can be improved from 0.47 to 0.57 with a shorter processing time by increasing the inlet $H_2$ pressure from 1.2 atm to 1.8 atm. However, this improvement decreases sharply when the disk thickness is increased to 2.4 cm, as shown in Figure 5.5. For the disk with a thickness of 2.4 cm, the improvement resulting from the increase of inlet $H_2$ pressure to 1.8 atm is very limited.

Before using steeper pressure gradients to improve the uniformity of the density profile of large size specimens, it is important to understand changes of the induced gas flow resulting from the imposed pressure gradient. In Figures 5.6a and 5.6b, the gas flow was computed as the product of the gaseous pressure gradient and the medium permeability and then normalized with respect to the maximum gas flow. Calculations are based on Darcy's law, as described previously.

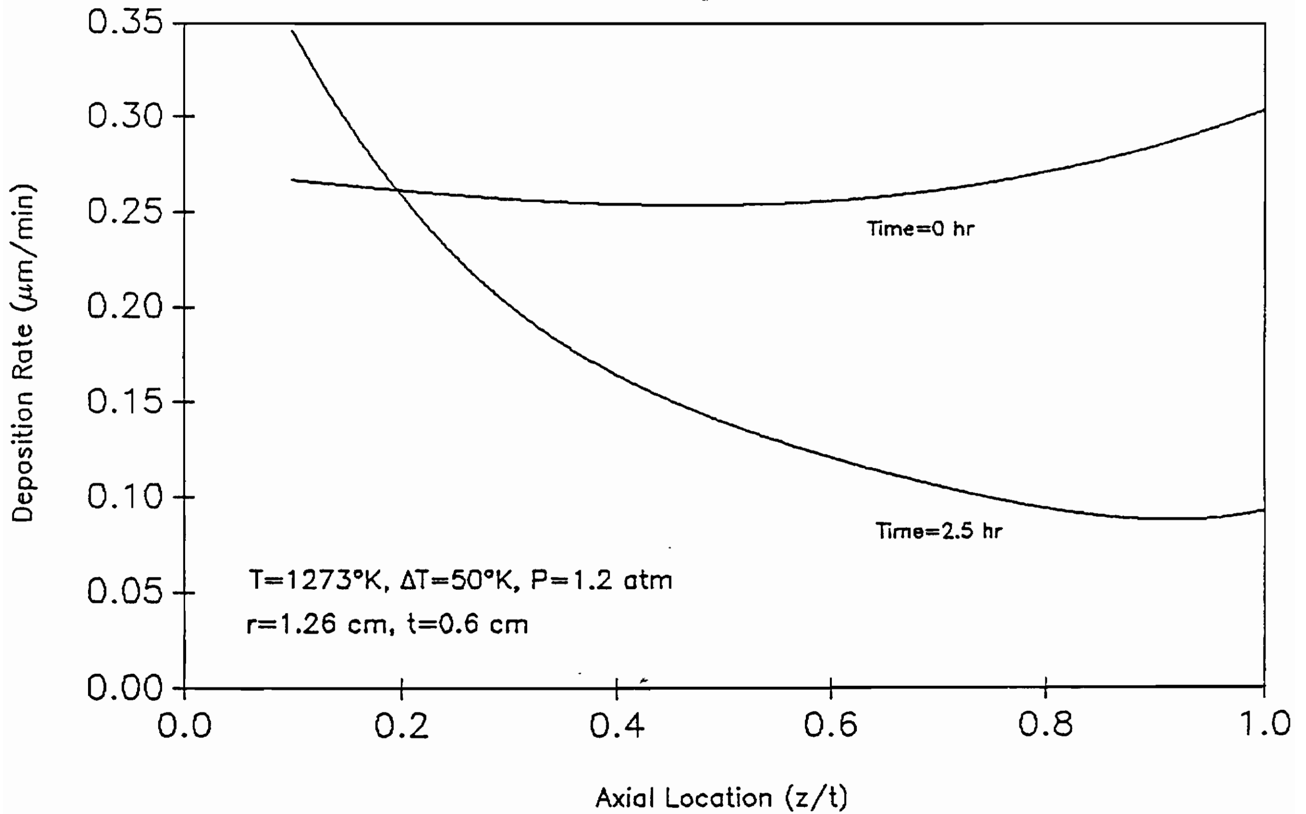


(a) $H_2$(Inlet) = 1.2 atm

Figure 5.3 Deposition Rate Profiles of a Circular Disk with Radius and Thickness being Equal to 1.26cm and 0.6cm. Experimental Conditions are: $T_{fu}$=1273° K, $\Delta$T=50° K, $H_2$(outlet)=1 atm

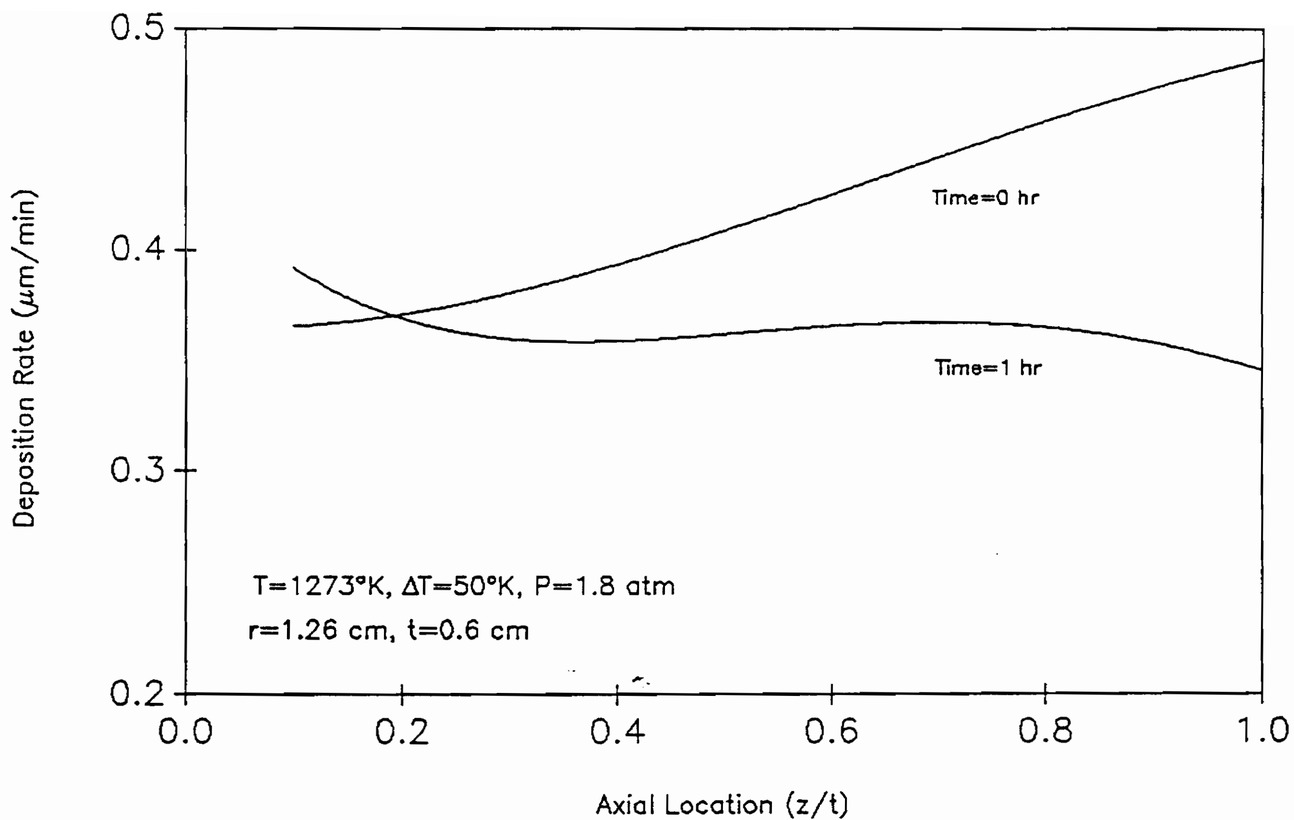


(b) $H_2$(Inlet) = 1.8 atm

Figure 5.3 Deposition Rate Profiles of a Circular Disk with Radius and Thickness being Equal to 1.26cm and 0.6cm. Experimental Conditions are: $T_{fu}=1273^\circ K$, $\Delta T=50^\circ K$, $H_2$(outlet)=1 atm

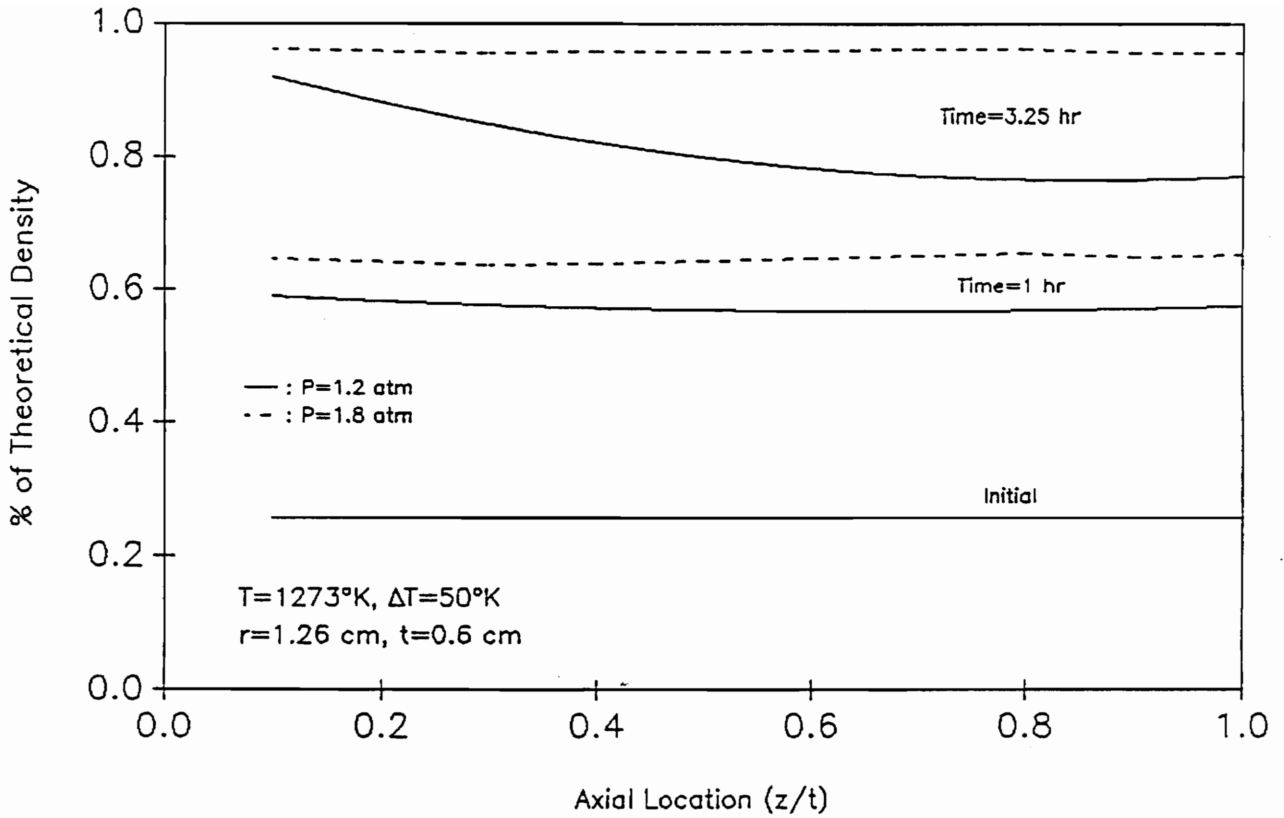


Figure 5.4 Improvements of the Resultant Density Profiles with the Use of the Forced–Flow Technique.
Radius and Thickness of the Disk are Equal to 1.26cm and 0.6cm

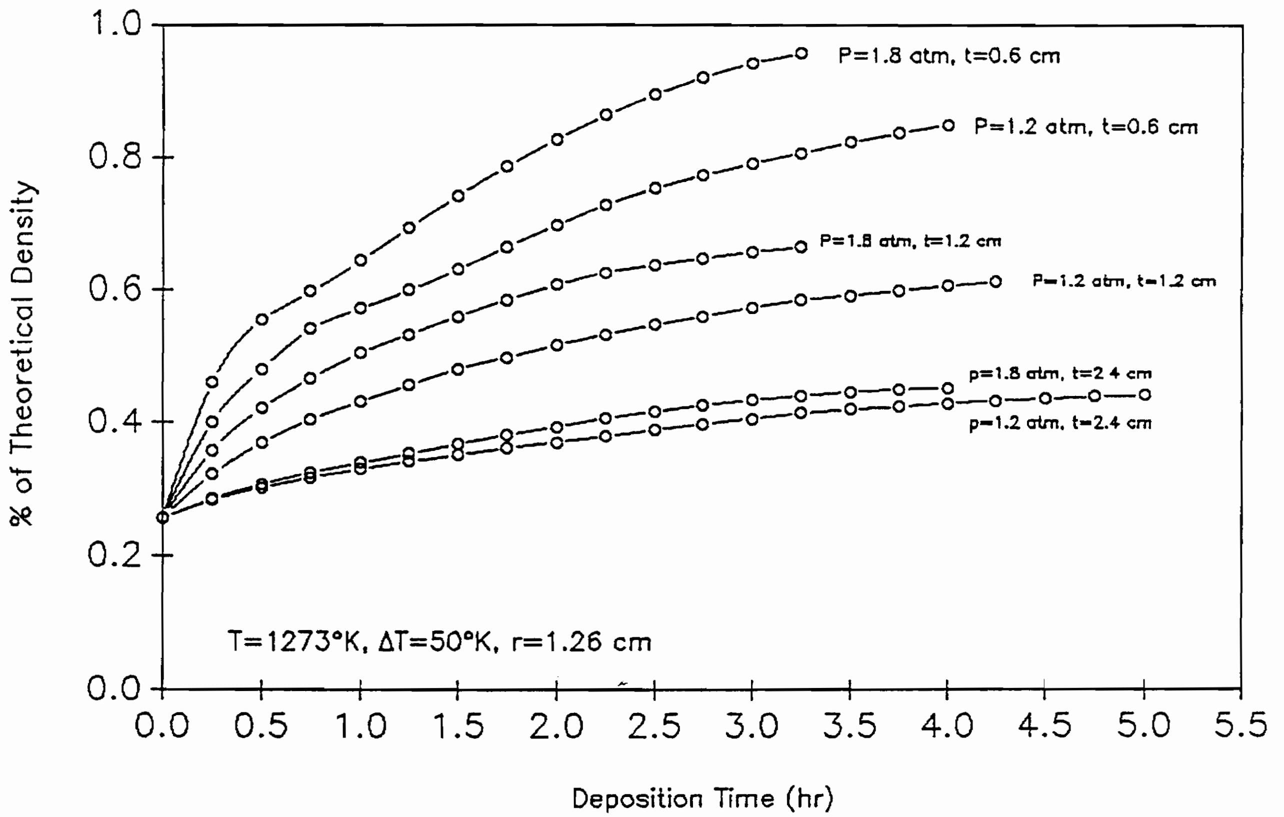


Figure 5.5 Changes of the Resultant Density Resulting from an Increase in the Disk Thickness

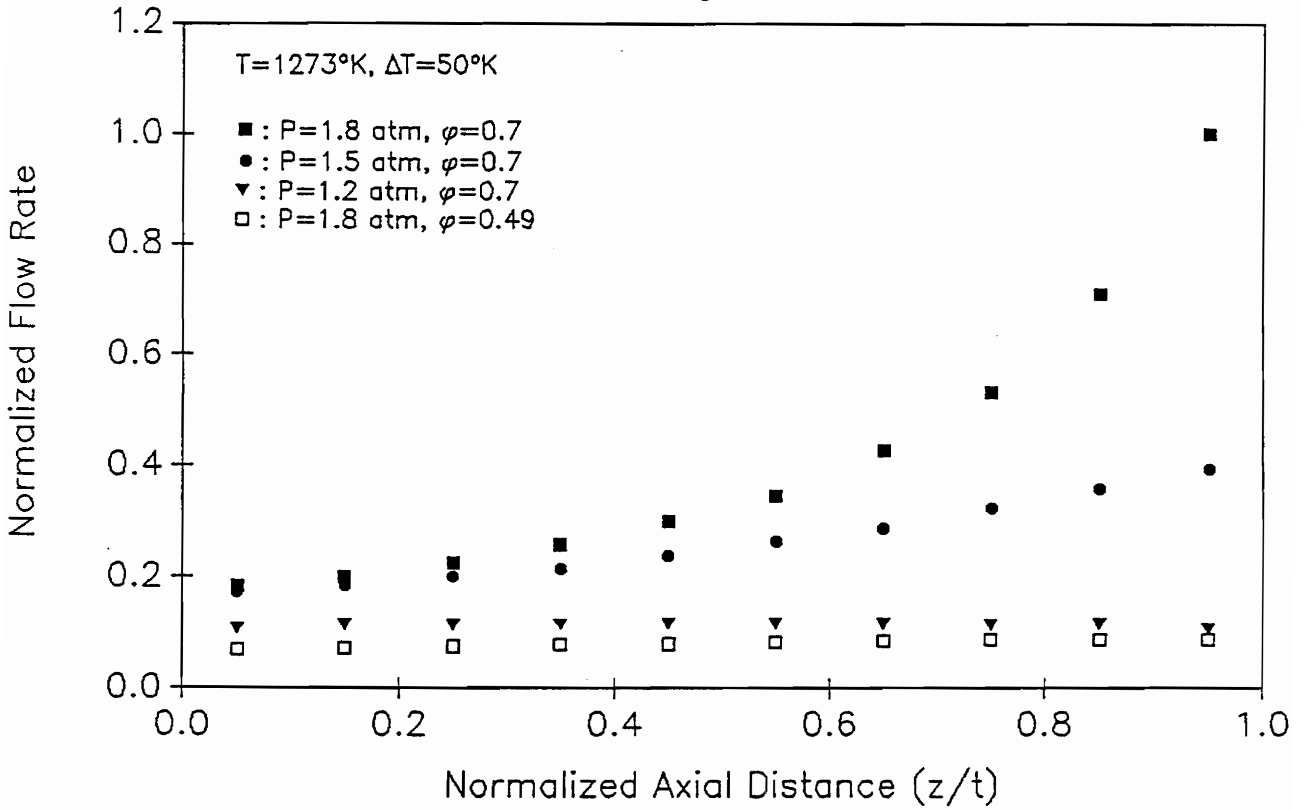


(a) $T_{fu}$ 1273° K, $\Delta T = 50°$ K

Figure 5.6 Calculated Gas flow Profiles for Various $\Delta P$ Values: $\Delta P$s are 0.2, 0.5 and 0.8 atm

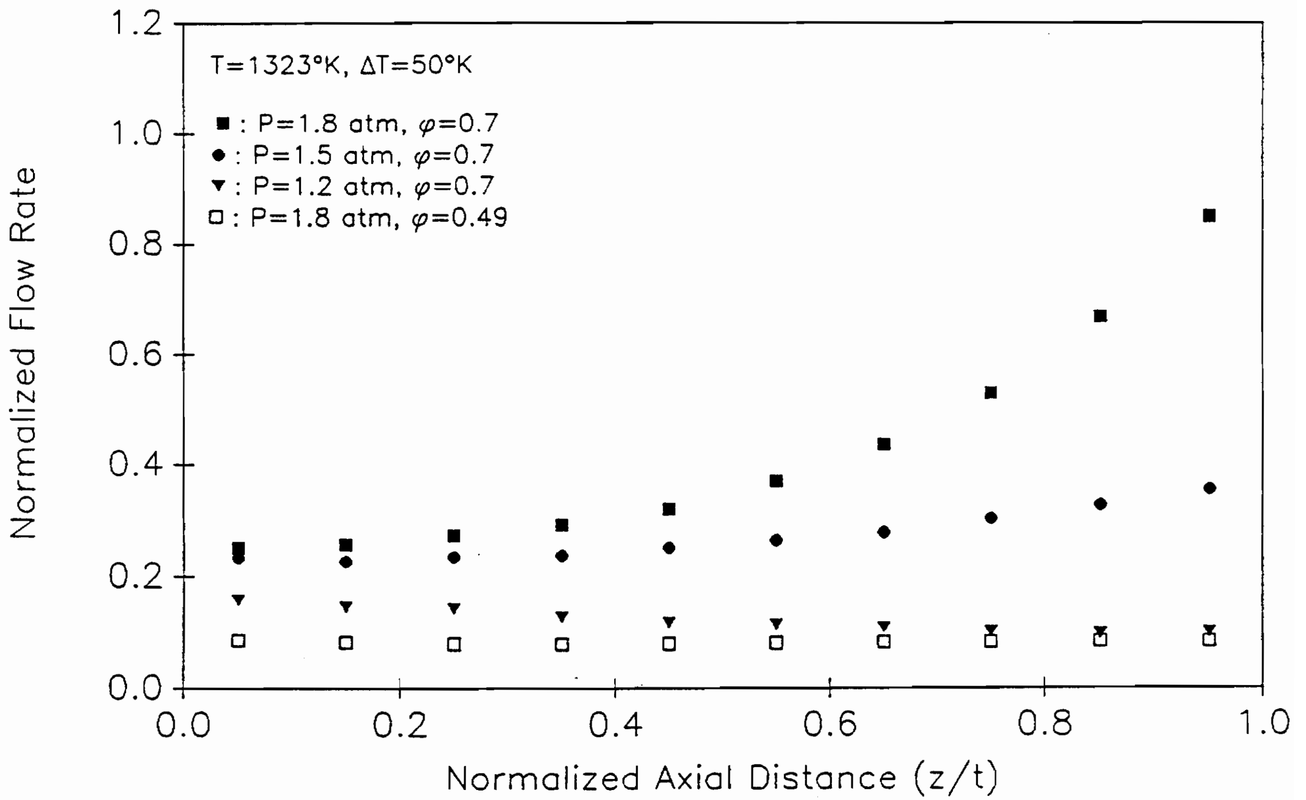


(b) $T_{fu}$ 1323° K, $\Delta T = 50°$ K

Figure 5.6 Calculated Gas flow Profiles for Various $\Delta P$ Values: $\Delta P$s are 0.2, 0.5 and 0.8 atm

As shown in Figure 5.6a, values of gas flow are almost doubled as the inlet $H_2$ pressure is increased from 1.2 atm to 1.5 atm with a 1273°K furnace temperature and 50°K temperature difference. As the inlet $H_2$ pressure is further increased to 1.8 atm, values of gas flow away from the entrance are increased significantly while values of gas flow near the entrance are almost invariant. This non–uniform effect of the gas flow can be attributed to the accumulation of gases near the entrance. As a result, improvements in the deposition rate profiles by increasing the inlet $H_2$ pressure could be reduced.

Gas flow profiles with same imposed $H_2$ pressure gradient but higher deposition temperatures are shown in Figure 5.6b. It can be seen that gas flow profiles are not sensitive to thermal profiles. In other words, gas flow profiles are dominated by the imposed $H_2$ pressure gradient, although changes resulting from chemical reactions also contribute to the induced forced–flow.

Also shown in Figures 5.6a and 5.6b are gas flow profiles with an initial porosity of 0.49 and an entrance $H_2$ pressure of 1.8 atm. As can be seen, with the same imposed pressure gradient, the induced gas flow is reduced significantly as the porosity of the composite is decreased. In order to maintain the same amount of gas flow to overcome the possible mass transfer limitations, the entrance $H_2$ pressure has to be increased during the process to compensate the decrease in the porosity.

However, with the entrance accumulation phenomenon mentioned above and possible limitations on the allowed inlet $H_2$ pressure to compensate for the gas flow loss due to permeability decreases, it might be necessary to reduce the deposition rates during the deposition process to prevent early pore blockage problems.

One obvious way to achieve this goal is to decrease the deposition temperature. Another alternative is to use the low pressure FCVI (LPFCVI) process. With a

possible large amount of $H_2$ gases accumulated near the entrance by using the APFCVI process, the deposition rate profiles near the entrance region could be improved through the use of LPFCVI processes. This can result in significantly improved deposition rate profiles, especially for the mass transfer limited FCVI processes, as shown in Figure 5.7 (with small specimen size and high deposition temperature) and Figure 5.8 (with large specimen size and low deposition temperature).

Figure 5.7 and Figure 5.8 show the deposition rate profiles with a disk thickness of 0.6 cm and 1.2 cm, respectively. In both cases, the FCVI processes are limited by the mass transfer with the entrance $H_2$ and MTS pressures being equal to 1.2 atm and 0.12 atm. Although the deposition rate profiles can be improved by increasing the $H_2$ entrance pressure to 1.8 atm, these deposition rate profiles with low deposition rate parameters $\omega_2$ are still not desirable for the densification process.

The MTS entrance pressure was changed from 0.12 atm to 0.024 atm to reduce the high deposition rates near the entrance. Two cases were studied of the FCVI processes with low inlet MTS pressure: one with a high $H_2$ entrance pressure (1.2 atm) and larger $H_2$ pressure difference (0.2 atm); and the other with a low $H_2$ entrance pressure (0.24 atm) and smaller $H_2$ pressure difference (0.04 atm). It can be seen in both Figure 5.7 and Figure 5.8 that the deposition rate profiles were much improved through the use of the LPFCVI process under these conditions.

The LPFCVI processes suffer from their low deposition rate, that is, resultant density profiles can be improved but at the expense of longer processing times. However, this major disadvantage can be overcome by using a higher deposition temperature or combining the APFCVI process with the LPFCVI process in the deposition process, as is discussed in the following section.

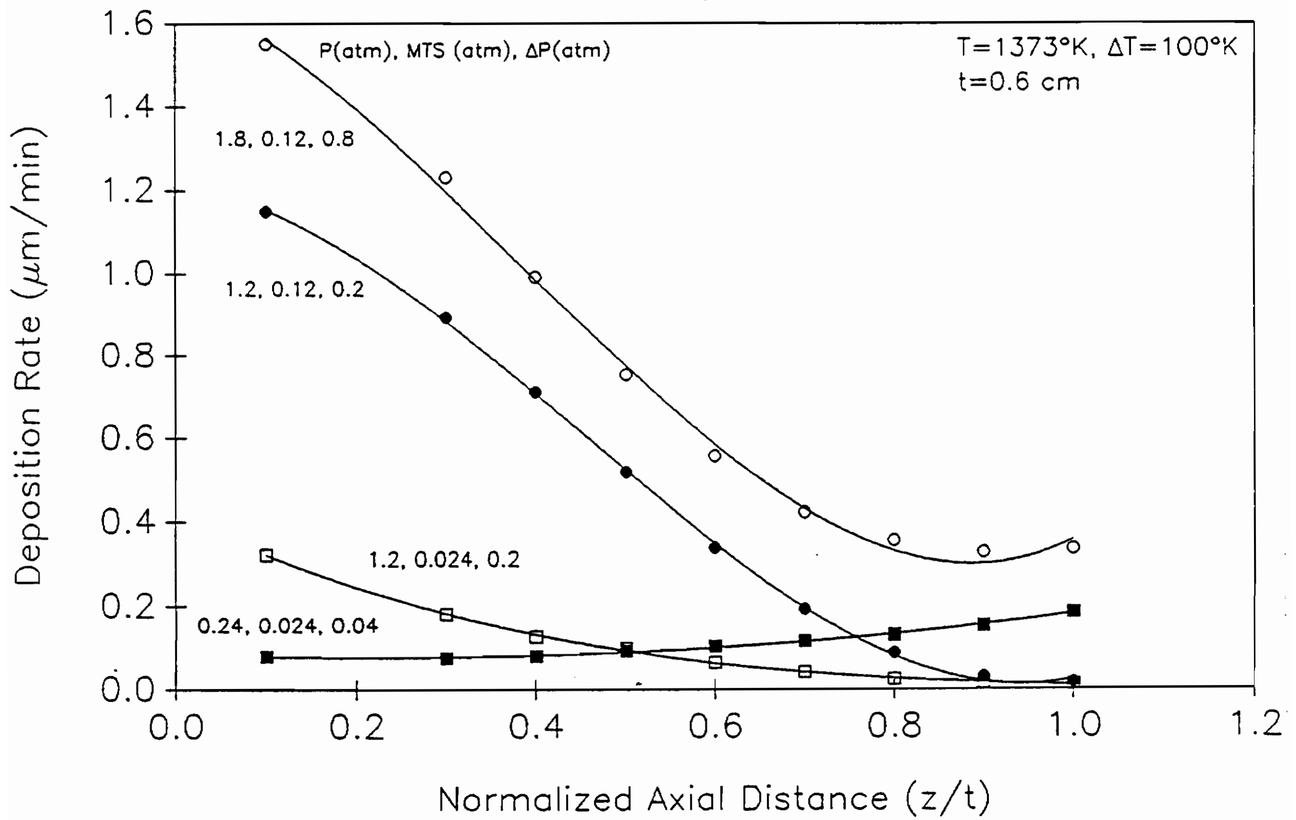


Figure 5.7 Comparisons of Deposition Rate Profiles

between APFCVI and LPFCVI Processes — $T_{fu}$=1373° K, ΔT=100° K, t=0.6cm

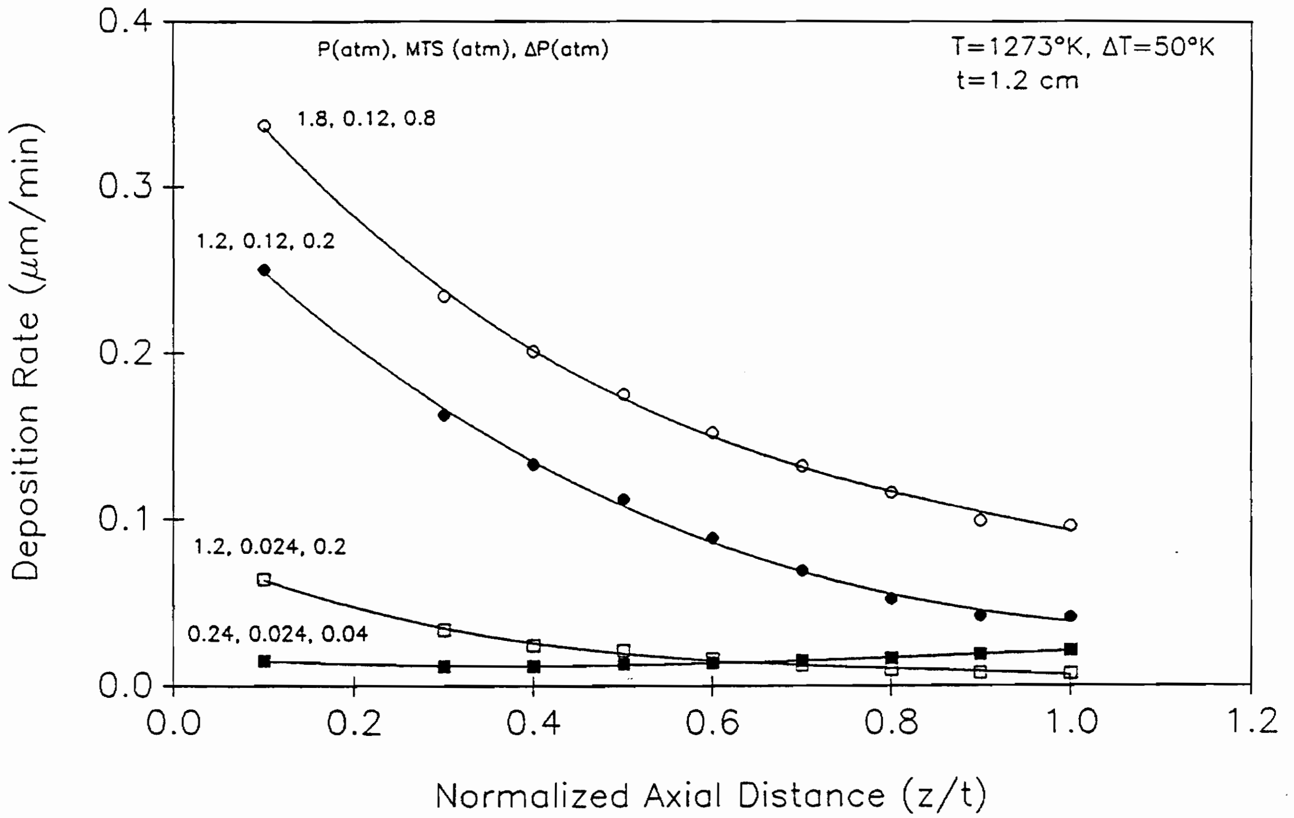


Figure 5.8 Comparisons of Deposition Rate Profiles

between APFCVI and LPFCVI Processes — $T_{fu}$=1273° K, ΔT=50° K, t=1.2cm

### 5.5.4 Optimization of the FCVI Process with Combinations of both APFCVI and LPFCVI Processes

As discussed previously, the APFCVI processes can significantly improve the deposition rate profiles with an appropriate choice of thermal profiles. However, the improved deposition rate profiles deteriorate rapidly as the medium permeability decreases because of the deposition of the matrix.

In order to prevent early pore blockage, especially for large size specimens, experimental conditions have to be changed during the FCVI process to adjust to these structural changes. For the LPFCVI process, the entrance accumulation effect can be avoided because of the low $H_2$ inlet pressure. Loss of the convection mass flux resulting from the pressure difference decrease could be compensated with an increase in the diffusion mass flux. As a result, the LPFCVI process can be used in the later stage of the FCVI processes to improve the overall deposition rate profiles.

With the combined use of APFCVI and LPFCVI processes, the balance between the processing time and product density profiles could be achieved, especially for the processing of large size specimens.

Various processing conditions, as listed in Table 5.1, were used to densify the disk with a thickness of 1.2 cm. Density profiles after the entrance was blocked and the time evolution of the total density are shown in Figure 5.9a and 5.9b.

With the use of only the APFCVI process, the density parameter $\omega_1$ was improved from 0.47 to 0.58 by adjusting the entrance $H_2$ pressure from 1.2 atm to 1.8 atm. The processing time was also shortened from 4.25 hours to 2.5 hours.

If the APFCVI process was followed by the LPFCVI process after 60 minutes

of processing, the resultant density profile, especially for those portions away from the entrance, improved significantly compared to that of the APFCVI process. The total processing time of this combined process is 9 hours.

On the other hand, although the final density profile is much more uniform, the total processing time of the LPFCVI process alone is as long as 14 hours.

As the disk thickness was increased to 2.4 cm, a lower thermal profile had to be used with the forced–flow technique to provide a desirable deposition rate profile. As shown in Figure 5.10a, the APFCVI process with a 1223°K furnace temperature, 50°K temperature difference, 1.8 atm entrance $H_2$ pressure, and 0.8 atm $H_2$ pressure difference, was used to densify the disk. The initial deposition rate parameter $\omega_2$ of this chosen APFCVI process was 0.63.

The FCVI processes used to densify the disk with a 2.4 cm thickness are listed in Table 5.2. Profiles of the composite density after the entrance was blocked and the time evolution of the total density are shown in Figures 5.10b and 5.10c. As shown in Figure 5.10c and Table 5.2, although a high composite density could be obtained by using the LPFCVI process alone, this process suffers from long processing time.

On the other hand, although the processing time is much shorter than other processes, the density profile that can be achieved by using the APFCVI process alone is not satisfactory, as shown in Figures 5.10b and 5.10c.

With the combined use of APFCVI and LPFCVI processes, a balance between processing time and final density profile can be achieved. For example, if the APFCVI process is followed by the LPFCVI process after 5.5 hours of deposition, the final density parameter $\omega_1$ can be improved from 0.63 of the APFCVI process alone to 0.76, with a reasonably high composite density of 0.77. The corresponding

processing time is 41.5 hours, which is about 58% of the processing time of the LPFCVI process.

## 5.6 Summary

A mathematical model utilizing the finite element method was proposed to study the FCVI process of silicon carbide using methyltrichlorosilane and hydrogen precursors. Density profiles of circular disks with radii of 1.26 cm and thicknesses of 0.6 cm, 1.2 cm and 2.4 cm were analyzed for various experimental conditions.

Deposition rates near the entrance were found to increase during the FCVI process as a result of the increased residence time of the vapor species. This phenomenon, which could not be predicted without the consideration of gas phase reactions, could result in unacceptable density profiles.

A conceptual multi–step FCVI process was proposed to obtain acceptable final density profiles within reasonable processing times. This multi–step FCVI process involved deposition under ambient–pressure to improve the density profiles and shorten the processing times. This was followed by the LPFCVI process to overcome the mass transfer limitations caused by the entrance accumulation effect and possible limitations on the equipment of the APFCVI process.

The balance between the processing time and final density profile could be achieved with the use of this multi–step FCVI process. Advantages of this multi–step FCVI process were demonstrated by studying the densification process in large size specimens.

Table 5.1 Parameters of the FCVI processes Used in Figures 5.9a and 5.9b

| PROCESS | $\omega_1$ | TIME (HR) | DESCRIPTION |
|---|---|---|---|
| APFCVI (1) | 0.47 | 4.25 | P=1.2, MTS=0.12, $\Delta$P=0.2<br>T=1273, $\Delta$T=50 |
| APFCVI (2) | 0.58 | 2.50 | P=1.8, MTS=0.18, $\Delta$P=0.8<br>T=1273, $\Delta$T=50 |
| APFCVI + LPFCVI (1) | 0.67 | 9.00 | {P=1.8, MTS=0.18, $\Delta$P=0.8, T=1273, $\Delta$T=50 (60 min.)} and {P=0.36, MTS=0.072, $\Delta$P=0.06, T=1323, $\Delta$T=100 (480 min.)} |
| APFCVI + LPFCVI (2) | 0.75 | 11.50 | {P=1.8, MTS=0.18, $\Delta$P=0.8, T=1273, $\Delta$T=50 (30 min.)} and {P=0.36, MTS=0.072, $\Delta$P=0.06, T=1323, $\Delta$T=100 (660 min.)} |
| LPFCVI(1) | 0.82 | 14.00 | P=0.36, MTS=0.072, $\Delta$P=0.06<br>T=1323, $\Delta$T=100 |

with: P, MTS and $\Delta$P in (atm); T and $\Delta$T in ($^\circ$K)

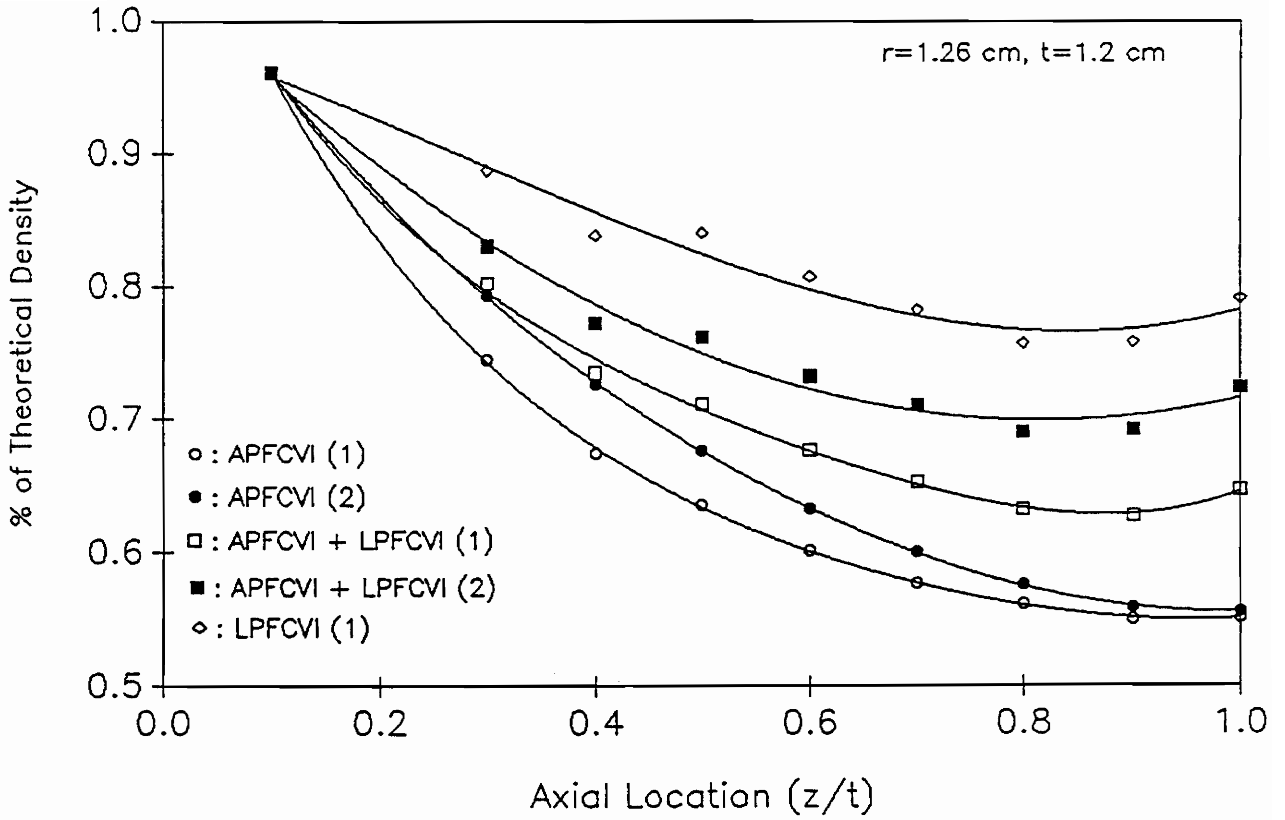


Figure 5.9a Final Density Profiles of the Disk with Radius and Thickness being Equal to 1.26cm and 1.2cm.

The Processing Conditions are Listed in Table 5.1

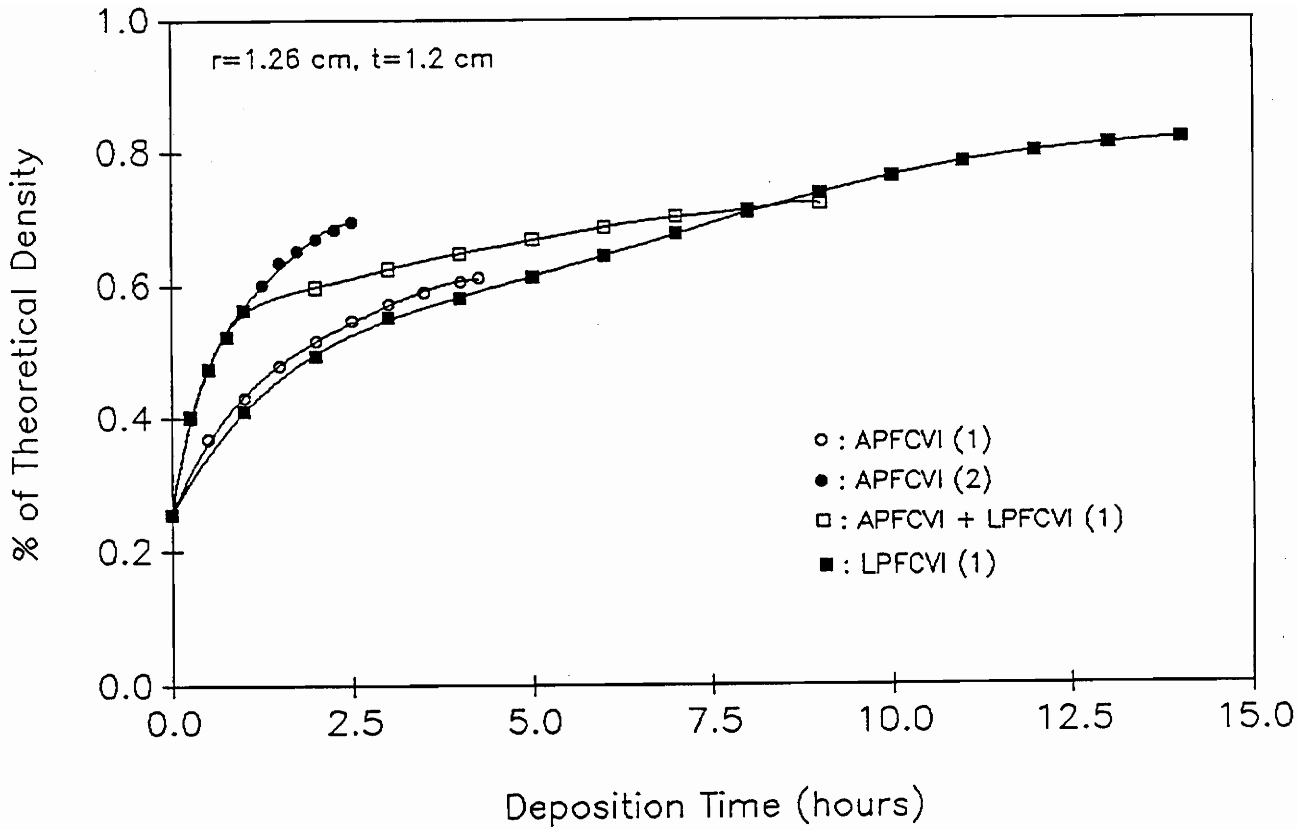


Figure 5.9b The Time Evolution of the Total Density of the Disk with Radius and Thickness being Equal to 1.26cm and 1.2cm. The Processing Conditions are Listed in Table 5.1

Table 5.2 Parameters of the FCVI processes Used in Figures (5.10a–5.10c)

| PROCESS | $\omega_1$ | TIME (HR) | DESCRIPTION |
|---|---|---|---|
| APFCVI (1) | 0.63 | 12.00 | P=1.8, MTS=0.18, ΔP=0.8<br>T=1223, ΔT=50 |
| APFCVI +<br>LPFCVI (1) | 0.70 | 34.00 | {P=1.8, MTS=0.18, ΔP=0.8, T=1223, ΔT=50 (420 min.)} and {P=0.36, MTS=0.072, ΔP=0.06, T=1273, ΔT=100 (1620 min.)} |
| APFCVI +<br>LPFCVI (2) | 0.76 | 41.50 | {P=1.8, MTS=0.18, ΔP=0.8, T=1223, ΔT=50 (330 min.)} and {P=0.36, MTS=0.072, ΔP=0.06, T=1273, ΔT=100 (2160 min.)} |
| APFCVI +<br>LPFCVI (3) | 0.81 | 50.50 | {P=1.8, MTS=0.18, ΔP=0.8, T=1223, ΔT=50 (240 min.)} and {P=0.36, MTS=0.072, ΔP=0.06, T=1273, ΔT=100 (2790 min.)} |
| LPFCVI (1) | 0.88 | 72.00 | P=0.36, MTS=0.072, ΔP=0.06<br>T=1273, ΔT=100 |

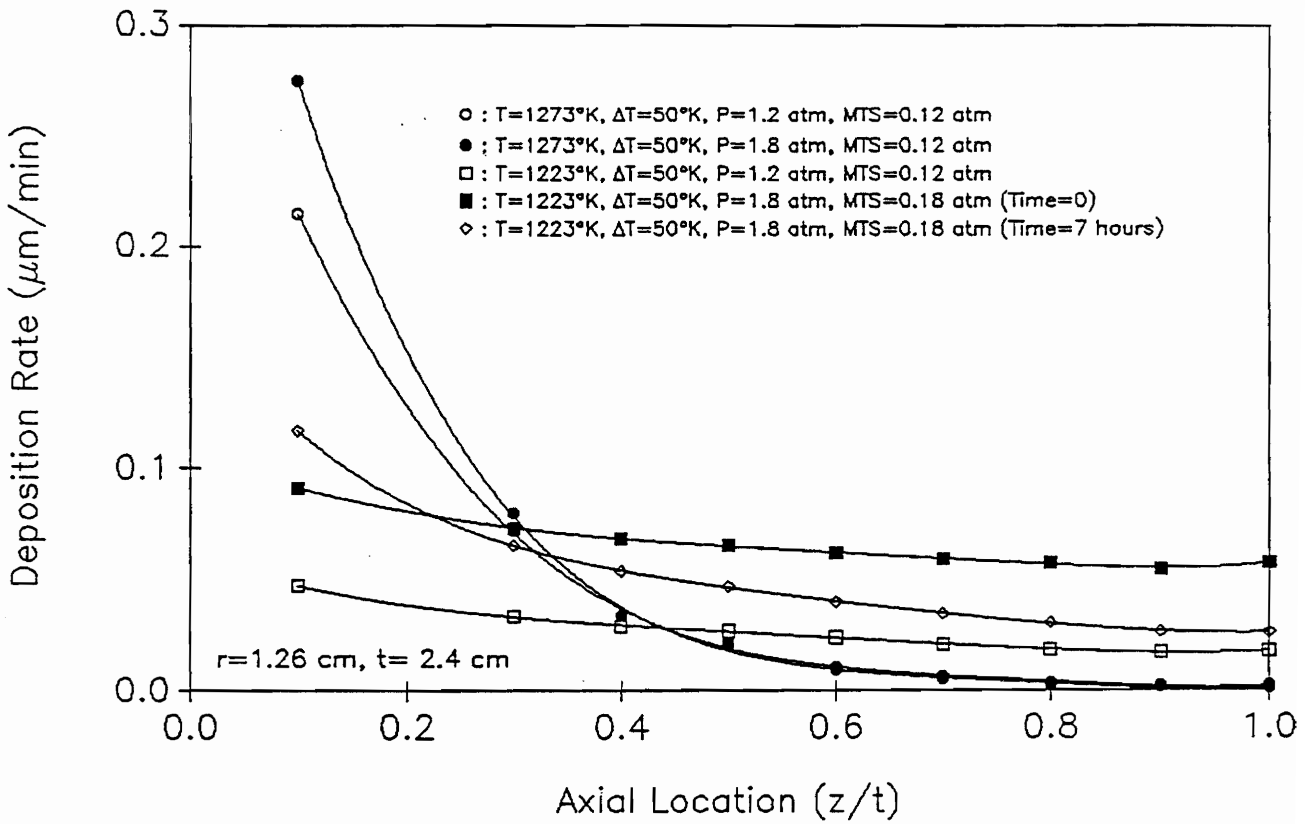


Figure 5.10a Deposition Rate Profiles for the Disk with Radius and Thickness being Equal to 1.26cm and 2.4cm

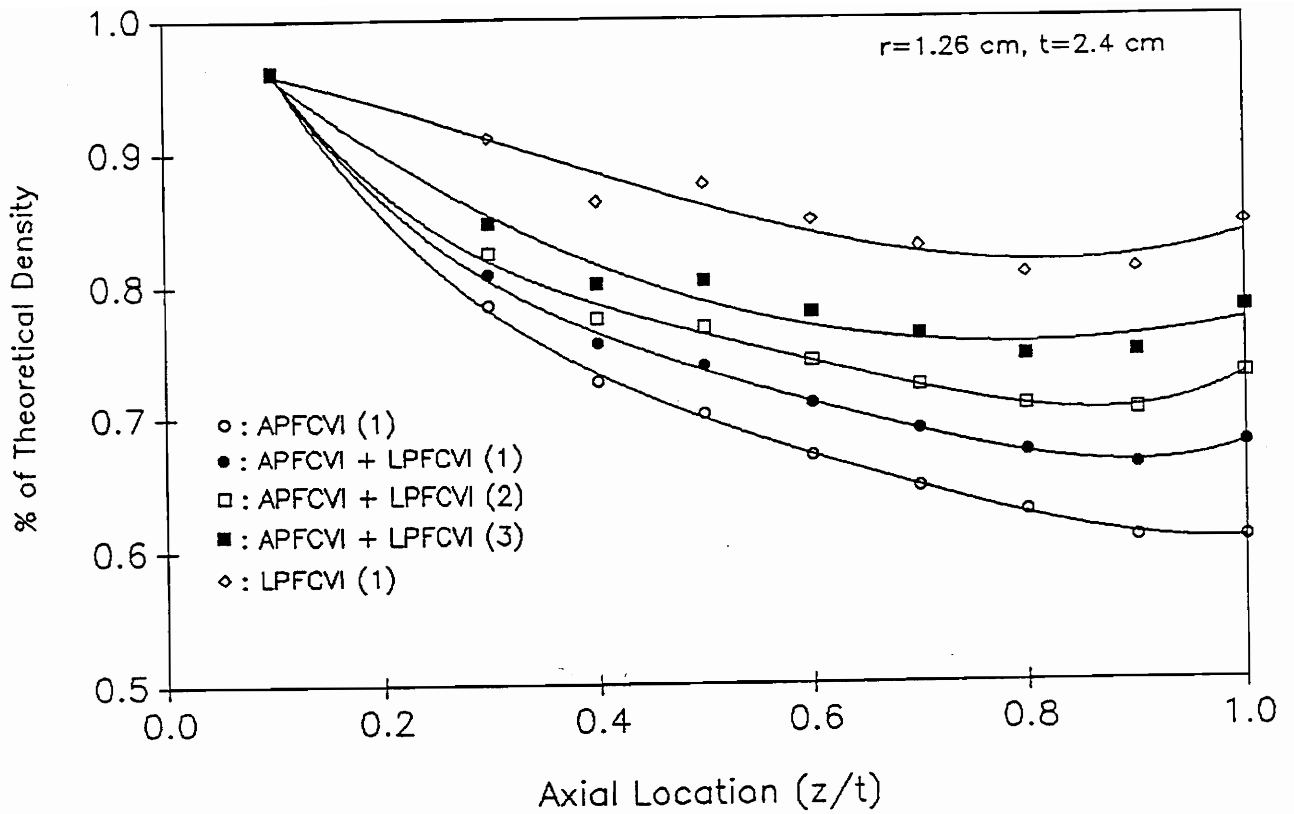


Figure 5.10b Final Density Profiles of the Disk with Radius and Thickness being Equal to 1.26cm and 2.4cm.

The Processing Conditions are Listed in Table 5.2

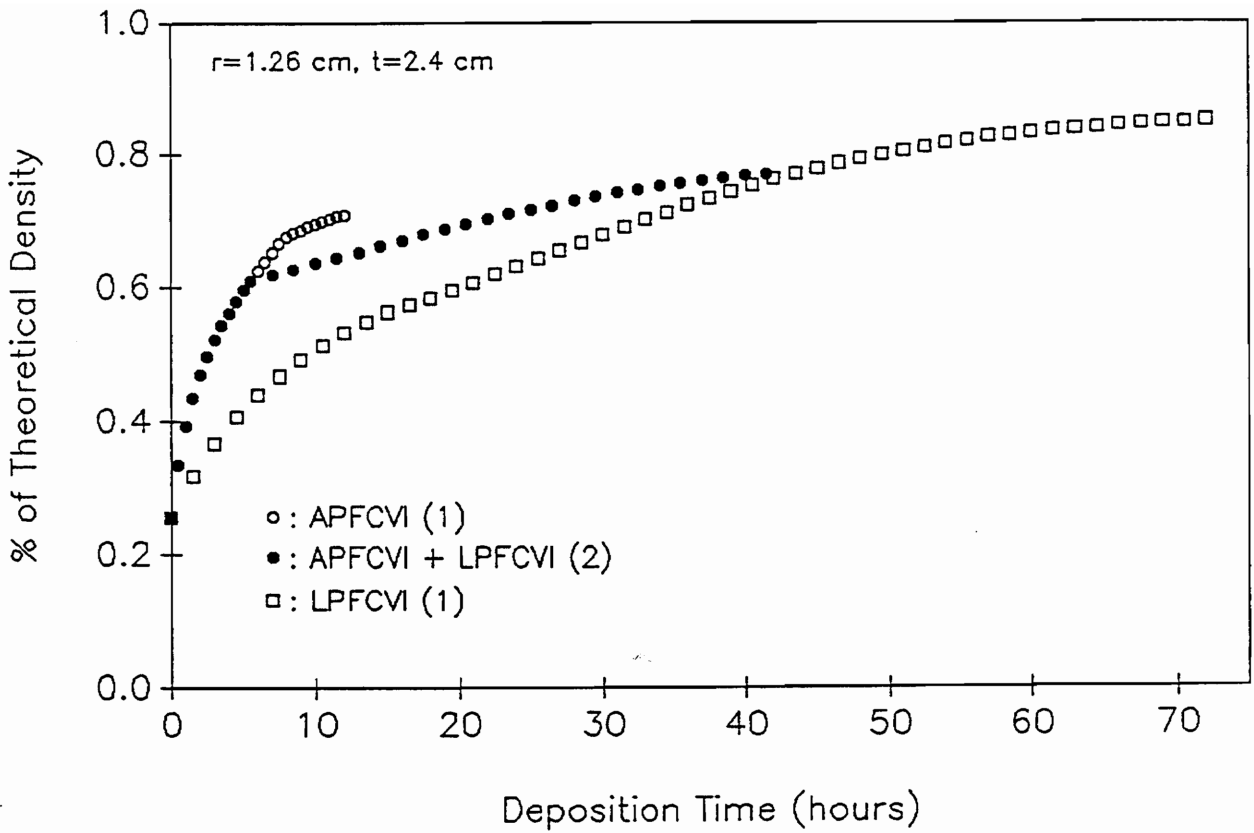


Figure 5.10c The Time Evolution of the Total Density of the Disk with Radius and Thickness being Equal to 1.26cm and 2.4cm. The Processing Conditions are Listed in Table 5.2

# Chapter 6
# Summary and Conclusions

A systematic study on the FCVI process leads to the following summary and conclusions:

(1). The step coverage test has the advantage of studying the film or matrix conformality experimentally during the deposition process because of its simple geometry and similar dimensional sizes compared to voids within the fibrous preform.

Agreements between the experimental step coverage data and the calculations based on the 2–D continuum–like step coverage model were found to be good for $SiO_2$ films deposited from $SiH_4/H_2$ precursors. This continuum–like modeling approach can be applied to study the film conformality for other CVD systems.

Evolutions of the CVD film conformality during the deposition process were also studied. The BEM technique was used to implement the 2–D continuum–like step coverage model, which incorporates the effect of the moving deposition fronts. The CVD film conformality was found to deteriorate at the later stage of the step coverage process resulting from closing of the trench opening.

This transient analysis of the step coverage process suggests that for the FCVI process the experimental conditions would have to change during the deposition process to prevent early stage pore blockage problem.

(2). The feasibility of using the forced–flow technique to improve the deposition rate profiles of the FCVI process was investigated based on the simple flux model which incorporates both the gas phase and surface reactions.

The local pressure gradient, resulting from both gaseous pressure changes due to chemical reactions and imposed inert gas pressure gradient, was used to calculate the local forced–flow based on Darcy's law.

In addition to being dependent on the permeability of the porous medium, the effectiveness of the forced–flow technique was found to be strongly dependent on the controlling step of the FCVI process.

In other words, for the surface reaction controlled FCVI processes, the use of forced–flow can improve the deposition rate profiles, and result in lower residual porosity. On the other hand, for the gas–phase reaction controlled FCVI processes, the deposition rate profiles deteriorate with an increase in the forced–flow rate.

The controlling step of the FCVI processes may shift resulting from changes of the deposition temperature profiles. Changes in the deposition temperature profiles can be caused by the imposed thermal gradient between the entrance and exit sides, and changes of the permeability and thermal conductivity of the composite medium due to the matrix depositions.

Therefore, it is very important to consider explicitly the individual reactions, that is, the gas–phase and surface reactions, in order to predict the optimal conditions of the FCVI process, such as thermal profiles and the forced–flow magnitude, through the modeling calculations.

(3). Kinetic data of silicon carbide deposition from MTS/$H_2$ precursors were obtained by analyzing our own deposition rate data as well as reported results. The SiC deposition process was modeled using the following reactions — (1) : gas phase decomposition of MTS molecules into two major intermediates one containing silicon and the other containing carbon; (2) : adsorption of the intermediates onto the surface sites of the growing film; (3) : reaction of the adsorbed intermediates to form silicon carbide.

A FEM model, which incorporates the kinetics and transport process of the gaseous species, was developed to analyze the hot–wall SiC CVD process. The equilibrium constant for the gas phase decomposition process was divided into the forward and backward reaction constants as 2.0E+25 exp[(–448.2 kJ/mol)/RT] and 1.1E+32 exp[(–416.2 kJ/mol)/RT], respectively. Equilibrium constants for the surface adsorption reactions of silicon–carrying and carbon–carrying intermediates are 0.5E+11 exp[(–21.6 kJ/mol)/RT] and 7.1E+09 exp[(–33.1 kJ/mol)/RT], while the rate constant for the surface reaction of the intermediates is 4.6E+05 exp[(–265.1 kJ/mol)/RT].

Experimental data on the hot–wall SiC CVD process with respect to the variance of system pressure and temperature were in good agreement with the modeling predictions. Changes in the effective activation energy and reaction order of the deposition process can be attributed to the consumption of gas species on the hot reactor walls. With the incorporation of both gas–phase and surface reactions of the SiC CVD process, this kinetic model is more suitable for analyzing the deposition rate profiles in the FCVI processes than the conventional lumped first order kinetic model.

(4). Density profiles of a circular SiC disk with radius of 1.26 cm and thicknesses of 0.6 cm, 1.2 cm and 2.4 cm were analyzed using the FEM FCVI model under various experimental conditions.

Although the final density profile of the SiC disk with a thickness of 0.6 cm can be improved tremendously with an increase in the $H_2$ inlet pressure from 1.2 atm to 1.8 atm, this improvement is diminished as the disk thickness is increased to 1.2 cm and 2.4 cm. Further increases in the inlet $H_2$ pressure to improve the density profile of large size specimens are not suggested because of the limitations associated with the equipments and the accumulation of gaseous species near the entrance side. This accumulation phenomenon may prove to be detrimental to the deposition rate profiles depending on the balance between the gaseous species transferred by the diffusion and convection mechanisms.

A conceptual multi–step FCVI process was proposed to obtain good final density profiles within reasonable processing times. The balance between the processing time and final density profile could be achieved through the use of this multi–step FCVI process. Advantages of this multi–step FCVI process were demonstrated by studying the densification process in large size specimens.

# Appendix A
# Estimations of the Structural and Transport Properties

## A.1 Accessible Porosity

Based on the percolation theory [18–22], it was found that for media with high porosity, the accessible porosity ($\phi_a$) is nearly identical to the overall porosity ($\phi$). However, as the overall porosity decreases due to the deposition process, the accessible porosity starts to deviate from the overall porosity due to the occurrence of trapped pores. These deviations are dependent on the geometry of the porous medium.

Reported data [20–22] on accessible porosity for fibrous preform with different packing geometry, that is, 1–D, 2–D or 3–D microstructure, were fitted to polynomial expressions to be used in the FEM FCVI program:

For $\phi < \phi_p$

$$\phi_a = \text{Accessible Porosity} = 0 \tag{A.1.1}$$

For $\phi_p < \phi < \phi_1$

$$\phi_a\,(1\text{–D},\perp) = -18.995 + 102.03\phi - 134.33\phi^2 \tag{A.1.2.a}$$

$$\phi_a\,(2\text{–D}) = -1.182 + 16.138\phi - 48.481\phi^2 \tag{A.1.2.b}$$

$$\phi_a\,(3\text{–D}) = -0.1626 + 5.724\phi - 34.059\phi^2 \tag{A.1.2.c}$$

For $\phi > \phi_1$

$$\phi_a = \phi \tag{A.1.3}$$

Values of the parameter $\phi_1$ of different fibrous structures are : 0.39 (1–D,⊥), 0.1675 (2–D), and 0.075 (3–D). Values of the corresponding percolation porosity $\phi_p$ are given in Table A.1.

Table A.1 Parameters Used to Estimate the Bulk and Knudsen Diffusion Constants within Structures of Randomly Overlapping Fibers [20–22]

| Fibrous Structures & Diffusional Flow Direction | Knudsen | | | Bulk |
|---|---|---|---|---|
| | $\phi_p$ | $\eta_{min}$ | $\alpha$ | $\alpha$ |
| 1–D Parallel (∥) | 0 | 0.549 | 0 | 0 |
| 1–D Perpendicular (⊥) | 0.33 | 1.747 | 1.099 | 0.707 |
| 2–D Parallel (∥) | 0.11 | 1.149 | 0.954 | 0.521 |
| 2–D Perpendicular (⊥) | 0.11 | 1.780 | 1.055 | 0.785 |
| 3–D All Directions | 0.037 | 13/9 | 0.921 | 0.661 |

## A.2 Permeability

Gebart [77] derived the permeability of the uni–directional fiber bundle with both quadratic and hexagonal packing geometries. The permeability expression for

flow transverse to the fibers was found to be different from the famous Kozeny–Carman form [77]. On the other hand, the permeability expression for flow along the fibers is the same as the Kozeny–Carman form:

$$B_{\parallel} = \frac{8R_f^2}{c_1}\frac{\phi_a^3}{(1-\phi_a)^2} \tag{A.2.1a}$$

$$B_{\perp} = c_2 R_f^2\left(\sqrt{V_{fmax}/(1-\phi_a)} - 1\right)^{2.5} \tag{A.2.1b}$$

where $R_f$ is the fiber radius ($\mu$m), and additional parameters are given in Table A.2.

Table A.2 Constants $c_1$, $c_2$ and $V_{fmax}$ Used to Calculate the Permeability of a Uni–Directional Fiber Bundle [77]

| Fiber Arrangement | $c_1$ | $c_2$ | $V_{fmax}$ ($V = 1-\phi$) |
|---|---|---|---|
| Quadratic | 57 | $\frac{16}{9\pi\sqrt{2}}$ | $\pi/4$ |
| Hexagonal | 53 | $\frac{16}{9\pi\sqrt{6}}$ | $\frac{\pi}{2\sqrt{3}}$ |

The permeability along the fibers is about one order of magnitude larger than the permeability perpendicular to the fibers.

For fibrous preforms with 2–D or 3–D microstructure, the following empirical expression was used [78]:

$$B\,(\parallel,\perp) = 0.515\phi_a R_f^2 \ln(0.64/(1-\phi_a)^2)/(1-\phi_a) \tag{A.2.2}$$

A.3 Reaction Area Per Unit Volume

For the medium with randomly overlapping fibers, the internal reaction area per unit volume is given as [20–22]:

$$S_v\ (\mu m^{-1}) = -2\phi_a \ln\phi_a / R_f \qquad (A.3.1)$$

A.4 Thermal Conductivity

Because both vapor species and ceramic composites provide the heat conduction paths, the so–called rule–of–mixtures relationship was used to estimate the thermal conductivity of the fibrous medium with the 2–D or 3–D microstructure:

$$K\ (\text{watt/cm–°K}) = K_f(1-\phi) + K_g\phi \qquad (A.4.1)$$

where $K_f$ and $K_g$ are the thermal conductivity of the vapor species and ceramic composite respectively.

Equation (A.4.1) is also applied to the thermal conduction flow along the fibers of the 1–D fiber bundles. For the condition of thermal conduction flow perpendicular to the fibers of the 1–D fiber bundles, the Lewis and Nielsen semi–theoretical expression [80] was used:

$$K_{\perp} = K_g\left(\frac{1+0.5\,b(1-\phi)}{1-b\Psi(1-\phi)}\right) \qquad (A.4.2)$$

$$\text{with } b = (K_f/K_g-1)/(K_f/K_g+0.5);\ \Psi = 1+0.268(1-\phi)$$

## A.5 Effective Diffusion Coefficients inside the Porous Medium

Estimations of the diffusion coefficients, including both Knudsen and ordinary diffusion coefficients, are given in equation (A.5.4). The overall effective diffusion constant can be computed based on the Bosanquet formula [25]:

$$D_{eff}^{-1} = D_{ik}(eff)^{-1} + D_{ij}(eff)^{-1} \qquad \text{(A.5.1)}$$

The ordinary or bulk diffusion constant for binary gaseous mixtures (i and j), which depends on the mean free path of the diffusing molecules, can be expressed as [26]:

Equation (A.5.2)

$$D_{ij}\ (cm^2/sec) = 0.0018583\sqrt{T^3(^\circ K)(M_i^{-1}+M_j^{-1})}/(p(atm)\sigma_{ij}^2\Omega_{ij})$$

where $M_i$ (gm/mol) is the molecular weight of the gas component i, $\sigma_{ij}$ (Å) is the Lennard–Jones parameter, and $\Omega_{ij}$ is a dimensionless function of the temperature and the intermolecular potential field.

On the other hand, the Knudsen diffusion constant of the species i, which depends on the medium geometry, can be estimated from [27]:

$$D_{ik}\ (cm^2/sec) = 0.97R_{eq}(\mu m)\sqrt{T(^\circ K)/M_i} \qquad \text{(A.5.3)}$$

where $R_{eq}$ is the equivalent pore radius of the medium, which is equal to $-R_f/\ln\phi_a$ for randomly overlapping fibrous structures.

For the fluid transport phenomena within the porous medium, the network structure of the porous medium has to be considered in order to predict the effective mass diffusivity of the gases inside the fibrous medium.

Based on the Monte Carlo simulation study of the gas diffusivities in structures of randomly overlapping fibers [20–22], the effective diffusion coefficient within the porous medium can be expressed as:

$$D_{ik}(\text{eff}) = \phi_a D_{ik}/\eta_{ik},\ D_{ij}(\text{eff}) = \phi_a D_{ij}/\eta_{ij} \tag{A.5.4}$$

where $\eta$ is the tortuosity factor of the porous medium, which can be obtained from the following expression:

$$\eta = \eta_{min} \left\{(1-\phi_p)/(\phi-\phi_p)\right\}^{\alpha} \tag{A.5.5}$$

Estimations of the tortuosity factor of the fibrous medium with different microstructure are listed in Table A.1.

It should be noted that values of $\alpha$ in Table A.1 for ordinary diffusion in the 3–D structure or parallel to the fiber mat of the 2–D structure are valid when values of $\phi$ are larger than 0.4. For the low porosity regime, the following equation should be used:

$$\eta = \eta_{min} \left\{(0.4-\phi_p)/(\phi-\phi_p)\right\}^{\alpha} \tag{A.5.6}$$

where the parameter $\alpha$ is equal to 0.872 and 0.965 for the 2–D and 3–D structures, respectively. The parameter $\eta_{min}$ can be computed from equation (A.5.5) and Table A.1.

# Appendix B
## Solving the Conduction–Convection Equation

The application of FEM in solving the conduction–convection equation, as shown in equation (B.1), has been the subject of intensive studies for the past [83–86]. It was found that the convection term may introduce undesirable numerical oscillations, which does not exist in the pure conduction equation.

$$-K\frac{d^2T}{dx^2} + U\frac{dT}{dx} = 0 \qquad \text{(B.1)}$$

Basically, there are two approaches to obtain stable finite element solutions of the conduction–convection equation with high values of convection term, that is, the upwinding finite element method (UWFEM) [84] and the conventional Galerkin–based finite element method with refined meshes (GFEM) [86].

Another technique which is based on the canonical form of the conduction–convection equation was developed by Guymon et al. [83]. This technique, written here as the canonical finite element method (CFEM), however, has not received a lot of attention in comparison to the other two techniques mentioned above.

The UWFEM technique is based on the Petrov–Galerkin finite element method. Unlike the Galerkin finite element method, in which the shape and weighting functions are identical, shape functions and weighting functions are

chosen differently in the Petrov–Galerkin finite element method.

For example, the shape functions, $\Psi_1$ and $\Psi_2$, of the 1–D linear element can be expressed as [43,84]:

$$\Psi_1(\xi) = 0.5(1-\xi)\ ,\ \Psi_2(\xi) = 0.5(1+\xi)$$

The corresponding weighting functions, $\psi_1$ and $\psi_2$, of the Petrov–Galerkin finite element method are given as [84]:

$$\psi_1(\xi) = \Psi_1(\xi) - \alpha F(\xi),\ \psi_2(\xi) = \Psi_2(\xi) + \alpha F(\xi)$$

where the function $F(\xi)$ is the modifying function, which is equal to $0.75(1-\xi)(1+\xi)$, and $\alpha$, called the upwinding parameter, is a problem–dependent coefficient.

The canonical finite element method is based on the canonical form of equation (B.1):

$$-K\frac{d}{dx}(H\frac{dT}{dx}) = 0, \text{ with } H = \exp\{-\int(U/K)dx)\} \qquad \text{(B.2)}$$

Numerical results of the conduction–convection equation based on these three finite element methods are presented in Tables B.1a–B.1c. For the conduction–convection equation with a low peclet number, all the three methods provide good results, as shown in Table B.1a, with the use of just 10 linear elements.

As the peclet number is increased to 50, the number of elements have to be increased from 10 to 40 for the GFEM model in order to suppress the undesirable

oscillations, as shown in Table B.1b.

For the UWFEM model using a $\alpha$ value of 0.2, numerical results at positions after 0.6 start to oscillate although solutions at positions ranging from 0.0 to 0.6 are very close to the corresponding exact solutions. Although these oscillation phenomena can be suppressed by increasing the $\alpha$ value, numerical results might also be over–damped, as illustrated in Table B.1c for the $\alpha$ parameter equal to 0.38 and 1.0. The peclet number is equal to 25.0 in this case.

On the other hand, as shown in Table B.1b, even with the peclet number as high as 50, the CFEM can still provide excellent results with coarse meshes.

Table B.1 Numerical Results of the Conduction–Convection Equation

$$-\frac{d^2T}{dx^2} + (\text{Peclet Number}) \frac{dT}{dx} = 0$$

Using Galerkin FEM, Upwinding FEM, and Canonical FEM Techniques

(a) Peclet Number = 0.25

| x | EXACT | GFEM | UWFEM | CFEM |
|---|---|---|---|---|
| 0.0 | 1.0 | 1.0 | 1.0 | 1.0 |
| 0.1 | 0.91087 | 0.91087 | 0.91086 | 0.91087 |
| 0.2 | 0.81948 | 0.81949 | 0.81946 | 0.81948 |
| 0.3 | 0.72578 | 0.72579 | 0.72575 | 0.72578 |
| 0.4 | 0.62971 | 0.62971 | 0.62968 | 0.62971 |
| 0.5 | 0.53121 | 0.53121 | 0.53117 | 0.53121 |
| 0.6 | 0.43021 | 0.43021 | 0.43018 | 0.43021 |
| 0.7 | 0.32666 | 0.32666 | 0.32663 | 0.32666 |
| 0.8 | 0.22048 | 0.22048 | 0.22046 | 0.22048 |
| 0.9 | 0.11162 | 0.11162 | 0.11160 | 0.11162 |
| 1.0 | 0.0 | 0.0 | 0.0 | 0.0 |

(1). Ten elements were used in all cases.

(2). $\alpha$ is equal to 0.1 for the UWFEM model.

(b) Peclet Number = 50

| x | EXACT | GFEM[1] | GFEM[2] | UWFEM | CFEM |
|---|---|---|---|---|---|
| 0.0 | 1.0 | 1.0 | 1.0 | 1.0 | 1.0 |
| 0.1 | 1.0 | 1.0 | 1.0 | 1.0 | — |
| 0.2 | 1.0 | 0.99907 | 1.0 | 0.99999 | 1.0 |
| 0.3 | 1.0 | 1.0029 | 1.0 | 1.0001 | — |
| 0.4 | 1.0 | 0.99401 | 1.0 | 0.99976 | 1.0 |
| 0.5 | 1.0 | 1.0147 | 1.0 | 1.0010 | — |
| 0.6 | 1.0 | 0.96647 | 1.0 | 0.99609 | 1.0 |
| 0.7 | 1.0 | 1.0789 | 1.0 | 1.0156 | — |
| 0.8 | 0.99995 | 0.8165 | 0.99999 | 0.93750 | 0.9995 |
| 0.9 | 0.99326 | 1.4289 | 0.99716 | 1.2500 | — |
| 1.0 | 0.0 | 0.0 | 0.0 | 0.0 | 0.0 |

(1). Ten elements were used in GFEM[1] and UWFEM models. Forty elements were used in the GFEM[2] model, and five elements were used in the CFEM model.

(2). The value of $\alpha$ is equal to 0.2 for the UWFEM model.

(c) Peclet Number = 25

| x | EXACT | UWFEM[1] | UWFEM[2] |
|---|---|---|---|
| 0.0 | 1.0 | 1.0 | 1.0 |
| 0.1 | 1.0 | 1.0 | 0.99999 |
| 0.2 | 1.0 | 1.0 | 0.99996 |
| 0.3 | 1.0 | 1.0 | 0.99985 |
| 0.4 | 1.0 | 1.0 | 0.99946 |
| 0.5 | 1.0 | 1.0 | 0.99810 |
| 0.6 | 0.99995 | 0.99995 | 0.99334 |
| 0.7 | 0.99944 | 0.99944 | 0.97668 |
| 0.8 | 0.99318 | 0.99318 | 0.91837 |
| 0.9 | 0.91743 | 0.91743 | 0.71429 |
| 1.0 | 0.0 | 0.0 | 0.0 |

(1). Ten elements were used in all cases.

(2). $\alpha$ is equal to 0.38 and 1.0 for the UWFEM[1] and UWFEM[2] cases.

# References

(1). A. G. Evans (Editor), Ceramic Containing Systems — Mechanical Aspects of Interfaces and Surfaces, Noyes Publications, Park Ridge, New Jersey (1986)

(2). K. K. Chawla, Composite Materials — Science and Engineering, Springer–Verlag New York Inc. (1987)

(3). R.W. Rice, "Ceramic Processing:An Overview", AIChE J., 36 [4], 481 (1990)

(4). J.R. Strife, J.J. Brennan, and K.M. Prewo, "Status of Continuous Fiber–Reinforced Ceramic Matrix Composite Processing Technology", Ceram. Eng. Sci. Proc., 11 [7–8], 871 (1990)

(5). D.P. Stinton, T.M. Besmann, and R.A. Lowden, "Advanced Ceramics by Chemical Vapor Deposition Techniques", Ceram. Bull., 67 [2], 350 (1988)

(6). A.J. Caputo, W.J. Lackey, and D.P. Stinton, "Development of a New, Faster Process for the Fabrication of Ceramic Fiber–Reinforced Ceramic Composites by Chemical Vapor Infiltration", Ceram. Eng. Sci. Proc., 6 [7–8], 694 (1985)

(7). Stanley Middleman, "The Interaction of Chemical Kinetics and Diffusion in the Dynamics of Chemical Vapor Infiltration", J. Mater. Res., 4 [6], 1515 (1989)

(8). N.H. Tai and T.W. Chou, "Analytical Modeling of Chemical Vapor Infiltration in Fabrication of Ceramic Composites", J. Am. Ceram. Soc., 72 [3], 414 (1989)

(9). S.M. Gupte and J.A. Tsamopoulos, "Densification of Porous Materials by Chemical Vapor Infiltration", J. Electrochem. Soc., 136 [2], 555 (1989)

(10). Ching Yi Tsai and Seshu B. Desu, "Contribution of Gas–Phase Reactions to the Deposition of SiC by a Forced–Flow Chemical Vapor Infiltration Process", Mater. Res. Soc. Symp., Vol. 250, 227 (1992)

(11). R.P. Currier, "Overlap Model for Chemical Vapor Infiltration of Fibrous Yarns", J. Am. Ceram. Soc., 73 [8], 2274 (1990)

(12). G.Y. Chung, B.J. McCoy and J.M. Smith, "Chemical Vapor Infiltration: Modelling Solid Matrix Deposition in Ceramic–Ceramic Composites", Chem. Eng. Sci., 46 [3], 723 (1991)

(13). T.L. Starr, "Model for CVI of Short Fiber Preforms", Ceram. Eng. Sci. Proc., 8 [7–8], 951 (1987)

(14). N.H. Tai and T.W Chou, "Modeling of an Improved Chemical Vapor Infiltration Process for Ceramic Composites Fabrication", J. Am. Ceram. Soc., 73 [6], 1489 (1990)

(15). S.M. Gupte and J.A. Tsamopoulos, "An Effective Medium Approach for Modeling Chemical Vapor Infiltration of Porous Ceramic materials", J. Electrochem. Soc., 137 [5], 1626 (1990)

(16). S.M. Gupte and J.A. Tsamopoulos, "Forced–Flow Chemical Vapor Infiltration of Porous Ceramic Materials", J. Electrochem. Soc., 137 [11], 3675 (1990)

(17). Stratis V. Sotirchos, "Dynamic Modeling of Chemical Vapor Infiltration", AIChE J., 37 [9], 1365 (1991)

(18). R.R. Melkote and K.F. Jensen, "Gas Diffusion in Random–Fiber Substrates", AIChE J., 35 [12], 1942 (1989)

(19). S. Reyes and K.F. Jensen, "Estimation of Effective Transport Coefficients in Porous Solids Based on Percolation Concepts", Chem. Eng. Sci., 40 [9], 1723 (1985)

(20). Manolis M. Tomadakis and Stratis V. Sotirchos, "Effective Knudsen Diffusivities in Structures of Randomly Overlapping Fibers", AIChE J., 37 [1], 74 (1991)

(21). Manolis M. Tomadakis and Stratis V. Sotirchos, "Knudsen Diffusivities and Properties of Structures of Unidirectional Fibers", AIChE J., 37 [8], 1175 (1991)

(22). Manolis M. Tomadakis and Stratis V. Sotirchos, "Effects of fiber Orientation and Overlapping on Knudsen, Transition, and Ordinary Regime Diffusion in Fibrous Substrates", Mater. Res. Soc. Symp., Vol. 250, 221 (1992)

(23). Brian W. Sheldon, "The Control of Gas Phase Kinetics to Maximize Densification during Chemical Vapor Infiltration", J. Mater. Res., 5 [11], 2729 (1990)

(24). Seshu B. Desu and Surya R. Kalidindi, "Determination of Rate Controlling Step in CVD Processes with Gas Phase and Surface Reactions", Jap. J. of App. Phy., 29 [7], 1310 (1990)

(25). R. Jackson, Transport in Porous Catalysts, Elsevier North–Holland, New York (1977)

(26). R.B. Bird, W.E. steward, and E.N. Lightfoot, Transport Phenomena, John Wiley & Sons, New York (1960)

(27). E.L. Cussler, Diffusion: Mass Transfer in Fluid Systems, Cambridge University Press, New York (1984)

(28). Thomas L. Starr and Arlynn W. Smith "3–D Modeling of Forced–Flow Thermal–Gradient CVI for Ceramic Composite Fabrication", Mater. Res. Soc. Symp., Vol. 168, 55 (1990)

(29). A. Yuuki, Y. Matsui, and K. Tachibana, "A Study on Radical Fluxes in Silane Plasma CVD from Trench Coverage Analysis", Jpn. J. Appl. Phys., 28 [2], 212 (1989)

(30). M.J. Cooke and G. Harris, "Monte Carlo Simulation of Thin–Film Deposition in a Rectangular Groove", J. Vac. Sci. Technol. A7 [6], 3217 (1989)

(31). Zhi J. Chen and Seshu B. Desu, "Monte Carlo Simulation of Chemical Vapor Deposition", J. Chemical Vapor Deposition, 1 [2], 191 (1992)

(32). Masato Ikegawa and Junichi Kobayashi, "Deposition Profile Simulation Using the Direct Simulation Monte Carlo Method", J. Electrochem. Soc., 136 [10], 2982 (1989)

(33). Kazunori Watanabe and Hiroshi Komiyama, "Micro/Macrocavity Method Applied to the Study of the Step Coverage Formulation Mechanism of $SiO_2$ Films by LPCVD", J. Electrochem. Soc., 137 [4], 1222 (1990)

(34). M. Ikegawa and K. Kobayashi, "Deposition Profile Simulation using the Direct Simulation Monte Carlo Method", The Electrochem. Soc. Softbound Proceedings Series (PV 88–22), Plasma Processing, G. S. Mathad, G. C. Schwartz and D.W. Hess, Editors, p. 378 (1988)

(35). Sulagna Chatterjee and Carol M. McConica, "Prediction of Step Coverage during Blanket CVD Tungsten Deposition in Cylindrical Pores", J. Electrochem. Soc., 137 [1], 328 (1990)

(36). A. Hasper, J. Holleman, J. Middlehoek, C. R. Kleijn, and C. J. Hoogendoorn, "Modeling and Optimization of the Step Coverage of Tungsten LPCVD in Trenches and Contact Holes", J. Electrochem. Soc., 138 [6], 1728 (1991)

(37). T. S. Cale, M. K. Jain, and G. B. Raupp, "Programmed Rate Processing to Increase Throughput in LPCVD", J. Electrochem. Soc., 137 [5], 1526 (1990)

(38). T. S. Cale, and G. B. Raupp, "Free Molecular Transport and Deposition in Cylindrical Features", J. Vac. Sci. Technol. B8 [4], 649 (1990)

(39). Manoj K. Jain, Timothy S. Cale, and Todd H. Gandy, "Comparison of LPCVD Film Conformalities Predicted by Ballistic Transport–Reaction and Continuum Diffusion–Reaction Models", J. Electrochem. Soc., 140 [1], 242 (1993)

(40). Eugene E. Petersen, Chemical Reaction Analysis, Englewood Cliffs, New Jersey (1965)

(41). Takaaki Kawahara, Akimasa Yuuki, and Yasuji Matsui, "A Study on the Behavior of $SiO_2$ Film Precursors with Trench Deposition Method for $SiH_4/O_2$ Low Pressure Chemical Vapor Deposition", Japanese J. of Appl. Phys., 30 [3], 431 (1991)

(42). Ching Yi Tsai and Seshu B. Desu, "Step Coverage Modeling of Thin Films Deposited by CVD Using Finite Element Method", Mater. Res. Soc. Symp., Vol. 250, 65 (1992)

(43). J.N. Reddy, An Introduction to the Finite Element Method, McGraw–Hill Book Company, New York (1984)

(44). James A. Liggett and Philip L.F. Liu, The Boundary Integral Equation Method for Porous Media Flow, Allen & Unwin, Boston (1983)

(45). C.A. Brebbia, The Boundary Element Method for Engineers, Pentech Press, London (1980)

(46). Andrew R. Neureuther, C.H. Ting and C.Y. Liu, "Application of Line–Edge Profile Simulation to Thin–Film Deposition Processes", IEEE Trans. on Electron Devices, ED–27 [8], 1449 (1980)

(47). S. Dushmann, Scientific Foundations of Vacuum Technique, John Wiley and Sons, New York (1949)

(48). Surya R. Kalidindi and Seshu B. Desu, "Analytical Model for the Low Pressure Chemical Vapor Deposition of $SiO_2$ from Tetraethoxysilane", J. Electrochem. Soc., 137 [2], 624 (1990)

(49). Francis S. Galasso, Chemical Vapor Deposited Materials, Chapter 2 "CVD SiC", CRC Press, Boca Raton (1991)

(50). M. I. Chaudhry, R. J. McCluskey and R. L. Wright, "The Role of Carrier Gases in the Epitaxial Growth of $\beta$–SiC on Si by CVD", J. of Crystal Growth, 113, 120 (1991)

(51). Koji Takahashi, Shigehiro Nishino and Junji Saraie, "Effect of Acceptor Impurity Addition in Low Temperature Growth of 3C–SiC", J. of Crystal Growth, 115, 617 (1991)

(52). L. Aggor and W. Fritz, Chem. Ing. Technik, "Kinetik der pyrolytischen Abscheidung von Siliciumcarbid auf kugelförmigen Teilchen in einem Fließbettreaktor", 43, 472 (1971)

(53). A. W. C. Van Kemenade and C. F. Stemfoort, "On the Formation of $\beta$–SiC from Pyrolysis of $CH_3SiCl_3$ in Hydrogen", J. of Crystal Growth, 12, 13 (1972)

(54). J. Chin, P.K. Gantzel and G. Hudson, "The Structure of Chemical Vapor Deposited Silicon Carbide", Thin Solid Films, 40, 57 (1977)

(55). K. Brennfleck, E. Fitzer, G. Schoch, and M. Dietrich, "CVD of SiC Interlayers and Their Interaction with carbon Fibers and with Multi–Layered NbN–Coatings", Proc. 9th Int. CVD Conf., The Electrochem. Soc., 649 (1984)

(56). T.M. Besmann and M.L. Johnson, "Kinetics of the Low–Pressure Chemical Vapor Deposition of Silicon Carbide", Proc. Third Int. Conf. on Ceramic Materials and Components for Engines, Las Vegas, Nevada, 443, Nov. 27–30 (1988)

(57). Myoung Gi So and John S. Chun, "Growth and Structure of Chemical Vapor Deposited Silicon Carbide from Methyltrichlorosilane and Hydrogen in the Temperature Range of 1100 to 1400°C", J. Vac. Sci. Technol., A6 [1], 5 (1988)

(58). A. Figueras, S. Garelik, R. Rodriguez–Clemente, B. Armas, C. Combescure and C. Dupuy, "A Morphological and Structural Study of SiC Layers Obtained by LPCVD using Tetramethylsilane", J. of Crystal Growth, 110, 528 (1991)

(59). Dieter Neuschutz and Farzin Salehomoum, "Kinetics of Chemical Vapor Deposition of SiC between 750 and 850°C at 1 bar Total Pressure", Mater. Res. Soc. Symp., Vol. 250, 41 (1992)

(60). Byung Jin Choi, Sun Ho Jeun and Dai Ryong Kim, "The Effects of $C_3H_8$ on the Chemical Vapor Deposition of Silicon Carbide in the $CH_3SiCl_3$ System", J. of the Euro. Cera. Soc., 9, 357 (1992)

(61). P. Rai–Choudhury and N. P. Formigoni, "$\beta$–Silicon Carbide Films", J. Electrochem. Soc., 116 [10], 1440 (1969)

(62). J. E. Doherty, "Chemical Vapor Deposition of Structural Ceramic Materials", J. Metals, 28, 6 (1976)

(63). T. Kaneko, T. Okuno and H. Yumoto, "Growth Kinetics of Silicon Carbide CVD", J. of Crystal Growth, 91, 599 (1988)

(64). Y. Furumura, M. Doki, F. Mieno, T. Eshita, T. Suzuki and M. Maeda, "Heteroepitaxial $\beta$–SiC on Si", J. Electrochem. Soc., 135 [5], 1255 (1988)

(65). J. Schlichting, "Chemical Vapor Deposition of Silicon Carbide", Powder Metall. Int., 12 [3], 141 and 12 [4], 196 (1980)

(66). Ching Yi Tsai, Seshu B. Desu, Chien C. Chiu, and J.N. Reddy, "The Role of Gas Phase Reactions in Modeling of the Forced–Flow Chemical Vapor Infiltration Process", J. Electrochem. Soc., 140 [7], 2121 (1993)

(67). Gary S. Fischman and William T. Petuskey, "Thermodynamic analysis and Kinetic Implications of Chemical vapor Deposition of SiC from Si–C–Cl–H System", J. Am. Ceram. Soc., 68 [4], 185 (1985)

(68). Chien C. Chiu and Seshu B. Desu, "Conversion of Single Crystal Si (100) to SiC Film by $C_2H_2$", Journal of Mater. Res., 8 [3], 535 (1993)

(69). Jean N. Burgess and Thomas Lewis, "Kinetics of the Reduction of Methyltrichlorosilane by Hydrogen", Chemistry and Industry, 19, 76 (1974)

(70). Seshu B. Desu, J. Am. Ceram. Soc., "Decomposition Chemistry of Tetraethoxysilane", 72 [9], 1615 (1989)

(71). E.D. Evans, and B. Subramaniam, "Extension of One–Dimensional Film Model for Chemical Vapor Deposition to Predict Selective Epitaxial Growth Rates", J. Electrochem. Soc., 138 [2], 589 (1991)

(72). Richard H.F. Pao, Fluid Dynamics, Charles E. Merrill Books., Columbus, OH (1967)

(73). O.C. Zienkiewicz and R.L. Taylor, The Finite Element Method: Basic Formulation and Linear Problems (Vol. 1), Chap. 9, McGraw–Hill, New York (1989)

(74). Richard L. Burden and J. Douglas Faires, Numerical Analysis (3rd), Prindle, Weber & Schmidt, Boston, MA (1985)

(75). F. Langlais, C. Prebende, B. Tarride and R. Naslain, "On the Kinetics of the CVD of Si from $SiH_2Cl_2/H_2$ and SiC from $CH_3SiCl_3/H_2$ in a Vertical Tubular Hot–Wall Reactor", J. de Phys., Colloq. C5, 50, 93 (1989)

(76). Ching Yi Tsai, Seshu B. Desu and Chien C. Chiu, "Kinetic Study of Silicon Carbide Deposited from Methyltrichlorosilane Precursor", Submitted to Journal of Mater. Res.

(77). B. Rikard Gebart, "Permeability of Unidirectional Reinforcements for RTM", SICOMP Technical Report 90–006

(78). C. Y. Chen, Chem. Rev., "Filtration of Aerosols by Fibrous Media", 55, 595 (1955)

(79). H. Schlichting, Boundary Layer Theory, 7th Edition, McGraw–Hill, New York (1979)

(80). R. C. Progelhof, J. L. Throne and R. R. Ruetsch, "Methods for Predicting the Thermal Conductivity of Composite Systems: A Review", Polymer Eng. and Sci., 16 [9], 615 (1976)

(81). Frank Kreith, Principles of Heat Transfer, 3rd Edition, Intext Press Inc., New York (1973)

(82). In–Hwan Oh, Christos G. Takoudis and Gerold W. Neudeck, "Mathematical Modeling of Epitaxial Silicon Growth in Pancake Chemical Vapor Deposition Reactors", J. Electrochem. Soc., 138 [2], 554 (1991)

(83). G. L. Guymon, V.H. Scott and L.R. Herrmann, "A General Numerical Solution of the Two–Dimensional Diffusion–Convection Equation by the Finite Element Method", Water Resour. Res., 6 [6], 204 (1970)

(84). J. C. Heinrich and O. C. Zienkiewicz, "The Finite Element Method and Upwinding Techniques in the Numerical Solution of Convection Dominated Flow Problems", AMD 34, 105 (1979)

(85). T. J. R. Hughes, Editor, Finite Element Methods for Convection Dominated Flows, ASME Winter Annual Meeting, ASME, New York (1979)

(86). P. Gresho and R.L. Lee, "Don't Suppress the Wiggles — They're Telling You Something", AMD 34, 37 (1979)

# Vita

Ching Yi Tsai was born on December 20, 1958 in Tainan, Taiwan. He grew up in Taichung, Taiwan where he graduated from the First Provincial Taichung High School in 1977. Ching Yi attended National Cheng Kung University from 1977–1981, and graduated in June 1981 with a Bachelor of Science degree in Naval Architecture and Marine Engineering. From Fall 1986 to Winter 1987, he pursued his Master of Science degree in the Department of Aerospace and Mechanical Engineering of Arizona State University, and graduated in December 1987. He enrolled in the Department of Engineering Science and Mechanics at Virginia Polytechnic Institute and State University to pursue his Ph.D. in Fall 1989.

Ching Yi Tsai